STABILIZATION OF LIQUID INTERFACES

By

ABDULLAH KEREM UĞUZ

A DISSERTATION PRESENTED TO THE GRADUATE SCHOOL
OF THE UNIVERSITY OF FLORIDA IN PARTIAL FULFILLMENT
OF THE REQUIREMENTS FOR THE DEGREE OF
DOCTOR OF PHILOSOPHY

UNIVERSITY OF FLORIDA

2006

To my Mom and my Dad

ACKNOWLEDGMENTS

First of all, I would like to thank Professor Ranga Narayanan for his support and advice. He has been both a mentor and a friend. He always emphasizes the importance of enjoying your work. Dr. Narayanan is enthusiastic about his work and this is the best motivation for a student. His dedication to teaching and his philosophy has inspired me to be in academia. I would like to thank Nick Alvarez. He started as an undergraduate student helping me with my experiments. Then, he became co-author of my papers. The members of my PhD committee, Prof. Oscar D. Crisalle, Prof. Loc Vu-Quoc, and Prof. Dmitry Kopelevich also deserve my gratitude. Also, I would like to thank Prof. Alex Oron for accepting to be in my defense. I have really enjoyed taking classes from Prof. Vu-Quoc, Prof. Crisalle and Prof. Narang. Their teaching philosophies of seeing the big picture have deeply influenced me. Many thanks go to my friends Özgur Özen and Berk Usta for their friendship. I am lucky to be their colleague.

Many thanks go to Sinem Özyurt for her constant support throughout my graduate education. I thank her for always being there when I need her. She is very special for me.

I would like to thank my brother, Erdem Uğuz, who has always been with me, and has motivated me for my work. I would like to express my highest appreciation for my parents and my brother for their love and support throughout my educational career. It has been difficult for them and for me because of the large distance. Thank you for your patience, encouragement and your moral support.

I would like to thank the University of Florida for an Alumni Fellowship.

TABLE OF CONTENTS

LIST OF TABLES

LIST OF FIGURES

Abstract of Dissertation Presented to the Graduate School
of the University of Florida in Partial Fulfillment of the
Requirements for the Degree of Doctor of Philosophy

STABILIZATION OF LIQUID INTERFACES

By

Abdullah Kerem Uğuz

August 2006

Chair: Ranganatha Narayanan
Major Department: Chemical Engineering

This dissertation advances the understanding of the instability of interfaces that occur in Rayleigh-Taylor (RT) and liquid bridge problems and investigates two methods for delaying the onset of instability, namely, changing the geometry and judiciously introducing fluid flow. In the RT instability, it is shown theoretically that an elliptical shaped interface is more stable than a circular one of the same area given that only axiymmetric disturbances are inflicted on the latter. In a companion study on bridges, it is experimentally shown that a liquid bridge with elliptical end plates is more stable than a companion circular bridge whose end plates are of the same area as the ellipses. Using two different sizes of ellipses whose semi-major axes were deviated from the radii of the companion circles by 20%, it was found that the elliptical bridge's breakup height was nearly 3% longer than that of the corresponding circular bridge.

Another way to stabilize interfaces is to judiciously use fluid flow. A comprehensive theoretical study on the RT problem involving both linear and weakly nonlinear methods shows that mode interactions can delay the instability of an erstwhile flat interface between two viscous fluids driven by moving walls. It is

shown that when the flow is driven under Couette conditions the breakup point remains unchanged compared to the classical RT instability. However, in a closed two-dimensional container, shearing the fluids enhances the stability provided a flat interface is an allowable base solution. In addition, for a selected choice of parameters, three different critical points can be obtained. Therefore, there is a second window of stability for the shear-induced RT problem. A weakly nonlinear analysis using a dominant balance method showed the problem has either a backward or forward pitchfork bifurcation depending on the critical point around which the analysis is performed. In an experimental study investigating the effect of shear-driven flow in a liquid bridge, it was shown that a returning flow in both the encapsulating liquid and the bridge would increase the stability of a non-vertical bridge depending on the direction of shear by as much as 12%.

CHAPTER 1
INTRODUCTION

This dissertation involves the study of two interfacial instability problems with the objectives of understanding the underlying physics behind the instabilities and finding ways to delay them. The two problems are the liquid bridge and the Rayleigh-Taylor instabilities. A liquid bridge is a volume of liquid suspended between two solid supports. It can be held together without breaking owing to surface tension forces. However, at some critical height the surface tension effects are not strong enough to maintain the integrity of the bridge between the supporting disks and the bridge becomes unstable and collapses. A depiction of a stable and an undulating bridge is given in Figure 1-1.

The instability occurs because there is a playoff between pressure gradients that are generated due to transverse curvature and those caused by longitudinal curvature. As the spacing between the end plates increases, the latter becomes weak, an imbalance occurs and the necking becomes more pronounced leading to ultimate breakup. The Rayleigh-Taylor instability, on the other hand, is observed when a light fluid underlies a heavy one, and the common interface becomes unstable at some width. For large enough widths, the stabilizing surface potential energy is insufficient to withstand the destabilizing gravitational energy. Such an instability is depicted in Figure 1-2. A basic understanding of the instability is needed if there is any hope of altering the stability limit by, say, changing the geometry or by applying an outside force to get more stability. A fair question to ask is to why these two instability problems are chosen is addressed next.

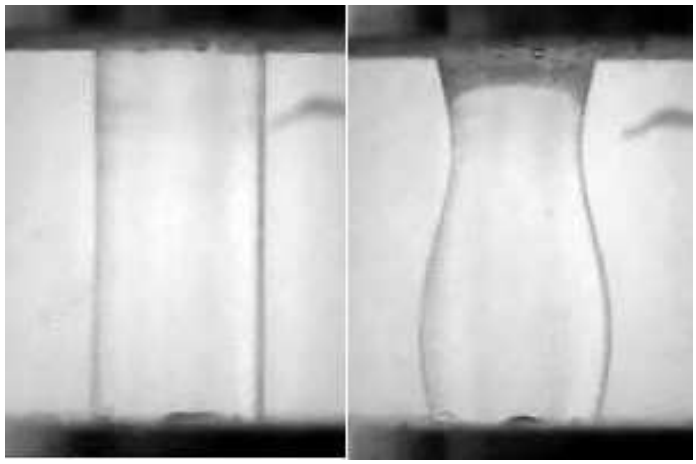

Figure 1-1. Liquid bridge photo a) Stable liquid bridge b) Unstable liquid bridge at higher height.

1.1 Why Were the Rayleigh-Taylor Instability and Liquid Bridges Studied?

These two problems are similar in many ways. They exhibit instability when a control parameter, which can be the height for a liquid bridge, or the width of the container for the Rayleigh-Taylor instability, is exceeded beyond a critical value. At the critical point, the interface deflects and proceeds to complete breakup. In both problems the instability can be understood without taking viscosity into account. We will also see that the physics of both problems can be explained by the Rayleigh work principle. Also, in both problems shear can be induced in the base state causing flow, which in turn may alter the stability limit. In addition, understanding the Rayleigh-Taylor instability from a theoretical standpoint in the much simpler Cartesian coordinates is instructive for studying liquid bridges whose models are complicated because of the cylindrical coordinates.

Both liquid bridge and Rayleigh-Taylor problems have numerous technological applications. Liquid bridges occur, for example, in the production of single crystals by the floating zone method [1, 2]. They occur in the form of flowing jets in the encapsulated oil flow in pipelines [3]. In the melt spinning of fibers, liquid jets emitting from nozzles accelerate and thin until they reach a steady state and

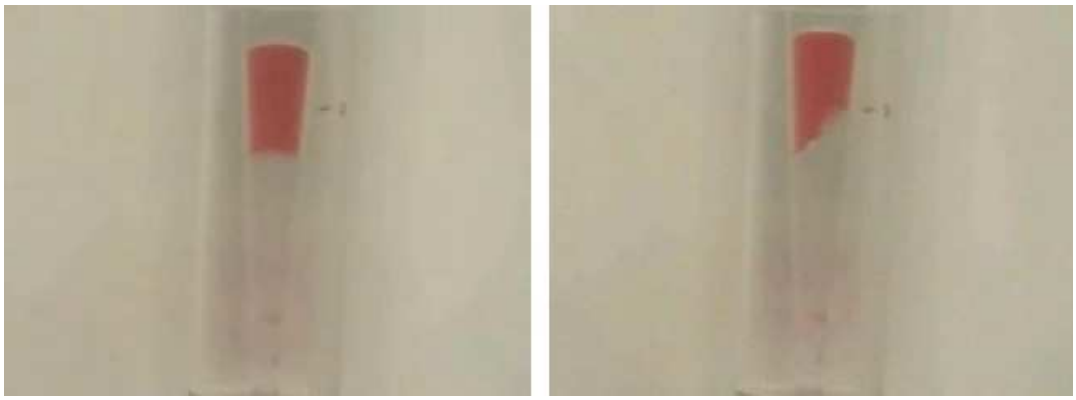

Figure 1-2. Interface between heavier colored water on top of lighter transparent decane in a conical tube a) Stable interface b) Unstable interface at higher diameter.

then they break on account of instability. Besides such technological applications in materials science, liquid bridges have importance in biomedical science. For example, Grotberg [4] shows the vast scope of biofluid mechanics ranging from the importance of the cell topology in the reopening of the pulmonary airways [5] to the occluding of oxygen resulting from the capillary instabilities [6]. In all these studies, the mucus that closes the airways is represented by a liquid bridge configuration.

The Rayleigh-Taylor instability also plays a role in a number of situations, some natural, others technological. For example, the inability to obtain any capillary rise in large diameter tubes is a result of the Rayleigh-Taylor instability. When a fluid bilayer is heated from below, it becomes top heavy and the interface can become unstable even before convection sets in due to buoyancy. In astrophysics, the adverse stratification of densities in the star's gravitational field is responsible for the overturn of the heavy elements in collapsing stars [7]. Rayleigh-Taylor instability is also observed in inertial confinement fusion (ICF), where it is necessary to compress the fuel to a density much higher than that of a solid. Rayleigh-Taylor instability occurs in two different occasions during this process [8].

It is the central objective of this study to see how to stabilize liquid interfaces by applying an outside force or by changing the geometry of the system. For that purpose, understanding the physics of the system, including the dissipation of disturbances and the nature of the breakup of the interface as a function of geometry is very important.

In applications of liquid bridges such as the floating zone technique, the molten crystal is surrounded by another liquid to encapsulate the volatile components and the presence of temperature gradients causes flow. Whether such flow can cause stability or not is of interest, so in this study we shall consider the role of shear in a liquid bridge problem. Another effect that is studied is the shape of the supporting solid disks on the stability of liquid bridges. Most of the studies on liquid bridges pertain to bridges of circular end plates. Physical arguments suggest that noncircular bridges ought to be more stable so this research also deals with the stability of noncircular liquid bridges.

The current research is both experimental and theoretical in character. The theoretical methods include linear stability analysis via perturbation calculations and weakly nonlinear analysis via a dominant balance method. The experimental methods involve photography of the interface shapes. The work on liquid bridges will be experimental in nature on account of the difficulty in analyzing the problem without resort to computations. The work on the Rayleigh-Taylor problem, on the other hand, will be theoretical in nature on account of difficulty in obtaining clear experiments.

All instability problems are characterized by models that contain nonlinear equations. This must be true because instability by the very nature of its definition means that a base state changes character and evolves into another state. The fact that we have at least two states is indicative that we have nonlinearity in the model. If the complete nonlinear problem could be solved, then all of the physics

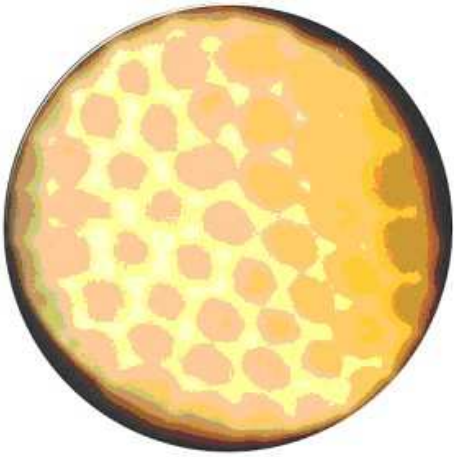

Figure 1-3: Shadowgraph image showing convection.

would become evident. However, solving nonlinear problems is by no means an easy task and one endeavors to find the behavior by linearization of the model about a known base state whose stability is in question. This local linearization is sufficient to determine the necessary conditions for instability and in the absence of a complete solution to the modeling equations it would seem beneficial to obtain the conditions for the onset of the instability. To determine what happens beyond the critical point requires the use of weakly nonlinear analysis. Once the instability sets in, the interface created in the ordinary liquid bridge problem and Rayleigh-Taylor configuration evolves to complete breakup. However, under some conditions even this may not be true and we will see later in this dissertation that a secondary state may be obtained if shear is applied. There are interfacial instability problems that have been studied where patterns may be observed once the instability sets in. An example of this is the Rayleigh-Bénard problem problem, which is a problem of convective onset in a fluid that is heated from below. When the temperature gradient across the layer reaches a critical value, patterns are predicted and in fact are also observed. Figure 1-3 is a photograph of such patterns seen in an experiment. The fact that steady patterns are predicted and observed implies a sort of "saturation" of solutions that might be expected in a weakly

nonlinear analysis, weak in the sense that the analysis is confined to regions close to the onset of the instability. Contrast this behavior with that expected of the common Rayleigh-Taylor problem discussed earlier. In this problem the onset of the instability leads to breakup and no saturation of solutions may be expected. All this will become important in our discussion of this problem later on.

1.2 Organization of the Thesis

The rest of this thesis pertains to both experimental and theoretical aspects of problems in Rayleigh-Taylor instability and liquid bridges. As stated, our goal is to understand the reasons underlying these instabilities, to predict them and finally to try to delay them.

Chapter 2 outlines the physics of the instability for both problems, namely Rayleigh-Taylor and liquid bridges. This chapter includes a short discussion of liquid jets because a preliminary study of liquid jets forms the basis for the study of liquid bridges. In other words most of the physics pertaining to liquid bridges can be understood more easily by studying liquid jets. A general literature review and applications are also given in this chapter.

Chapter 3 discusses the governing equations along with boundary and interface equations in their general forms. The theoretical methods required to solve these equations is also presented in this chapter.

Chapter 4 focuses on the Rayleigh-Taylor instability. In the first section, the critical point is found using Rayleigh's work principle. Then, the same result is obtained by a perturbation calculation. This is followed by a calculation that shows the effect of changing the geometry on the stability by considering instability in an elliptical interface via a perturbation calculation. The last section presents the shear-introduced stabilization of the Rayleigh-Taylor problem where a theory is advanced. The dispersion curves are plotted by using linear stability analysis while the types of bifurcations are determined via a weakly nonlinear analysis.

Chapter 5, which deals with bridges, is organized in a manner similar to the previous chapter. First, the critical point is determined using Rayleigh's work principle. Then, a perturbation calculation is presented that obtains the same result. This is followed by a calculation where the effect of off-centering a liquid bridge with respect to its surrounding liquid on the stability of the liquid bridge is studied. While the idea of off-centering seems peripheral to our objectives it does introduce an imperfection and is important because we must make sure in bridge experiments that this imperfection has little if any consequence. In addition this configuration is an idealization of the fluid configuration that appears in the floating zone crystal growth technique. The theoretical method to investigate the off-centering problem involves the use of an energy method. The details of the derivation, and the physical explanation of the results are emphasized in this chapter. Thereafter this chapter contains the details and results of two series of experiments. In the first series, we investigate the effect of the geometry via the stability of elliptical liquid bridges. A physical explanation of the effect of changing the end plates of a liquid bridge from circles to ellipses on the stability of liquid bridges is given through the dissipation of disturbances. The breakup point of elliptical liquid bridges is then determined by means of experiments. The second series deals with the effect of shear on the stability of liquid bridges. The experiments show the stabilizing effect of returning flow in a liquid bridge on its stability and are assisted by rough scoping calculations on the base state.

Chapter 6 is a general conclusion and presents a scope for a future study.

CHAPTER 2
THE PHYSICS OF THE PROBLEMS AND THE LITERATURE REVIEW

The purpose of this chapter is to familiarize the reader with the basic physics and to provide a brief overview of the literature. We know from the previous chapter that both liquid bridge and Rayleigh-Taylor problems may become unstable. Here, we will give the details of the instability mechanisms. We start with a discussion of liquid jets because it serves as a precursor to the study of liquid bridges.

A liquid jet forms when it ejects from a nozzle as in ink-jet printing and agricultural sprays. Such jets to some approximation are cylindrical in shape. However, a cylindrical body of liquid in uniform motion or at rest does not remain cylindrical for long and left to itself, spontaneously undulates and breaks up. A picture of such a body of liquid is depicted in Figure 2-1. Given the fact that a spherical body of liquid upon perturbation returns to its spherical shape and a body of liquid in a rectangular trough also returns to its original planar configuration we might wonder why a cylindrical volume of liquid behaves as depicted in the picture leading to necking and breakup.

The physics of the instability can be explained by introducing Figure 2-2, which depicts a volume of liquid with a perturbation imposed upon it. If viewed from the ends as in Figure 2-2(a), the pressure in the neck exceeds the pressure in the bulge and the thread gets thinner at the neck. This is the transverse curvature effect. It reminds us of the fact that the pressure in small diameter bubbles is greater than the pressure in large diameter bubbles. On the other hand if viewed from the perspective of a front elevation as in Figure 2-2(b), the pressure under a crest is larger than the pressure under the trough or neck and consequently,

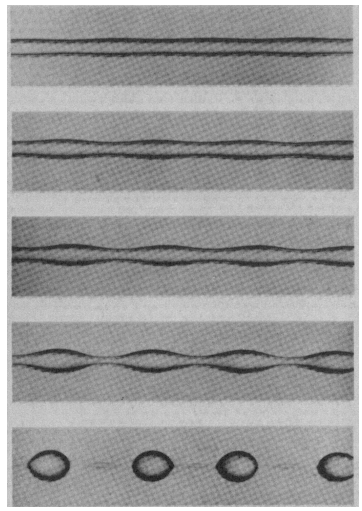

Figure 2-1. Photograph illustrating the jet instability. Reprinted from Journal of Colloid Science, vol. 17, F. D. Rumscheidt and S. G. Mason, "Break-up of stationary liquid threads," pp. 260-269, 1962, with permission from Elsevier.

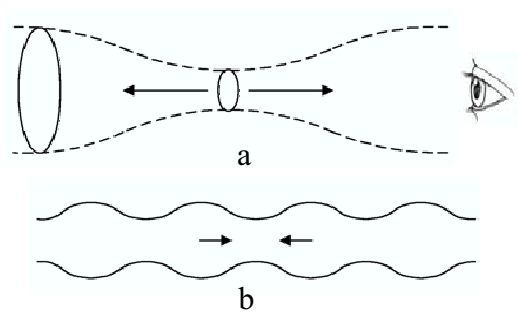

Figure 2-2. Liquid jet with a given perturbation a) Transverse curvature b) Longitudinal curvature (Adapted from [10]).

the liquid moves towards the neck restoring the stability. This is the longitudinal curvature effect. The longer the wavelength the weaker is this stabilizing effect. The critical point is attained when there is a balance between these offsetting curvatures.

The breakup of liquid jets has been extensively studied, both experimentally and theoretically. Such studies can be tracked back to Savart's [11] experiments and Plateau's observations [12], which led Plateau to study capillary instability. Theoretical analysis had started with Rayleigh [13, 14] for an inviscid jet injected

into air. Neglecting the effects of the ambient air, Rayleigh showed through a linear stability analysis that all wavelengths of disturbances exceeding the circumference of the jet at rest would be unstable. He was also able to determine that one of the modes had to grow faster. Rayleigh [15] conducted some experiments on the breakup of jets and observed that the drops, which form after the breakup, were not uniform. He attributed this nonuniformity to the presence of harmonics in the tuning forks he used to sound the jet and create the disturbances. The effect of viscosity was also considered by Rayleigh [16] for the viscosity dominant case. The general case and the theory on liquid jets is summarized and extended in several directions by Chandrasekhar [17]. The experimental work by Donnelly and Glaberson [18] was in good agreement with Chandrasekhar's theory as seen in Figure 2-3. Here, a dimensionless growth constant is plotted against a dimensionless wave number, x. The critical point is reached when the dimensionless wave number is equal to unity. In their experiments, Donnelly and Glaberson [18] also saw the sort of nonuniformity of the drops that Rayleigh observed. Lafrance [19] attributed this phenomenon to the nonlinearity. Through his calculation, he was able to match the experimental data for early times. Mansour and Lundgren [20] extended the calculation for large times.

In some applications, the jet is surrounded by another liquid as in the oil flow in pipelines where an internal oil core is surrounded by an annular region of water. In this regard, Tomotika [21] extended the Rayleigh stability to a viscous cylindrical jet surrounded by another viscous liquid. A more general problem was solved later using numerical methods by Meister and Scheele [22] and the reader is referred to the recent book by Lin [23] for an overview of the phenomena of jet breakup. Although the study of liquid jets started more than a century ago, this topic is still relevant due to applications in modern technology such as nanotechnology [24].

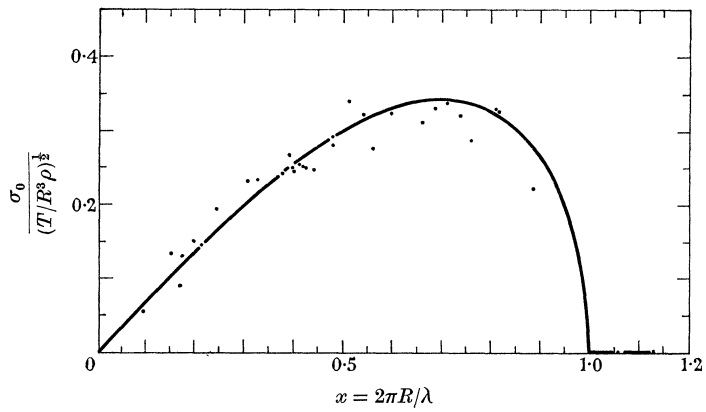

Figure 2-3. Dispersion curve for the jet. The solid line represents Chandrasekhar's theory [17]. Reprinted from Proceedings of the Royal Society of London Series A - Mathematical and Physical Sciences, vol. 290, R. J. Donnelly and W. Glaberson, "Experiments on capillary instability of a liquid jet," pp. 547-556, 1966, with permission from the Royal Society.

When a liquid jet is confined between two solid supports a liquid bridge is obtained as in Figure 2-4. This liquid bridge can attain a cylindrical configuration if it is surrounded by another fluid of the same density.

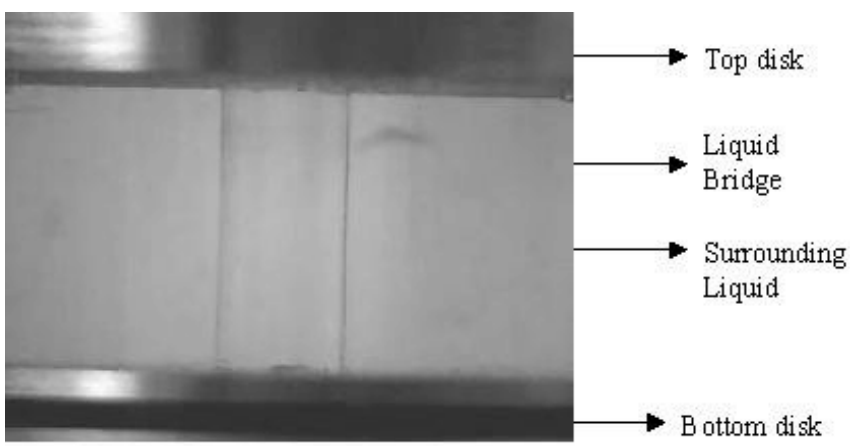

Figure 2-4: Liquid bridge photograph from one of our experiments.

Liquid bridges have been studied as far back as Plateau [12] who showed theoretically that in a gravity-free environment, the length to radius ratio of a cylindrical liquid bridge at breakup is 2π. This instability takes place because of a competition between the stabilizing effect of longitudinal curvature and

destabilizing effect of transverse curvature as in the liquid jets. However, while the physics of the instability of cylindrical jets and bridges are similar there are subtle differences between these two configurations. First, there is no natural control parameter when studying the instability of jets while the bridge does come equipped with one; it is the length to radius ratio. Second, there is no mode with a maximum growth rate in the liquid bridge problem.

To obtain a cylindrical configuration of a liquid bridge requires a gravity-free environment. There are various ways to decrease the effect of the gravity during an experiment. These include going to outer space, using density-matched liquids, or using small liquid bridge radii. The effect of gravity is represented by the Bond number, Bo, which is the ratio of gravitational effects to the effect of surface tension and is given by $Bo = \frac{g\Delta\rho R^2}{\gamma}$; where g is the constant of gravitational acceleration, $\Delta\rho$ is the absolute density difference between the inner and the outer liquid, R is the radius and γ the interfacial tension. Small radii can therefore cause a decrease in the effect of gravity or the density mismatch. It might be noted that while the Plateau limit was obtained for a gravity free case, instability limits for non zero Bond numbers and for a variety of input liquid volumes have also been calculated [25].

Liquid bridges have often been investigated for their importance in technological applications, such as in the floating zone method for crystal growth of semi-conductors [1, 2], for their natural occurrence such as in lung airways [4] and for scientific curiosity [25, 26]. Liquid bridges, as they appear in crystal growth applications, are usually encapsulated by another liquid to control the escape of volatile constituents. The floating zone method is used to produce high-resistivity single-crystal silicon and provides a crucible-free crystallization [27]. In this technique, a molten zone, which is depicted in Figure 2-5, is created between a polycrystalline feed rod and a monocrystalline seed rod. The heaters are translated

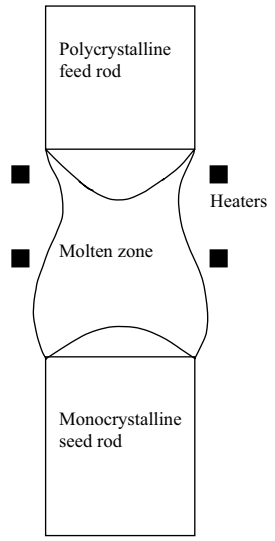

Figure 2-5: Cartoon illustrating floating zone method.

uniformly thereby melting and recrystallizing a substance into a more desirable state. The crystal grows as the melt solidifies on the seed. The aim is to obtain stable molten zones or liquid bridges. Gravity is the major problem in the stability of the melt. On earth, because of the hydrostatic pressure, the melt zone has to be small, causing small crystals. In the case of GaSb for example, a material that is used in electronic devices, the crystal that can be obtained is about 7.5 mm [28]. The maximum stable height of the molten zone is determined by gravity. However, with the advent in microgravity research, it has been possible to obtain larger liquid zones. It has been possible to grow GaAs crystals of 20 mm diameter by the floating zone technique during the German Spacelab mission D2 in 1993 [29].

Apart from gravity, the temperature gradient strongly influences the shape and stability of the crystal. The thermocapillary convection in the presence of an encapsulant generates a shear flow and this shear flow has an effect on the float zone or bridge stability. Our interest lies in the stability of the zone in the presence of shear flow. A recirculating pattern appears upon shear-induced motion and the effect of this type of shear flow on the bridge stability is a question of interest. The

focus of the research is on the enhancement of the stability of these bridges by suitably changing the geometry of the end plates or by imposing shear.

Many satellite questions crop up in determining the stability of the liquid zone in the presence of a closed encapsulant: What is the role of the viscosity on the stability of the bridge? What is the role of the centering of the bridge? Do off-center bridges help to stabilize the bridge itself? We will answer these questions in Chapter 5.

The second problem of interest of this research is Rayleigh-Taylor instability. It is well known that if a light fluid underlies a heavy one, the common interface becomes unstable when the width of the interface increases beyond a critical value. The instability is caused by an imbalance between the gravitational and the surface potential energies. The latter always increases upon perturbation and its magnitude depends on the interfacial tension. This problem was first investigated by Rayleigh [30] and then by Taylor [31]. If the fluids are incompressible and have uniform densities, the thicknesses of the fluid layers and the viscosities play no role in determining the critical width, w_c, which is given by $w_c = \pi\sqrt{\frac{\gamma}{g[\rho - \rho^*]}}$. Here, γ is the surface tension, g is the gravitational constant, and ρ and ρ^* are the densities of the heavy and light fluids respectively. The nature of the bifurcation is a backward pitchfork, i.e., when the instability initiates, it progresses to complete breakup.

The interest in studying the stability of a dense liquid lying on top of a light liquid continues because of its applications in other problems. For example, Völtz et al. [32] applied the idea of Rayleigh-Taylor instability to study the interface between glycerin and glycerin-sand in a closed Hele-Shaw like cell. Another different example of Rayleigh-Taylor instability is seen when miscible liquids have been studied either to examine the stability of front moving problems in reaction diffusion systems [33] or to understand the dynamics of the mixing zone in the

nonlinear regime [34]. In this research, we are interested on the effect of geometry and on shear on the stability of the interface in a Rayleigh-Taylor configuration.

The equations that represent both instability problems with corresponding boundary and interface conditions are presented in the next section along with the methods to solve these equations.

CHAPTER 3
A MATHEMATICAL MODEL

This chapter includes the equations used to analyze both instability problems and are given in vector form so that no special coordinate system need be chosen. They can then be adapted to the specific problem of interest. The differences between the problems and further assumptions, which will simplify the governing equations, will be pointed out as each problem is studied.

In the first chapter, we pointed out that the instabilities are related to the nonlinearities in the modeling equations. In this chapter we will observe that the modeling equations are nonlinear because the interface position is coupled to the fluid motion and the two depend upon each other.

3.1 The Nonlinear Equations

In both problems the physical system consists of two immiscible, non-reactive liquids. The fluids are considered to have constant density and viscosity. Therefore, the motion of each fluid is governed by the Navier-Stokes equation, which holds at any point in the domain and boundary and is given by

$$\rho\left[\frac{\partial\vec{v}}{\partial t}+\vec{v}\cdot\nabla\tilde{\mathrm{v}}\right]=-\nabla\mathrm{P}+\rho\vec{g}+\mu\nabla^2\vec{v} \tag{3–1}$$

Here $\vec{v}$ and P are the dimensionless velocity and pressure fields, g is the gravitational constant, ρ and and μ are the density and viscosity of the fluid respectively. A similar equation for the second phase also holds. Mass conservation in each phase is governed by the continuity equations. For each of the phases, it is

$$\nabla\cdot\vec{v}=0 \tag{3–2}$$

Equations 3–1 and 3–2 represent a system of four equations in four unknowns, these being the three components of the velocity and the pressure. We postpone the scaling of the equations as the scales depend on the physical system of interest. Depending on the dimensionless groups that arise, several simplifications can be made all of which will be made later for each problem.

We continue with the modeling equations. All walls are considered to be impermeable, therefore, $\vec{v} \cdot \vec{n} = 0$ holds. Here, $\vec{n}$ is the unit outward normal.

The no-slip condition applies along the walls, and gives rise to $\vec{v} \cdot \vec{t} = 0$ holds. Here, $\vec{t}$ is the unit tangent vector.

At the interface, the mass balance equation is given by

$$\rho \left(\vec{v} - \vec{u}\right) \cdot \vec{n} = 0 = \rho^* \left(\vec{v}^* - \vec{u}\right) \cdot \vec{n} \tag{3–3}$$

In the above equation u represents the surface speed. This equation yields two interface conditions as there is no phase-change at the interface. Note that the asterisk denotes the second phase.

At the interface, the tangential components of velocities of both fluids are equal to each other, i.e.,

$$\vec{v} \cdot \vec{t} = \vec{v^*} \cdot \vec{t} \tag{3–4}$$

The interfacial tension at the interface comes into the picture through the force balance, which satisfies

$$P\vec{\vec{I}} \cdot \vec{n} + \mu \left[\nabla \vec{v} + \left[\nabla \vec{v}\right]^T\right] \cdot \vec{n} - P^* \vec{\vec{I}} \cdot \vec{n} - \mu^* \left[\nabla \vec{v^*} + \left[\nabla \vec{v^*}\right]^T\right] \cdot \vec{n} = \gamma 2H\vec{n} \tag{3–5}$$

where γ is the interfacial tension and $2H$ is the surface mean curvature. Observe that as the direction of the normal determines the sign of the right hand side, we don't want to specify its sign yet. The reader is referred to Appendix B for the derivation of the surface variables in Cartesian and cylindrical coordinate systems.

The tangential and the normal stress balances are obtained by taking the dot product of Equation 3–5 with the unit tangent and normal vectors respectively.

Finally, the volumes of both liquids must be fixed, i.e.,

$$\int_V dV = V_0 \tag{3–6}$$

where V_0 is the original volume of one of the liquids. Equation 3–6 implies that a given perturbation to the liquids does not change their volumes. This volume constraint is the last condition needed to close the problem.

As we mentioned, the equations are nonlinear. The first nonlinearity is observed in the domain equation because of the $\vec{v} \cdot \nabla \vec{v}$ term. However, in most of the problems we study, as we will see in the following section, the base state is quiescent and this term is usually not needed. The main nonlinearity comes from the fact that the interface position depends on the fluid motion and the fluid motion depends on the position of the interface. This nonlinearity is seen vividly in the normal stress balance at the interface for it is an equation for the interface position. To investigate the instability arising from small disturbances we move on to the linearization of the equations.

3.2 The Linear Model

As our interest is primarily in the onset of instability, it is sufficient to analyze a linearized model where the linearization is done about a base state. The importance of linearization calls for an explanation.

The instability arises when a system, which was in equilibrium, is driven away from the equilibrium state when small disturbances are imposed upon it and when a control parameter exceeds a critical value. For example in the liquid bridge problem, the control parameter may be the length of the bridge of a given radius or it may be the width of the container in the Rayleigh-Taylor problem. An equilibrium system is said to be stable if all disturbances imposed upon it

damp out over time and said to be unstable when they grow in time. Now if the system becomes unstable to infinitesimal perturbations at some critical value of the control parameter it is unconditionally unstable. It is crucial to note that the disturbances are taken to be small for if a state is unstable to infinitesimal disturbances it must be unstable to all disturbances. Also, this assumption leads to the local linearization of the system. The theoretical approach that is taken when studying the instability of the physical system is therefore to impose infinitesimal disturbances on the base state and to linearize the nonlinear equations describing the system around this base state. It should be pointed out that the base state is always a solution to the nonlinear equations and often it might seem defeating to look for a base state if it means solving these nonlinear equations. However, in practice for a large class of problems the base state is seen almost by inspection or by guessing it. For example, for a stationary cylindrical liquid bridge in zero gravity, it is obvious that the base state is the quiescent state with a vertical interface. On the other hand, for some other problems, one might need to determine the flow profile in the base state as seen in the shear-induced Rayleigh-Taylor problem. Often, we try to simplify the governing equations by making assumptions such as creeping flow or an inviscid liquid. These assumptions are employed if there is no loss of generality in the physics that we are interested. Most of the time these simplifications can be introduced after the nonlinear equations are made dimensionless.

Calling the base state variable for velocity, $\vec{v}_0$, and indicating the amplitude of the perturbation by ϵ, the velocity and all dependent variables can be expanded as

$$\vec{v} = \vec{v}_0 + \epsilon \left[\vec{v}_1 + z_1 \frac{\partial \vec{v}_0}{\partial z} \right] + \cdots \tag{3–7}$$

Here z_1 is the mapping from the current state to the base state at first order. Its meaning is explained in the Appendix A and, at the interface, the mapping at this

order is denoted by Z_1, a variable, which needs to be determined during the course of the calculation. Note that the subscripts represent the order of the expansion, e.g. the base state variables are represented by a subscript zero. We can further expand v_1 and other subscript 'one' variables using a normal mode expansion. Consequently, the time and the spatial dependencies of the perturbed variables are separated as

$$\vec{v_1} = \vec{\hat{v_1}} e^{\sigma t} \tag{3–8}$$

where σ is the inverse time constant also known as the growth or decay constant. The critical point is attained when the real part of σ vanishes.

We will discuss Rayleigh-Taylor instability in the next chapter and apply the model developed in this chapter to this problem.

CHAPTER 4
THE RAYLEIGH-TAYLOR INSTABILITY

In this chapter, the instability of a flat interface between two immiscible fluids where the light fluid underlies the heavy one is studied. The chapter is composed of four sections. In the first section, we will employ Rayleigh's work principle to find the critical width, introduced in Chapter 2, which is given by $w_c = \pi\sqrt{\dfrac{\gamma}{g[\rho - \rho^*]}}$. In the second section, we obtain the same result by a perturbation calculation, with a companion nonlinear analysis. The linear calculation is used in the third section where a similar perturbation calculation in conjunction with another type of perturbation is used to study the effect of a slightly deviated circular cross section in the form of an elliptical cross section on the stability point. In the last section we study the effect of shear on the Rayleigh-Taylor (RT) instability with a linear and nonlinear analysis.

4.1 Determining The Critical Width in Rayleigh-Taylor Instability by Rayleigh's Work Principle

The physical problem is sketched in Figure 4-1. A heavy fluid of density ρ lies above a light fluid of density ρ^* in a container of width w. We will make use of the Rayleigh work principle as adapted from Johns and Narayanan [10] to determine the critical width at which the common interface becomes unstable.

According to the Rayleigh work principle the stability of a system to a given disturbance is related to the change of energy of the system where the total energy of the system is the sum of gravitational and surface potential energies. The change in the latter can be determined directly from the change in the surface area multiplied by its surface tension [35]. Consequently, the critical or neutral point is attained when there is no change in the total energy of the system for a given

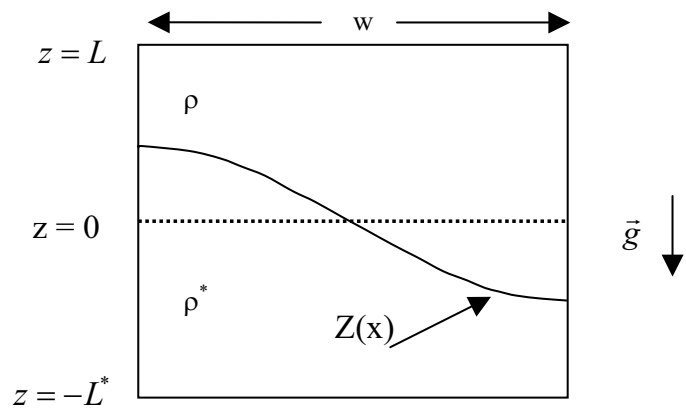

Figure 4-1. Sketch of the physical problem depicting two immiscible liquids with the heavy one on top of the light one.

disturbance. To set these thoughts to a calculation, let the displacement be

$$z = Z\left(x\right) = \epsilon \cos(kx) \tag{4–1}$$

where ϵ represents the amplitude of the disturbance, assumed to be small, and k is the wave number given by $n\pi/w$, where $n = 1, 2, \cdots$. The surface area is given by

$$A = \int_0^w \frac{ds}{dx} dx \tag{4–2}$$

where ds is the arc length, given by $ds = \left[1 + \left[\frac{dz}{dx}\right]^2\right]^{1/2} dx \approx \left[1 + \frac{1}{2}\left[\frac{dz}{dx}\right]^2\right] dx$. To order ϵ^2, the change in the potential energy can be written as

$$\gamma \int_0^w \left[1 + \frac{1}{2} Z_x^2\right] dx - \gamma \int_0^w dx \tag{4–3}$$

Note that the system is in two-dimensions and the above equation is in fact the energy per unit depth. Using $Z_x = -\epsilon k \sin\left(kx\right)$, Equation 4–3 becomes

$$\gamma \frac{1}{4} \epsilon^2 k^2 w \tag{4–4}$$

The change in the gravitational potential energy per unit depth is given by

$$\int_0^w \int_Z^L \rho g z dz dx + \int_0^w \int_{-L^*}^Z \rho^* g z dz dx - \int_0^w \int_0^L \rho g z dz dx - \int_0^w \int_{-L^*}^0 \rho^* g z dz dx \tag{4–5}$$

Substituting the expression for Z, simplifies the above equation to

$$\epsilon^2 \frac{1}{2} g \left[-\rho \int_0^w \cos^2(kx)\, dx + \rho^* \int_0^w \cos^2(kx)\, dx \right] = -\frac{1}{4} g \left[\rho - \rho^*\right] \epsilon^2 w \tag{4–6}$$

The total energy change is therefore the sum of the energies given in Equations 4–4 and 4–6, i.e.

$$\frac{1}{4} \epsilon^2 w \left[\gamma k^2 - g\left[\rho - \rho^*\right]\right] \tag{4–7}$$

The critical point is attained when there is no change in the energy. Substituting $k = \pi/w$ into Equation 4–7, the critical width is obtained as

$$w_c = \pi \sqrt{\frac{\gamma}{g[\rho - \rho^*]}} \tag{4–8}$$

For all widths smaller than this, the system is stable. It is noteworthy that the depths of the liquids play no role in determining the critical width.

In the next section, the same result is obtained by a perturbation calculation and a weakly nonlinear analysis follows.

4.2 A Simple Derivation For The Critical Width For The Rayleigh-Taylor Instability and The Weakly Nonlinear Analysis of the Rayleigh-Taylor Problem

A simple perturbation calculation is used to determine the critical width at which a heavy liquid on top of air becomes unstable and a weakly nonlinear analysis is performed to determine the bifurcation type.

The physical problem is sketched in Figure 4-1. The bottom fluid in this calculation is taken as air. The liquid is assumed to be inviscid.

The Euler and continuity equations are

$$\rho\vec{v}\cdot\nabla\vec{v} = -\nabla P + \rho\vec{g} \tag{4–9}$$

and

$$\nabla\cdot\vec{v} = 0 \tag{4–10}$$

These domain equations will be solved subject to the force balance and no mass flow at the interface conditions given in Chapter 3, namely,

$$P = \gamma 2H \tag{4–11}$$

and

$$\vec{n}\cdot\vec{v} = \vec{n}\cdot\vec{u} \tag{4–12}$$

The base state is assumed to be stationary. To investigate the stability of the base state, linear stability analysis described in Chapter 3 is employed. For the perturbed problem, the equation of motion and the continuity equation results in

$$\nabla^2 P_1 = 0 \tag{4–13}$$

The walls are impermeable to flow; as a result the normal component of the velocity is zero, or in terms of pressure we can write

$$\vec{n}_0\cdot\nabla P_1 = 0 \tag{4–14}$$

Free end conditions are chosen for the contact of the liquid with the solid sidewalls, i.e.,

$$\frac{dZ_1}{dx} = 0 \tag{4–15}$$

Therefore, each variable can be expanded as a cosine function in the horizontal direction, e.g., $Z_1 = \hat{Z}_1\cos(kx)$ where $k = {}^{n\pi}/_{w}$. From the no-flow condition we get

P_1 as a constant. Finally, the normal stress balance reads as

$$P_1 + Z_1 \frac{dP_0}{dz} = \gamma \frac{d^2 Z_1}{dx^2} \tag{4–16}$$

Using the constant-volume requirement, which states $\int_0^w Z_1 dx = 0$, the perturbed pressure, which was already found to be a constant, is determined to be zero. Also, Z_1 is found as $A\cos(kx)$. The critical point is determined by rewriting Equation 4–16 as

$$\left[-\rho g + \gamma k^2\right] Z_1 = 0 \tag{4–17}$$

The square of the critical wave number is $\frac{\rho g}{\gamma} = G$. Substituting $k = \pi/w$, the critical width is obtained as

$$w_c = \pi \sqrt{\frac{\gamma}{g\rho}} \tag{4–18}$$

which is same as Equation 4–8. Now, our aim is to find what happens when the critical point is advanced by a small amount as $G = G_c + \epsilon^2$. The responses of the variables to this change in the critical point are given as

$$Z = \sum_j \frac{1}{j!} \varepsilon^j Z^j \tag{4–19}$$

Before moving to the weakly nonlinear analysis, let's rewrite the domain equation as

$$\frac{\rho}{\gamma} \vec{v} \cdot \nabla \vec{v} = -\frac{1}{\gamma} \nabla P - G\vec{k} \tag{4–20}$$

When the expansions are substituted into the nonlinear equations, to the lowest order in ϵ, the base state problem, to the first order, the eigenvalue problem where the critical point is determined, are recovered. The second order domain equation becomes

$$0 = -\frac{1}{\gamma} \nabla P_2 - 2\vec{k} \tag{4–21}$$

Both the domain equation and the no-mass transfer condition at the interface gives

$$0 = -\frac{1}{\gamma}\frac{dP_2}{dz} - 2 \tag{4–22}$$

Hence, P_2 is a constant. The normal stress balance at this order is

$$P_2 + Z_2\frac{dP_0}{dz} = \gamma\frac{d^2Z_2}{dx^2} \tag{4–23}$$

The pressure, which is a constant, turns out to be equal to zero by using the constant volume requirement. Therefore Z_2 is found as $B\cos(kx)$. To determine the value of A, hence the type of the bifurcation, the third order equations are written. The domain equation is

$$\frac{dP_3}{dz} = 0 \tag{4–24}$$

P_3 turns out to be a constant as in the previous orders. The normal stress balance at the third order is

$$P_3 + Z_3\frac{dP_0}{dz} + 3Z_1\frac{dP_2}{dz} = \gamma\left[\frac{d^2Z_3}{dx^2} - 9\frac{d^2Z_1}{dx^2}\left[\frac{dZ_1}{dx}\right]^2\right] \tag{4–25}$$

Observe that at this order there is a contribution to the pressure from the second order and the denominator of the curvature also shows its signature at this order. P_3 turns out to be equal to zero as in the previous orders. Solvability condition gives

$$-6\gamma A\int_0^w \cos^2(kx)\,dx - 9\gamma A^3k^4\int_0^w \cos^2(kx)\sin^2(kx)\,dx = 0 \tag{4–26}$$

which can be simplified to

$$-3A - \frac{9}{8}A^3k^4 = 0 \tag{4–27}$$

As A^2 is negative, G needs to be written as $G = G_c - \epsilon^2$ which yields a positive A^2. Therefore, the bifurcation type is a backward pitchfork.

4.3 The Effect of the Geometry on the Critical Point in Rayleigh-Taylor Instability: Rayleigh-Taylor Instability with Elliptical Interface

The breakup point of the RT instability with an elliptical interface is compared to the RT instability with a circular interface. An enhancement in the stability is obtained theoretically. It is assumed that the circular cross section will be subject to only axisymmetric disturbances. The physical argument for the enhanced stability is related to the dissipation of the disturbances. In a circular geometry, this is achieved by radial dissipation. In an elliptical geometry dissipation can also occur azimuthally.

The physical problem is sketched in Figure 4-2. Observe that the radial position depends on the azimuthal angle.

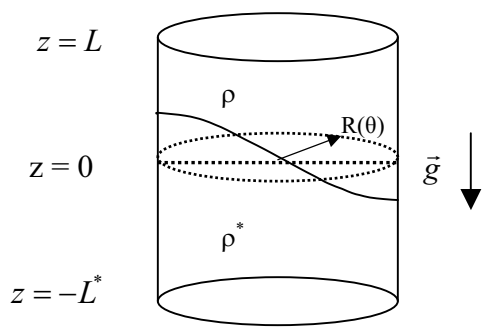

Figure 4-2: Sketch of the Rayleigh-Taylor problem for an elliptical geometry.

The modeling equations determining the fate of a disturbance are introduced in Chapter 3. In this problem, we are considering inviscid liquids and the base state is a quiescent state where the interface is flat. Therefore the nonlinear equations have at least one simple solution. It is

$$\vec{v}_0 = \vec{0}, \quad P_0 = -\rho g z \quad , \quad \vec{v}_0^* = \vec{0}, \quad \text{and} \quad P_0^* = -\rho^* g z \tag{4–28}$$

and $Z_0 = 0$. We are interested in the stability of this base state to small disturbances. For that purpose we turn to perturbed equations. The interface position

can be expanded as

$$z = Z\left(r, \theta, t, \epsilon\right) = Z_0 + \epsilon Z_1 + \frac{1}{2}\epsilon^2 Z_2 + \cdots \tag{4–29}$$

To first order upon perturbation, the equations of motion and continuity are

$$\rho \frac{\partial \vec{v}_1}{\partial t} = -\nabla P_1 \quad \text{and} \quad \nabla \cdot \vec{v}_1 = 0 \tag{4–30}$$

in the region $Z\left(r, \theta, t, \epsilon\right) \leq z \leq L$. Combining the two equations we get

$$\nabla^2 P_1 = 0 \tag{4–31}$$

with similar equation for the '*' fluid. The corresponding boundary conditions are also written in the perturbed form. The no-flow condition at the sidewalls is written as

$$\vec{n}_0 \cdot \vec{v}_1 = 0 = \vec{n}_0 \cdot \vec{v}_1^* \tag{4–32}$$

which is valid at $r = R\left(\theta\right)$. Before introducing the remaining boundary conditions, we want to draw the attention of the reader to this boundary condition. The equation is written at the boundary, which depends on the azimuthal angle. This is an inconvenient geometry. Therefore, to be able to carry out the calculation in a more convenient geometry, we want to use perturbation theory and write the equations at the reference state, which has a circular cross section.

The objective is to show that the RT problem with elliptical interface is more stable than a companion RT problem where the interface is circular. The area of the ellipse is assumed to be the same as that of the circle. Also, the ellipse is assumed to deviate from the circle by a small amount so that a perturbation calculation can be used. As the ellipse is considered as a perturbation of the ellipse, first the mapping obtaining an ellipse from a circle needs to be determined.

Assume that the ellipse is deviated from the circle by a small amount δ so that the semi-major axis "a" of the ellipse is defined as $a = R^{(0)}\left[1 + \delta\right]$, where is the

radius of the circle from which the ellipse is deviated. Then, the semi-minor axis "b" of the ellipse is calculated by keeping the areas to be the same, i.e.,

$$\pi {R^{(0)}}^2 = \pi ab$$

leading to

$$b \cong R^{(0)} \left[1 - \delta + \delta^2\right]$$

Observe that the surface position of the ellipse can be expanded in powers of as

$$R = R^{(0)} + \delta R^{(1)} + \frac{1}{2}\delta^2 R^{(2)} + \cdots \tag{4–33}$$

The mappings R_1 and R_2 can be found using the equation for ellipse, which is given by

$$\frac{x^2}{a^2} + \frac{y^2}{b^2} = 1 \tag{4–34}$$

Substituting the definitions for x, and y, which are $R\cos(\theta)$ and $R\sin(\theta)$, respectively, also making use of the expansions for a, b, and R, one gets the mappings as

$$R^{(1)} = R^{(0)} \cos(2\theta)\, a \tag{4–35}$$

to first order in δ , and

$$R^{(2)} = R^{(0)} \left[-\frac{1}{2} - \cos(2\theta) + \frac{3}{2}\cos(4\theta)\right] \tag{4–36}$$

to second order in δ.

The geometry of the physical system is determined through a perturbation calculation. Now, we can return to our perturbation calculation.

The no-flow boundary conditions at the reference interface, i.e., $z = 0$, and at the top wall, i.e., $z = H$, for the perturbed pressure can be written as

$$\frac{\partial P_1}{\partial z} = 0 \tag{4–37}$$

Therefore P_1 is a constant, which is found at each order in δ using constant-volume requirement. At the outer wall, the contact angle condition reads as

$$\frac{\partial Z_1}{\partial r} - \frac{1}{R^2}\frac{\partial R}{\partial \theta}\frac{\partial Z_1}{\partial \theta} = 0 \tag{4–38}$$

The normal stress balance at the interface is

$$P_1 + Z_1\frac{\partial P_0}{\partial z} = \gamma\left[\nabla^2 Z_1\right] \tag{4–39}$$

where $\frac{\partial P_0}{\partial z} = -\rho g$ and P_1 is equal to a constant and $\frac{P_1}{\gamma} = c_1$. Equation 4–39 can be rewritten as

$$c_1 - \lambda^2 Z_1 = \nabla^2 Z_1 \tag{4–40}$$

where $\lambda^2 = \frac{\rho g}{\gamma}$. Now, each variable is expanded in powers of δ as

$$Z_1 = Z_1^{(0)} + \delta Z_1^{(1)} + \frac{1}{2}\delta^2 Z_1^{(2)} + \cdots \tag{4–41}$$

Similarly λ, which determined the critical point is expanded as

$$c_1 - \lambda^2 Z_1 = \nabla^2 Z_1 \lambda^2 = \lambda^{(0)^2} + \delta\lambda^{(1)^2} + \frac{1}{2}\delta^2\lambda^{(2)^2} + \cdots \tag{4–42}$$

Here, $\lambda^{(0)^2}$ represents the critical point of the circle to axisymmetric disturbances. Higher order terms in λ are the corrections going from a circle to an ellipse.

To zeroth order in δ, the RT problem with a circular cross-section is recovered. The normal stress balance at this order is

$$c_1^{(0)} - \lambda^{(0)^2} Z_1^{(0)} = \nabla^2 Z_1^{(0)} \tag{4–43}$$

From the above equation, $Z_1^{(0)} = AJ_0\left(\lambda^{(0)}R^{(0)}\right) + \frac{c_1^{(0)}}{\lambda^{(0)^2}}$. The constant $c_1^{(0)}$ becomes zero when the constant-volume requirement is applied. Therefore $Z_1^{(0)}$ turns out to be

$$Z_1^{(0)} = AJ_0\left(\lambda^{(0)}R^{(0)}\right) \tag{4–44}$$

At the outer wall, $\dfrac{\partial Z_1^{(0)}}{\partial r} = 0$. Consequently, $\lambda^{(0)}R^{(0)}$ are found from $J_1\left(\lambda^{(0)}R^{(0)}\right) = 0$.

To first order in δ, the normal stress balance is given by

$$-\lambda^{(1)^2} Z_1^{(0)} - \lambda^{(0)^2} Z_1^{(1)} = \nabla^2 Z_1^{(1)} \tag{4–45}$$

At the outer wall, $\dfrac{\partial Z_1^{(1)}}{\partial r} + R^{(1)}\dfrac{\partial^2 Z_1^{(0)}}{\partial r^2} = 0$. Therefore, $Z_1^{(1)} = \hat{Z}_1^{(1)}(r)\cos(2\theta)$. To find the constant $\lambda^{(1)^2}$, the solvability condition is applied, i.e., Equation 4–43 is multiplied with $Z_1^{(1)}$ and integrated over the surface, from which the integral of the product of Equation 4–45 with $Z_1^{(0)}$ is subtracted. It turns out that $\lambda^{(1)^2} = 0$ as one would have expected. It means that the major and minor axis of the ellipse can be flipped and the same result would be still valid. The form of $Z_1^{(1)}$ can be found from Equation 4–45 as

$$Z_1^{(1)} = BJ_2\left(\lambda^{(0)}R^{(0)}\right)\cos(2\theta) \tag{4–46}$$

The constant B is found from the outer wall condition as

$$B = -\frac{A}{2}\left(\lambda^{(0)}R^{(0)}\right)^2 \frac{J_0\left(\lambda^{(0)}R^{(0)}\right)}{J_2\left(\lambda^{(0)}R^{(0)}\right)} \tag{4–47}$$

A similar approach is taken at second order in δ. The normal stress balance at this order is

$$-\lambda^{(2)^2} Z_1^{(0)} - \lambda^{(0)^2} Z_1^{(2)} = \nabla^2 Z_1^{(2)} \tag{4–48}$$

The solvability condition gives

$$\lambda^{(2)^2}\int_0^{R^{(0)}} Z_1^{(0)^2} r dr = -R^{(0)} Z_1^{(0)} \frac{d\hat{Z}_1^{(2)}}{dr}\left(r = R^{(0)}\right) \tag{4–49}$$

where $\hat{Z}_1^{(2)}$ is the θ independent part of $Z_1^{(2)}$. $Z_1^{(0)}$ is known, and $\hat{Z}_1^{(2)}$ can be found from the outside wall condition given as

$$\frac{\partial Z_1^{(2)}}{\partial r} + 2R^{(1)}\frac{\partial^2 Z_1^{(1)}}{\partial r^2} + R^{(1)^2}\frac{\partial^3 Z_1^{(0)}}{\partial r^3} + R^{(2)}\frac{\partial^2 Z_1^{(0)}}{\partial r^2} - \frac{2}{R^{(0)^2}}\frac{\partial Z_1^{(1)}}{\partial \theta}\frac{\partial R^{(1)}}{\partial \theta} = 0 \tag{4–50}$$

After some algebraic manipulations, an equation for $\lambda^{(2)^2}$ is obtained as

$$\lambda^{(2)^2} = 3.83^2 \lambda^{(0)^2} \tag{4–51}$$

As $\lambda^{(2)^2}$ is a positive number, the stability point is enhanced, which was expected because of the dissipation of the disturbances argument.

4.4 Linear and Weakly Nonlinear Analysis of the Effect of Shear on Rayleigh-Taylor Instability

In this section, the effect of shear on the RT instability is studied. Two cases are considered: an open channel Couette flow and a closed two-dimensional flow in a driven cavity. We will show that in the case of open channel flow, the critical point remains unchanged compared to the classical Rayleigh-Taylor (RT) instability, but it exhibits oscillations and the frequency of these oscillations depends linearly on the wall speed. It is shown in Appendix D that such a result also obtains if creeping flow is assumed while destabilization can be obtained if only inertia is taken into account. The closed flow geometry is however different. It is shown in this chapter that shearing the fluids by moving the walls stabilizes the classical RT problem even in the creeping flow limit provided a flat interface is an allowable base solution. This result would obtain only if both fluid layers are taken as active. An interesting conclusion of the closed flow case is that for a selected choice of parameters, three different critical points can be obtained. Therefore, there is a second window of stability for the shear-induced RT problem. To understand the nature of the bifurcation, a weakly nonlinear analysis is applied via a dominant balance method by choosing the scaled wall speed (i.e., Capillary number) as the control parameter. It will be shown that the problem has either a backward or forward pitchfork bifurcation depending on the critical point.

The interest in the effect of shear on the interfacial instability is not new. Chen and Steen [36] showed that when constant shear is applied to a liquid that is

above an ambient gas, a return flow is created in the liquid deflecting the interface. Given that the symmetry is broken, the stability point is reduced, i.e., the critical width at which the interface breaks up is lower than the classical RT limit given earlier. However, if a flat interface is possible, the situation may be different. The importance of a flat interface at the base state is seen in various other interfacial instability problems; for example Hsieh [37] studied the RT instability for inviscid fluids with heat and mass transfer. He was able to show that evaporation or condensation enhances the stability when the interface is taken to be flat in the base state. Ho [38] advanced this problem by adding viscosity to the model while considering the lateral direction to be unbounded. With a flat base state, these authors were able to obtain more stable configurations than the classical RT problem. The reason for the stability of an interface of constant curvature during evaporation is due to the fluid flow in the vapor, which tends to reduce interfacial undulations and is even seen in problems of convection with phase change [39]. There are other problems where the stability of a constant curvature base state has been enhanced either by imposing potential that induce shear [40]. These works motivate us to study the effect of shear on the RT problem with a constant curvature base state and inquire whether the critical width of the interface changes and if so, why and by how much. In many interfacial instability problems the physics of the instability is studied by explaining the shape of the growth curves where a growth constant, σ, is graphed against a disturbance wave number and in most, but not all problems the curve shows a maximum growth rate at non-zero values of the wave number. Here too, it is our aim to understand the physics of shear effects by considering similar growth rate curves where the wave number is replaced by scaled container width. Finally, it is of interest to see what the nature of the bifurcation becomes when shear is imposed on the RT problem. To these ends we move to a model.

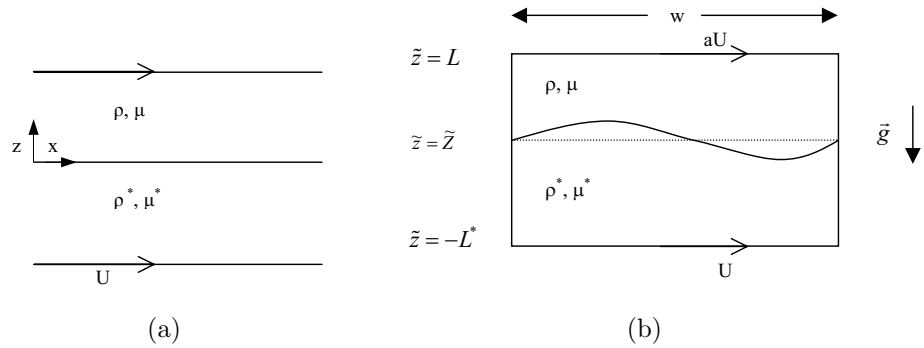

Figure 4-3. Two immiscible liquids with density stratification a) Open channel flow b) Closed flow.

The physical problem consists of two immiscible liquids where the heavy one overlies the light one when shear is present. The shear is introduced by moving the lower and bottom walls at constant speed. The parameters in the problem such as the depths of the liquid compartments, the physical properties of the liquids and the wall speeds are tuned to attain a flat interface between the two liquids. Two problems are considered in this study. In the first, the horizontal extent is taken to be infinity, while in the second, the fluids are enclosed by vertical sidewalls. The purposes of considering the open channel flow problem are to introduce necessary terminology and to understand some important characteristics, which will be instructive when considering the closed flow problem. A sketch of the physical problem can be seen in Figure 4-3.

The two configurations seen in Figure 4-3 are quite different from each other. In both, a heavy liquid is on top of the light one and shear is created by moving the walls. The waves travel in the open channel flow whereas in the closed flow, the perturbations are impeded by the walls. In fact, the presence of the sidewalls creates a return flow, which ought to affect the stability of the interface. In the open channel flow, the speed of the lower and upper walls must be

different otherwise no effective motion will be observed. In both configurations, it is assumed that the walls are moved slowly enough so that the inertia is ignored.

The scaled equation of motion and the continuity equation for a constant density fluid with the creeping flow assumption are given by

$$\nabla P = -B\vec{i_z} + \nabla^2 \mathbf{v} \tag{4–52}$$

$$\nabla \cdot \vec{v} = 0 \tag{4–53}$$

Equations 4–52 and 4–53 are valid in $Z(x) \leq z \leq 1$. Similar equations for the lower phase can be written as

$$\nabla P^* = -B^*\vec{i_z} + \frac{\mu^*}{\mu}\nabla^2\vec{v^*} \tag{4–54}$$

$$\nabla \cdot \vec{v^*} = 0 \tag{4–55}$$

The lower liquid is represented by *. The velocity scale is $\bar{v}$ and is chosen to be the capillary velocity, i.e., γ/μ where μ is the viscosity of the upper liquid. The over-bars represent the scale factors. The pressure scale $\bar{P}$ is given by $\mu\bar{v}/\bar{L}$. The length scale is taken to be the upper compartment's depth, L. The dimensionless variables B and B^* are given by $\dfrac{g\rho\bar{L}^2}{\gamma}$ and $\dfrac{g\rho^*\bar{L}^2}{\gamma}$ respectively. Now the domain equations must be solved subject to boundary conditions. At the solid walls no-slip and no-flow conditions hold. They are expressed as

$$v_x^* = Ca \quad \text{and } v_z^* = 0 \tag{4–56}$$

Note that, the no-slip condition at the bottom wall gives rise to the Capillary number, i.e. $v_x^* = \frac{\mu U}{\gamma} = Ca$, where v_x^* is the x-component of the scaled velocity. Similar equations can be written at the top wall. In addition to the conditions at the top and bottom walls other conditions hold at the fluid-fluid interface. Here, mass transfer is not permitted, the no-slip condition and the force balance hold.

Also, the volumes of both liquids must be fixed. These conditions are given in Chapter 3 and will not be repeated here.

For the closed flow problem, the boundary conditions on the vertical walls, which are located at $x = 0$ and w/L are also specified. These walls are impermeable and to get an analytic solution are assumed to be stress-free. These boundary conditions translate into

$$v_x = 0 = v_x^* \text{ and } \frac{\partial v_z}{\partial x} = 0 = \frac{\partial v_z^*}{\partial x} \tag{4–57}$$

We are using linear stability analysis as described in Chapter 3. The role of the wall speed on the critical point is questioned. The first problem, i.e., the instability in open channel flow is presented in the next section.

4.4.1 Instability in Open Channel Couette Flow

In the open flow problem the bottom wall is moved with a constant speed U while the top wall is kept stationary as only the relative motion of the walls is important. Recall that the physical problem is sketched in Figure 4-3(a).

The conditions for a flat interface in the base state are determined by using the normal stress balance at the interface. For a given viscosity ratio, a relation between the wall speed and the ratio of the compartment lengths is established. It turns out that if the viscosities of both liquids and the liquid depths are the same, then the normal stress balance is automatically satisfied. The base state velocity profile in the horizontal direction, i.e. $v_{x,0}$, is linear whereas $v_{z,0}$ is equal to zero. To determine the stability of this base state, the perturbed state is solved by eliminating $v_{x,1}$ in favor of $v_{z,1}$ by using the continuity equation. Consequently, the domain equation for the perturbed state becomes

$$\nabla^4 v_{z,1} = 0 \tag{4–58}$$

where the ∇^4 operator is defined as $\frac{\partial^4}{\partial x^4} + \frac{\partial^4}{\partial z^4} + 2\frac{\partial^4}{\partial x^2 \partial z^2}$. A similar equation is valid for the * phase. First, the time dependence of the velocity is separated by using Equation 3–8. Then, $\hat{v}_{z,1}$ is assumed to be $\hat{\hat{v}}_{z,1}(z)\, e^{ikx}$ where k is the wave number. From Equation 4–58, the form of the velocity can be expressed as

$$\hat{\hat{v}}_{z,1}(z) = C_1 e^{kz} + C_2 z e^{kz} + C_3 e^{-kz} + C_4 z e^{-kz}$$

Hereafter, the double hat symbol is dropped. To solve for the constants in the above equation, the perturbed boundary conditions are imposed. The perturbed no-penetration and no-slip conditions at the top wall are

$$v_{z,1} = 0 \text{ and } \frac{dv_{z,1}}{dz} = 0 \tag{4–59}$$

A similar equation is valid at the bottom wall. At the interface the perturbed no-mass transfer condition becomes

$$v_{z,1} = v^*_{z,1} \text{ and } v_{z,1} = ikZ_1 v_{x,0} + \sigma Z_1 \tag{4–60}$$

and the perturbed no-slip condition at the interface is

$$\frac{dv_{z,1}}{dz} = \frac{dv^*_{z,1}}{dz} \tag{4–61}$$

while the perturbed tangential stress balance is given by

$$\frac{d^2 v_{z,1}}{dz^2} = \frac{d^2 v^*_{z,1}}{dz^2} \tag{4–62}$$

The perturbed velocities $v_{z,1}$ and $v^*_{z,1}$ are found in terms of σ and Z_1 by using the above equations. Then, these expressions for the velocities are substituted into the normal stress balance, which is given by

$$P_1 + Z_1 \frac{\partial P_0}{\partial z} - 2\frac{\partial v_{z,1}}{\partial z} - P^*_1 - Z_1 \frac{\partial P^*_0}{\partial z} + 2\frac{\mu^*}{\mu}\frac{\partial v^*_{z,1}}{\partial z} = \frac{d^2 Z_1}{dx^2} \tag{4–63}$$

The pressure terms from the normal stress balance are eliminated by using the equations of motion. After these substitutions, Equation 4–63 becomes

$$\frac{d^3 v_{z,1}}{dz^3} - 3k^2 \frac{dv_{z,1}}{dz} - \frac{\mu^*}{\mu}\left[\frac{d^3 v^*_{z,1}}{dz^3} - 3k^2 \frac{dv^*_{z,1}}{dz}\right] + k^2 Z_1 \left[Bo - k^2\right] = 0 \tag{4–64}$$

where Bo is the Bond number defined as $Bo = \dfrac{gL^2\left[\rho - \rho^*\right]}{\gamma}$. From Equation 4–64, after some algebra it is found that the neutral point of the open channel flow is the same as that of the classical RT problem but that the neutral point is an oscillatory state, i.e. the imaginary part of σ is not zero. This result is in agreement with physical intuition. One might expect that the real part of the growth constants would be independent of Capillary number as they must be independent of the direction of the wall movement. It must be noted that the growth constant cannot depend on the square of Ca, as the base state problem is homogeneous in the first power of Ca. The imaginary part of σ, on the other hand, must appear in conjugate pairs and therefore must depend homogenously on Ca. In general, the oscillation at the critical point is not surprising because the perturbations are carried with the moving bottom wall and they are not impeded in the horizontal direction. This will change in the second problem where the shear induced RT instability in a closed container, is studied.

4.4.2 Rayleigh-Taylor Instability in Closed Flow

In this problem, the top and bottom walls are moved at constant speeds. The wall speeds, the liquid depths and the viscosities are the parameters to be determined to get a flat interface. The governing equations were presented earlier along with the boundary and interface conditions. To simplify the calculation, a stream function form is introduced. The stream function is defined via

$$v_x = -\frac{\partial \psi}{\partial z} \quad \text{and } v_z = \frac{\partial \psi}{\partial x} \tag{4–65}$$

After taking the curl of the equation of motion

$$\nabla^4\psi = 0 \;\text{ for }\; 0 < x < w/L \;\text{ and }\; Z < z < 1$$

and (4–66)

$$\nabla^4\psi^* = 0 \;\text{ for }\; 0 < x < w/L \;\text{ and} - \mathrm{L}^*/L < z < Z$$

are obtained. The solution to a similar fourth order equation can be found in [41]. For stress-free sidewalls, the solution can be written as

$$\psi = \sum_n \sin(kx)\,\hat{\psi}_n(z) \tag{4–67}$$

where $k = \dfrac{n\pi}{w/L}$ with $n = 1, 2, \cdots$ and $\hat{\psi}_n(z) = Ae^{kz} + Bze^{kz} + Ce^{-kz} + Dze^{-kz}$. This stream function is expanded around a base state ψ_0 and the stability of this base state is investigated.

The base state: The domain equations for the base state in terms of stream functions are

$$\nabla^4\psi_0 = 0 \;\text{ for }\; 0 < x < w/L \;\text{ and }\; 0 < z < 1$$

and (4–68)

$$\nabla^4\psi_0^* = 0 \;\text{ for }\; 0 < x < w/L \;\text{ and} - \mathrm{L}^*/L < z < 0$$

where

$$\psi_0 = \sum_{n_0} \sin(k_0 x)\,\hat{\psi}_{0,n_0}(z)$$

The z-dependent part of the stream function is given as

$$\hat{\psi}_{0,n_0}(z) = A_0 e^{k_0 z} + B_0 z e^{k_0 z} + C_0 e^{-k_0 z} + D_0 z e^{-k_0 z}$$

where $k_0 = \dfrac{n_0\pi}{w/L}$ with $n_0 = 1, 2, \cdots$. A similar result can be obtained for the * phase. At the top wall, no-penetration and no-slip imply

$$v_{x,0} = aCa \quad \Rightarrow \quad \sum_{n_0} \sin\left(k_0 x\right) \frac{d\hat{\psi}_{0,n_0}}{dz} = -aCa$$

and (4–69)

$$v_{z,0} = 0 \quad \Rightarrow \quad \hat{\psi}_{0,n_0} = 0$$

Similar equations can be written for the bottom wall. First, a flat interface for the base state is assumed and then the conditions that allow it are found from the normal component of the interfacial force balance. Now, at the interface, the mass balance turns into

$$v_{z,0} = 0 = v^*_{z,0} \Rightarrow \hat{\psi}_{0,n_0} = 0 = \hat{\psi}^*_{0,n_0} \tag{4–70}$$

The no-slip condition becomes

$$v_{x,0} = v^*_{x,0} \Rightarrow \frac{d\hat{\psi}_{0,n_0}}{dz} = \frac{d\hat{\psi}^*_{0,n_0}}{dz} \tag{4–71}$$

and the tangential stress balance can be written as

$$\frac{\partial v_{x,0}}{\partial z} + \frac{\partial v_{z,0}}{\partial x} = \frac{\mu^*}{\mu}\left[\frac{\partial v^*_{x,0}}{\partial z} + \frac{\partial v^*_{z,0}}{\partial x}\right] \tag{4–72}$$

which gives

$$\frac{d^2\hat{\psi}_{0,n_0}}{dz^2} + k_0^2\hat{\psi}_{0,n_0} = \frac{\mu^*}{\mu}\left[\frac{d^2\hat{\psi}^*_{0,n_0}}{dz^2} + k_0^2\hat{\psi}^*_{0,n_0}\right] \tag{4–73}$$

By using the eight conditions given above, ψ_0 and ψ_0^* are determined in terms of Ca. Then, the expressions are substituted into the normal stress balance, which is given by

$$P_0 - 2\frac{\partial v_{z,0}}{\partial z} - P_0^* + 2\frac{\mu^*}{\mu}\frac{\partial v^*_{z,0}}{\partial z} = 0 \tag{4–74}$$

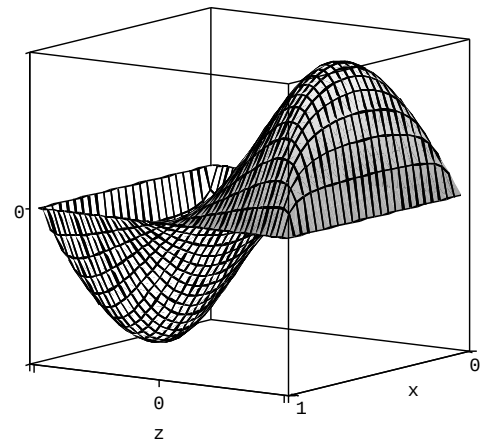

Figure 4-4. Base state stream function for closed flow Rayleigh-Taylor problem for Ca = 1, w/L = 1.

Replacing pressures with the stream functions, the new form of the normal stress balance is given as

$$\frac{d^3\hat{\psi}_{0,n_0}}{dz^3} - 3k_0^2\frac{d\hat{\psi}_{0,n_0}}{dz} - \frac{\mu^*}{\mu}\left[\frac{d^3\hat{\psi}^*_{0,n_0}}{dz^3} - 3k_0^2\frac{d\hat{\psi}^*_{0,n_0}}{dz}\right] = 0 \tag{4–75}$$

It turns out that the normal stress balance is satisfied if and only if the viscosities of both liquids, the compartment depths, and upper and lower wall speeds are the same, i.e., $\mu = \mu^*, L = L^*, a = 1$. With these conditions, the stream functions for both fluids are the same, i.e., $\psi_0 = \psi_0^*$. The plots of the stream functions and the velocity fields can be seen in Figures 4-4 and 4-5.

The stability of this base state is studied in the next section by introducing the perturbed equations and solving the resulting eigenvalue problem.

The perturbed state: The perturbed domain equations in terms of stream functions are

$$\nabla^4\psi_1 = 0 \quad \text{for} \quad 0 < x < w/L \quad \text{and} \quad 0 < z < 1 \tag{4–76}$$

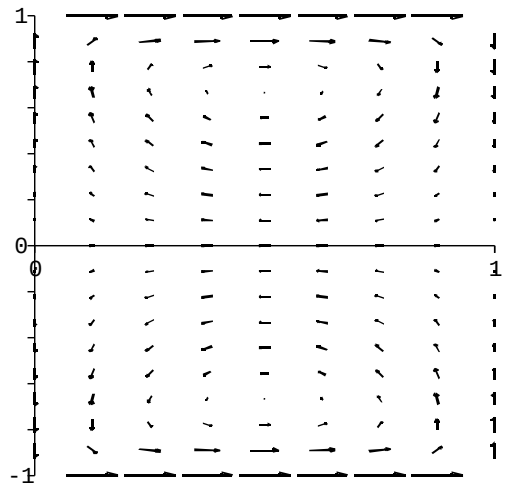

Figure 4-5. Base state velocity field for closed flow Rayleigh-Taylor problem for Ca = 1, w/L = 1.

for the upper phase. Similarly, for the lower phase

$$\nabla^4 \psi_1^* = 0 \;\text{ for }\; 0 < x < w/L \;\text{ and }\; -1 < z < 0 \tag{4–77}$$

are valid. They are solved by a procedure that was used for obtaining the solution for the base state and require the use of the perturbed boundary conditions. At the bottom wall, located at $z = -1$, the perturbed no-slip and the no-penetration conditions give rise to

$$\frac{d\hat{\psi}^*_{1,n_1}}{dz} = 0 \;\text{ and }\; \hat{\psi}^*_{1,n_1} = 0 \tag{4–78}$$

A similar equation is valid at the top wall. Note that, the index that was n_0 at the base state is now changed to n_1. These indices will play a big role in the course of solving the perturbed equations and so particular attention should be paid to them. At the interface, mass balance is satisfied and thus

$$\hat{\psi}_{1,n_1} = \hat{\psi}^*_{1,n_1} \tag{4–79}$$

and

$$\frac{\partial \psi_1}{\partial x} = -Z_1 \frac{\partial^2 \psi_0}{\partial x \partial z} - \frac{dZ_1}{dx}\frac{\partial \psi_0}{\partial z} + \sigma Z_1 \tag{4–80}$$

Observe that the x and z dependent parts of the variables in the above equation were not separated, because there is coupling between the modes and each variable needs to be written as a summation. Accordingly, Equation 4–80 becomes

$$\sum_{n_1} \frac{n_1 \pi}{w/L} \hat{\psi}_{1,n_1} \cos\left(\frac{n_1 \pi}{w/L} x\right) = -\sum_{m_1} \hat{Z}_{1,m_1} \cos\left(\frac{m_1 \pi}{w/L} x\right) \sum_{n_0} \frac{n_0 \pi}{w/L} \frac{d\hat{\psi}_{0,n_0}}{dz} \cos\left(\frac{n_0 \pi}{w/L} x\right)$$
$$- \sum_{m_1} -\frac{m_1 \pi}{w/L} \hat{Z}_{1,m_1} \sin\left(\frac{m_1 \pi}{w/L} x\right) \sum_{n_0} \frac{d\hat{\psi}_{0,n_0}}{dz} \sin\left(\frac{n_0 \pi}{w/L} x\right) + \sigma \sum_{m_1} \hat{Z}_{1,m_1} \cos\left(\frac{m_1 \pi}{w/L} x\right) \tag{4–81}$$

The no-slip condition at the interface at this order becomes

$$\frac{d\hat{\psi}_{1,n_1}}{dz} = \frac{d\hat{\psi}^*_{1,n_1}}{dz} \tag{4–82}$$

while the tangential stress balance is given by

$$\frac{d^2\hat{\psi}_{1,n_1}}{dz^2} = \frac{d^2\hat{\psi}^*_{1,n_1}}{dz^2} \tag{4–83}$$

The viscosities do not appear in the tangential stress balance, because a flat base state is satisfied only when the viscosities of both fluids are identical. By using Equation 4–78 and its counterpart for the top fluid, and Equations 4–79, 4–82, and 4–83, seven of the constants of the stream functions are determined in terms of A_1^*. Thus the stream functions can be written as

$$\hat{\psi}_{1,n_1}(z) = A_1^* \breve{\psi}_{1,n_1}(z) \quad \text{and} \quad \hat{\psi}^*_{1,n_1}(z) = A_1^* \breve{\psi}^*_{1,n_1}(z) \tag{4–84}$$

where $\breve{\psi}_{1,n_1}$ and $\breve{\psi}^*_{1,n_1}$ are known. The last coefficient A_1^* is determined by using Equation 4–81, which can then be written as

$$\sum_{n_1} \frac{n_1\pi}{w/L}\hat{\psi}_{1,n_1}\cos\left(\frac{n_1\pi}{w/L}x\right) = \sigma\sum_{m_1}\hat{Z}_{1,m_1}\cos\left(\frac{m_1\pi}{w/L}x\right)$$
$$-\frac{1}{2}\sum_{m_1}\sum_{n_0}\frac{n_0\pi}{w/L}\hat{Z}_{1,m_1}\frac{d\hat{\psi}_{0,n_0}}{dz}\left[\cos\left([m_1-n_0]\frac{\pi}{w/L}x\right)+\cos\left([m_1+n_0]\frac{\pi}{w/L}x\right)\right]$$
$$+\frac{1}{2}\sum_{m_1}\sum_{n_0}\frac{m_1\pi}{w/L}\hat{Z}_{1,m_1}\frac{d\hat{\psi}_{0,n_0}}{dz}\left[\cos\left([m_1-n_0]\frac{\pi}{w/L}x\right)-\cos\left([m_1+n_0]\frac{\pi}{w/L}x\right)\right] \tag{4–85}$$

To reduce Equation 4–85 into its moments, it is multiplied by $\cos\left(\frac{j\pi}{w/L}x\right)$ and integrated over x. After some manipulations, Equation 4–85 becomes

$$\frac{n_1\pi}{w/L}\hat{\psi}_{1,n_1} = \sigma\hat{Z}_{1,n_1} + \frac{1}{2}\frac{n_1\pi}{w/L}\sum_{n_0}\frac{d\hat{\psi}_{0,n_0}}{dz}\left[\hat{Z}_{1,(n_1+n_0)} - \hat{Z}_{1,(n_1-n_0)}\right] \tag{4–86}$$

In the above equation, $Z_{1,(-j)} = Z_{1,(j)}$ where j is a positive integer. Note that $j = 0$ is ruled out by the constant-volume requirement given in Equation 3–6. The last coefficient, A_1^*, is found by substituting Equation 4–84 into Equation 4–86, i.e.,

$$\frac{n_1\pi}{w/L}A_1^*\breve{\psi}_{1,n_1} = \sigma\hat{Z}_{1,n_1} + \frac{1}{2}\frac{n_1\pi}{w/L}\sum_{n_0}\frac{d\hat{\psi}_{0,n_0}}{dz}\left[\hat{Z}_{1,(n_1+n_0)} - \hat{Z}_{1,(n_1-n_0)}\right] \tag{4–87}$$

Observe that Equation 4–87 is evaluated at $z = 0$. To close the problem, the normal stress balance is used. It is written as

$$\frac{d^3\hat{\psi}_{1,n_1}}{dz^3} - 3k_1^2\frac{d\hat{\psi}_{1,n_1}}{dz} + \hat{Z}_{1,n_1}\left[-k_1Bo + k_1^3\right] - \left[\frac{d^3\hat{\psi}^*_{1,n_1}}{dz^3} - 3k_1^2\frac{d\hat{\psi}^*_{1,n_1}}{dz}\right] = 0 \tag{4–88}$$

When the stream functions $\hat{\psi}_{1,n_1}$ and $\hat{\psi}^*_{1,n_1}$ are substituted into Equation 4–88, an eigenvalue problem of the form $\mathcal{M}\hat{Z}_1 = \sigma\hat{Z}_1$ is obtained. Here, σ are the eigenvalues and $\mathcal{M}$ is a nondiagonal matrix that occurs as such because of the coupling between the modes. As in the open channel flow, our aim is to see the effect of the wall speed or the Capillary number on the RT instability. The input variables are the physical properties of the liquids, the width of the box, the depth

of the liquids, and the wall speed. In terms of dimensionless variables, they are Bo, w/L, and Ca. The output variables are the growth constant σ, or more precisely the real and the imaginary parts of σ and the eigenmodes.

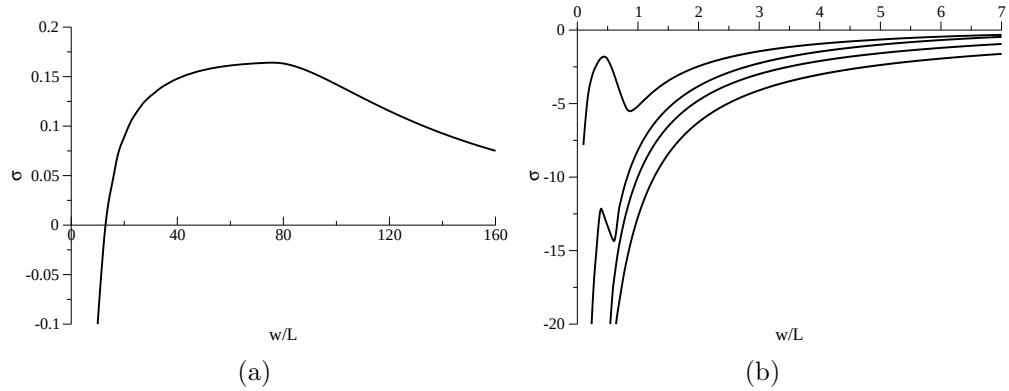

Figure 4-6. Dispersion curves for the closed flow Rayleigh-Taylor problem for Ca=10 and Bo=5. a) The ordinate is the leading eigenvalue, i.e., σ_{35}. b) The ordinate of the upper curve is the leading σ, and the ordinate of the subsequent curves are 30th, 25th, and $20^{th}\sigma$ respectively.

There are infinite eigenvalues because of the summation of infinite terms in Equation 4–87. The size of the matrix $\mathcal{M}$ depends on the number of terms taken in the series, which is determined by the convergence of the leading eigenvalue. In these calculations, 35 terms sufficed for all values of parameters. The eigenvalues are found using Maple 9^{TM}. In Figure 4-6(a), the real part of the leading σ, namely σ_{35}, is plotted against w/L. A variety of observations can be made from this dispersion curve but first the reason for the instability is given. The stabilizing mechanisms are due to the viscosities of the liquids and the surface tension. On the other hand, transverse gradients of pressure between crests and troughs, which depend on width, as well as gravity, which is width independent, destabilize the system. When the width is extremely small, approaching zero, the system is stable and the growth constant approaches negative infinity. This behavior is related to the stabilizing effect of the surface tension, which acts more strongly on small widths, in other words, on large curvature. When the width becomes larger, the

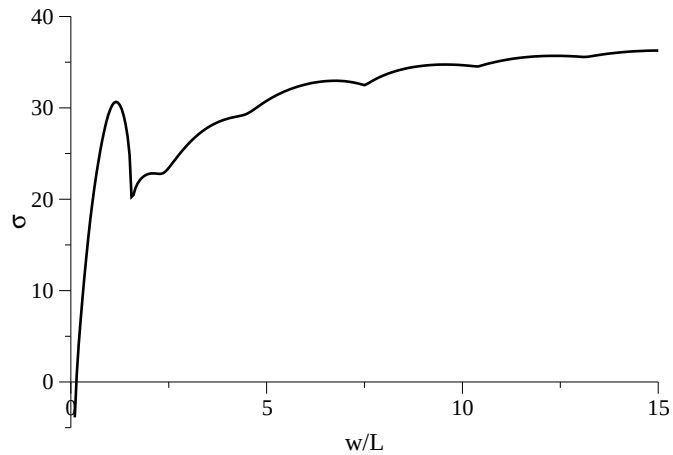

Figure 4-7. The dispersion curve for the closed flow Rayleigh-Taylor showing multiple maxima and minima for Ca=20 and Bo=500.

surface tension can no longer provide as much stabilization and, as a result, the curve rises to neutrality, where there is a balance between the opposing effects. For larger width the surface tension effects get weaker and consequently, the destabilizing forces become dominant and the growth curve crosses the neutral state and becomes positive. As the width increases even more, the curve continues rising but at some point it passes through a maximum and starts decreasing as can be seen in Figure 4-7. This calls for an explanation. This phenomenon, distinctive of the closed flow problem, is attributed to the interaction of the modes. As the width increases, higher modes must be accommodated. This has a dual effect; when a higher mode is introduced, the waves become choppier and surface tension acts to stabilize the higher mode, while destabilizing transverse pressure gradients also act more strongly. Further increase in the width causes an increase in the distance between crests and troughs and the stabilizing effect of surface tension becomes weaker as also does the destabilizing effect of transverse pressure gradients.

As the width increases, more and more modes now need to be accommodated. Consequently, the growth curve shows multiple maxima and minima as can be seen in Figure 4-7.

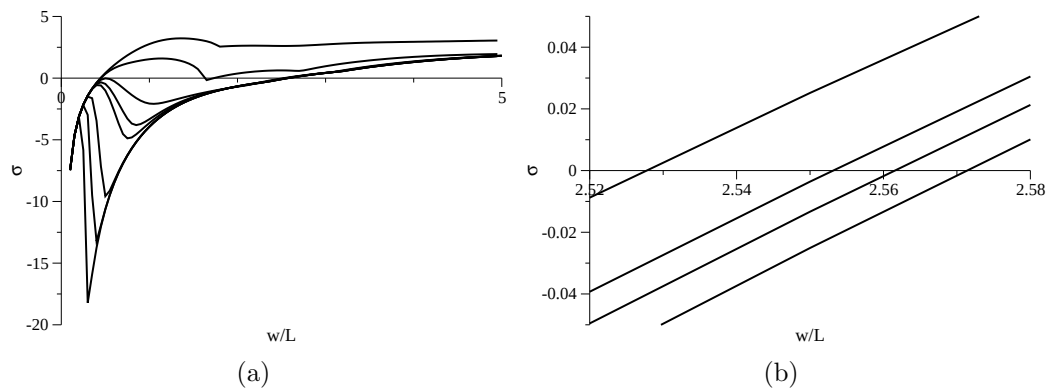

(a) (b)

Figure 4-8. The effect of the wall speed on the stability of shear-induced Rayleigh-Taylor for Bo=50. a) The graphs correspond to Ca=1 (the most upper curve), Ca=4, 10, 15, 20, 100, 500, and 5000. b) Close-up view near the critical point for Ca=10 (the most left), Ca=15, 20, and 100.

In summary, the inclusion of a higher mode as the width increases first makes the waves choppier; but a further increase in the width makes the waves in the new mode less choppy. Thus, stabilizing and destabilizing effects that are width dependent get reversed in strength. In Figure 4-6(b), the real part of the leading σ and some of the lower growth constants are plotted for small widths. The pattern of the other curves is similar to that of the leading one. However, more terms are needed in the summation in Equation 4–87 for the convergence of these curves in Figure 4-6(b).

Our aim is to see the effect of the wall speed on the RT instability. For that purpose, in Figure 4-8 the dispersion curves for the leading σ are plotted against w/L for several Capillary numbers at a fixed Bond number. Each curve shows a similar behavior to the curves presented in Figure 4-6. As the width increases from zero, the curves increase from negative infinity. They then exhibit several maxima and minima. For large Ca, the first maximum occurs when σ is negative, i.e., the system is stable. On the other hand, for small Ca, e.g. $Ca = 1$, the first maximum is observed when the system is unstable. So, when the curve starts decreasing, the system becomes less unstable, but it remains unstable. A very interesting feature is

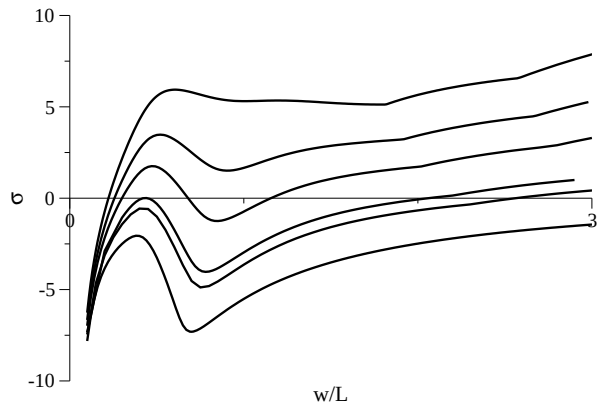

Figure 4-9. The effect of Bo on the stability of shear-induced Rayleigh-Taylor for Ca=20. The curves correspond to Bo=200 (The most upper curve), 150, 110, 65, 50, and 5.

observed for the intermediate Capillary numbers. The first maximum is seen close to the neutral point. Interestingly enough, the eigenvalue becomes negative one more time. For those curves, like the second curve from the top in Figure 4-8(a), it is possible to obtain a dispersion curve that has three critical points. In other words, there are two regions for the width where the system is stable. The size of this second stable window depends on Ca and Bo. This stability region builds a basis for a very interesting experiment. The effect of the wall speed on the critical point can be seen in Figure 4-8(b), which is a close-up view of Figure 4-8(a). The system becomes more stable as the walls are moved faster. In Figure 4-8, the dispersion curve is plotted at a fixed Bond number for different Capillary numbers while in Figure 4-9, the Capillary number is kept fixed and the curves are similar. The critical points are collected and the neutral curve is obtained in Figure 4-10.

The neutral curve depicted in Figure 4-10 is not a monotonically decreasing curve. It is clear that for some Bo numbers there exist three critical points. A neutral curve exhibiting three different critical points for a given wave number is seen in the pure Marangoni problem [42]. However, it should be noted that when gravity is added to the Marangoni problem, it does not exhibit the zero wave number instability seen in the pure Marangoni problem and consequently,

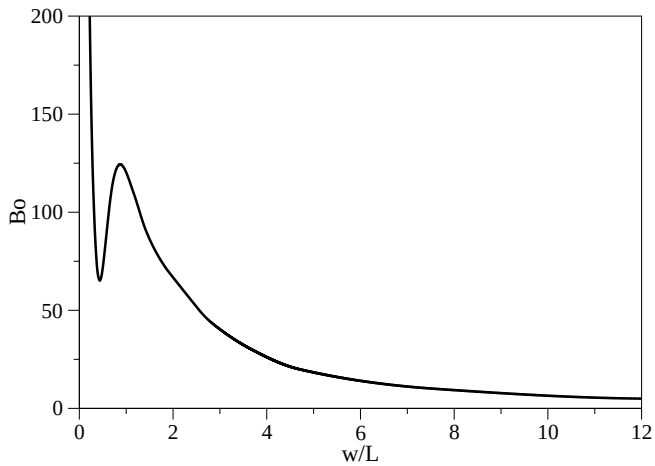

Figure 4-10: The neutral stability curve for the shear-induced flow where Ca=20.

does not have three critical points. The gravity is able to stabilize the small wave number disturbances. A dispersion curve, and therefore a neutral curve similar to those obtained in this study was observed by Agarwal et al. [43] in a solidification problem. Besides these examples, such a dispersion curve is not common in most interfacial instabilities. If one wants to compare the stability point of the shear-induced RT problem to that of the classical RT problem, it would be more practical to plot $Bo\frac{w^2}{L^2}$ versus w/L. If the depths are large enough, the classical RT stability limit, which is $Bo\frac{w^2}{L^2} = \pi^2$, is recovered because the effect of shear is lost.

By using linear stability analysis, it was concluded that moving the walls and creating a returning flow enhances the classical RT stability. The next question to answer is what happens when the onset of instability is passed. In other words, the type of bifurcation is of interest. The classical RT instability shows a backward pitchfork (subcritical) bifurcation when the control parameter is the width. Once the instability sets in, it goes to complete breakup. What would one see in an experiment when the interface becomes unstable for the closed flow RT configuration? To answer this question, a weakly nonlinear analysis is performed in the next section.

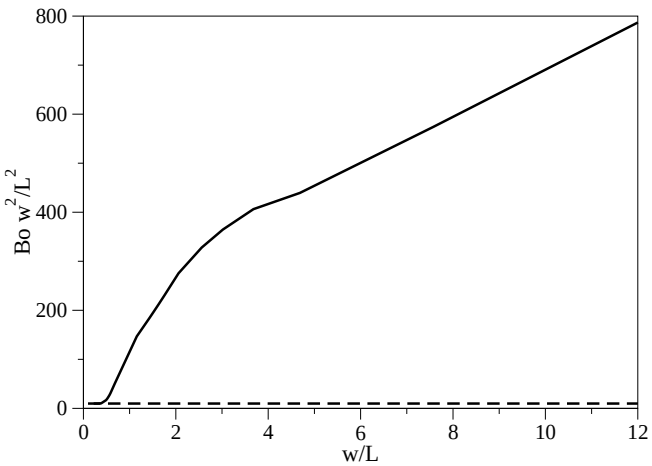

Figure 4-11. The neutral stability curve for the shear-induced flow where Ca=20. The dashed line represents the critical value for the classical Rayleigh-Taylor problem, which is π^2. Observe that the ordinate is independent of L.

Weakly nonlinear analysis: In the weakly nonlinear analysis, the aim of this study is to seek steady solutions, as one goes beyond a critical point by increasing or decreasing a control parameter, λ, from its critical value, λ_c, by a small amount. For that purpose, let each variable, "u", be expanded as follows

$$u = u_0 + [\lambda - \lambda_{\mathrm{c}}]^{\alpha} \left[u_1 + z_1 \frac{\partial u_0}{\partial z} \right]$$

$$+ \frac{1}{2}[\lambda - \lambda_{\mathrm{c}}]^{2\alpha} \left[u_2 + 2z_1 \frac{\partial u_1}{\partial z} + z_1^2 \frac{\partial^2 u_0}{\partial z^2} + z_2 \frac{\partial u_0}{\partial z} \right] + \frac{1}{6}[\lambda - \lambda_{\mathrm{c}}]^{3\alpha}$$

$$\left[u_3 + 3z_1 \frac{\partial u_2}{\partial z} + 3z_2 \frac{\partial u_1}{\partial z} + 3z_1 z_2 \frac{\partial^2 u_0}{\partial z^2} + 3z_1^2 \frac{\partial^2 u_1}{\partial z^2} + z_1^3 \frac{\partial^3 u_0}{\partial z^3} + z_3 \frac{\partial u_0}{\partial z} \right] + \cdots \qquad (4\text{–}89)$$

In the above equation, z_1, z_2, and z_3 are the mappings from the current state to the reference or the base state [10]. The idea is to substitute the expansion into the governing nonlinear equations and determine α from dominant balance as well as the variable u_n at various orders [44]. In this shear-induced RT problem, the control parameter is chosen to be the scaled wall speed or the Capillary number, Ca. Instead of determining α, an alternative approach is to guess it, and the

correctness of this guess is checked throughout the calculation [44]. In anticipation of a pitchfork bifurcation, α is set to 1/2 for this calculation. Thus, the expansion can be written more conveniently as

$$u = u_0 + \epsilon \left[u_1 + z_1 \frac{\partial u_0}{\partial z} \right] + \frac{1}{2}\epsilon^2 \left[u_2 + 2z_1 \frac{\partial u_1}{\partial z} + z_1^2 \frac{\partial^2 u_0}{\partial z^2} + z_2 \frac{\partial u_0}{\partial z} \right]$$

$$+ \frac{1}{6}\epsilon^3 \left[u_3 + 3z_1 \frac{\partial u_2}{\partial z} + 3z_2 \frac{\partial u_1}{\partial z} + 3z_1 z_2 \frac{\partial^2 u_0}{\partial z^2} + 3z_1^2 \frac{\partial^2 u_1}{\partial z^2} + z_1^3 \frac{\partial^3 u_0}{\partial z^3} + z_3 \frac{\partial u_0}{\partial z} \right] + \cdots \quad (4\text{–}90)$$

where ϵ is such that $Ca = Ca_c + \frac{1}{2}\epsilon^2$. When the expansions are substituted into the nonlinear equations, to the lowest order in ϵ, the base state problem is recovered; its solution is known. The first order problem in ϵ is a homogenous problem and it is identical to the eigenvalue problem provided σ is set to zero. It is important to note that in this weakly nonlinear analysis we assume that both the real and the imaginary parts of the largest growth constant is zero. Thus, if the neutral point is purely imaginary, this method would not applicable. In this problem, some, but not all, of the leading growth constants have imaginary parts. However, in what follows we shall focus only on steady bifurcation points, as we are interested in steady solutions.

The solution procedure is as follows. In the first order problem, the state variables are solved in terms of Z_1, which represents the surface deflection at first order. This results in a homogenous problem being expressed as $\mathcal{M}\hat{Z}_1 = 0$. Again, $\mathcal{M}$ is a real non-symmetric matrix operator. At this order, the value of the critical parameter, Ca_c, and the eigenvectors, up to an arbitrary constant, A, are found. Then, the second order problem is obtained and is expected to be of the form $\mathcal{M}\hat{Z}_2 = f\left(\hat{Z}_1^2\right) + c$ where the constant c appears from the boundary condition at the moving wall. A solvability condition has to be applied to this equation whence A can be found. If it turns out that the solvability condition is automatically satisfied, one needs to advance to the next order. At this order, the solvability

condition provides A^2 whose sign determines whether the pitchfork is forward or backward. In the next section the second order equations are presented.

Second order problem: The perturbed domain equations at second order are solved subject to the boundary conditions in a way similar to the previous orders. At the bottom wall, the no-slip and the no-penetration conditions are given by

$$\frac{d\hat{\psi}^*_{2,n_2}}{dz} = -1 \quad \text{and} \quad \hat{\psi}^*_{2,n_2} = 0 \tag{4–91}$$

A similar equation is valid at the top wall. At the interface, the second-order mass balance equation satisfies

$$\hat{\psi}_{2,n_2} = \hat{\psi}^*_{2,n_2} \tag{4–92}$$

and

$$\frac{\partial \psi_2}{\partial x} = -Z_2 \frac{\partial^2 \psi_0}{\partial x \partial z} - \frac{dZ_2}{dx}\frac{\partial \psi_0}{\partial z} \tag{4–93}$$

Recall that at the base state ψ_0 was found to be equal to ψ^*_0. This leads to several cancellations; for reasons of brevity the intermediate steps are omitted and simplified versions of the equations are presented. As in previous order equations, each variable is represented as a summation. As a result, (4–93) becomes

$$\hat{\psi}_{2,n_2} = \frac{1}{2}\sum_{n_0} \frac{d\hat{\psi}_{0,n_0}}{dz}\left[\hat{Z}_{2,(n_2+n_0)} - \hat{Z}_{2,(n_2-n_0)}\right] \tag{4–94}$$

The no-slip condition is given by

$$\frac{d\hat{\psi}_{2,n_2}}{dz} = \frac{d\hat{\psi}^*_{2,n_2}}{dz} \tag{4–95}$$

The tangential stress balance assumes the form

$$\frac{\partial^2 \psi_2}{\partial z^2} + 2Z_1 \frac{\partial^3 \psi_1}{\partial z^3} = \frac{\partial^2 \psi^*_2}{\partial z^2} + 2Z_1 \frac{\partial^3 \psi^*_1}{\partial z^3} \tag{4–96}$$

and the series expansion of the tangential stress balance yields

$$\frac{d^2\hat{\psi}_{2,n_2}}{dz^2} + \sum_{m_1} \hat{Z}_{1,m_1} \left[\frac{d^3\hat{\psi}_{1,(n_2-m_1)}}{dz^3} + \frac{d^3\hat{\psi}_{1,(n_2+m_1)}}{dz^3} \right]$$
$$= \frac{d^2\hat{\psi}^*_{2,n_2}}{dz^2} + \sum_{m_1} \hat{Z}_{1,m_1} \left[\frac{d^3\hat{\psi}^*_{1,(n_2-m_1)}}{dz^3} + \frac{d^3\hat{\psi}^*_{1,(n_2+m_1)}}{dz^3} \right] \tag{4–97}$$

By using the above conditions, $\hat{\psi}_{2,n_2}$ and $\hat{\psi}^*_{2,n_2}$ are determined. To close the problem, the normal stress balance is introduced in stream function form as

$$\frac{d^3\hat{\psi}_{2,n_2}}{dz^3} - \frac{d^3\hat{\psi}^*_{2,n_2}}{dz^3} + \hat{Z}_{2,n_2}\left(-k_2 Bo + k_2^3\right) = 0 \tag{4–98}$$

It turns out that after much algebraic manipulations, the normal stress balance results in $\mathcal{M}\hat{Z}_2 = 0$. This means solvability is automatically satisfied; hence $\hat{Z}_2 = B\hat{Z}_1$ holds. Therefore, the third order problem needs to be introduced with the hope of finding A^2 and the nature of the pitchfork bifurcation. Before introducing the third order equations, the meaning of the sign of A^2 needs to be given. Recall that an increase in Ca implies more stability; consequently, if A^2 turns out to be positive at the next order, a curve of A versus $1/Ca$ represents a backward (subcritical) pitchfork. However, if A^2 were determined to be negative, this would be unallowable. Then, Ca must be decreased from Ca_c by an amount $1/2\epsilon^2$ leading to a positive A^2, hence, a forward (supercritical) pitchfork in an A vs. $1/Ca$ graph.

Third order problem: The boundary conditions at the bottom wall are

$$\frac{d\hat{\psi}^*_{3,n_3}}{dz} = 0 \quad \text{and} \quad \hat{\psi}^*_{3,n_3} = 0 \tag{4–99}$$

At the interface, the mass balance equation satisfies

$$\frac{\partial \psi_3}{\partial x} - 3\left[\frac{dZ_1}{dx}\right]^2 \frac{\partial \psi_1}{\partial x} + 3Z_1 \frac{\partial^2 \psi_2}{\partial x \partial z} + 3Z_2 \frac{\partial^2 \psi_1}{\partial x \partial z} + 3Z_1^2 \frac{\partial^3 \psi_1}{\partial x \partial z^2} + 3\frac{dZ_2}{dx}\frac{\partial \psi_1}{\partial z}$$

$$+ 3\frac{dZ_1}{dx}\frac{\partial \psi_2}{\partial z} + 6Z_1 \frac{dZ_1}{dx}\frac{\partial^2 \psi_1}{\partial z^2} = \text{(similar expression for * phase)} \tag{4–100}$$

Note that in the above equation, the terms coming from the base state are not shown because they canceled each other as $\psi_0 = \psi_0^*$ holds. In addition, there are some more cancellations that take place when the interface conditions of the previous orders are introduced, e.g., the second term in Equation 4–100 cancels with the corresponding term of the * phase by using Equation 4–79. Hereafter, as the equations are very long, only the very simplified form of the interface conditions will be provided without separating the x and z dependent parts. However, it should be noted that as in the previous orders, each term has to be represented as a summation because of the coupling of the modes. The no-mass transfer condition at the interface gives rise to

$$\psi_3 = \psi_3^* \tag{4–101}$$

and

$$\frac{\partial \psi_3}{\partial x} + Z_3 \frac{\partial^2 \psi_0}{\partial x \partial z} + \frac{dZ_3}{dx}\frac{\partial \psi_0}{\partial z} - 3\left[\frac{dZ_1}{dx}\right]^2 \frac{\partial \psi_1}{\partial x} - 3Z_1\left[\frac{dZ_1}{dx}\right]^2 \frac{\partial^2 \psi_0}{\partial x \partial z} + 3Z_1 \frac{\partial^2 \psi_2}{\partial x \partial z} + 3Z_1^2 \frac{\partial^3 \psi_1}{\partial x \partial z^2}$$

$$+ Z_1^3 \frac{\partial^4 \psi_0}{\partial x \partial z^3} - 3\left[\frac{dZ_1}{dx}\right]^3 \frac{\partial \psi_0}{\partial z} + 3\frac{dZ_1}{dx}\frac{\partial \psi_2}{\partial z} + 6Z_1 \frac{dZ_1}{dx}\frac{\partial^2 \psi_1}{\partial z^2} + 3Z_1^2 \frac{dZ_1}{dx}\frac{\partial^3 \psi_0}{\partial z^3} = 0 \tag{4–102}$$

The no-slip condition at the interface is

$$\frac{\partial \psi_3}{\partial z} + 3Z_1 \frac{\partial^2 \psi_2}{\partial z^2} + 3Z_1^2 \frac{\partial^3 \psi_1}{\partial z^3} = \frac{\partial \psi_3^*}{\partial z} + 3Z_1 \frac{\partial^2 \psi_2^*}{\partial z^2} + 3Z_1^2 \frac{\partial^3 \psi_1^*}{\partial z^3} \tag{4–103}$$

The tangential stress balance assumes the form

$$\frac{\partial^2\psi_3}{\partial z^2}+3Z_1\frac{\partial^3\psi_2}{\partial z^3}+3Z_2\frac{\partial^3\psi_1}{\partial z^3}=\frac{\partial^2\psi_3^*}{\partial z^2}+3Z_1\frac{\partial^3\psi_2^*}{\partial z^3}+3Z_2\frac{\partial^3\psi_1^*}{\partial z^3} \tag{4–104}$$

Finally, the normal stress balance is given by

$$\frac{\partial^3\psi_3}{\partial z^3}+3\frac{\partial^3\psi_3}{\partial z\partial x^2}+9\frac{dZ_1}{dx}\frac{\partial^3\psi_2}{\partial z^2\partial x}+6\frac{d^2Z_1}{dx^2}\frac{\partial^2\psi_2}{\partial z^2}+3Z_1^2\frac{\partial^5\psi_1}{\partial z^5}+3Z_1\frac{\partial^4\psi_2}{\partial z^4}$$

$$+12Z_1\frac{d^2Z_1}{dx^2}\frac{\partial^3\psi_1}{\partial z^3}+18Z_1\frac{dZ_1}{dx}\frac{\partial^4\psi_1}{\partial z^3\partial x}+9Z_1\frac{\partial^4\psi_2}{\partial z^2\partial x^2}+12\left[\frac{dZ_1}{dx}\right]^2\frac{\partial^3\psi_1}{\partial z^3}$$

$$+9Z_1^5\frac{\partial^5\psi_1}{\partial z^3\partial x^2}-\text{(similar expression for *)}$$

$$+\frac{dZ_3}{dx}Bo+\frac{d^3Z_3}{dx^3}-18\left[\frac{d^2Z_1}{dx^2}\right]^2\frac{dZ_1}{dx}-9\frac{d^3Z_1}{dx^3}\left[\frac{dZ_1}{dx}\right]^2=0 \tag{4–105}$$

The way to proceed from this point is very similar to the procedure applied at the previous orders. First, the x-dependent part of the variables is separated and the equations are written as a summation. Then, $\hat{\psi}_3$ and $\hat{\psi}_3^*$ are solved in terms of $\hat{Z}_3$ and the inhomogeneities. Finally, these expressions are substituted into the normal stress balance and a problem of the form $\mathcal{M}\hat{Z}_3 = a_1\hat{Z}_1^3 + a_2\hat{Z}_1\hat{Z}_2 + a_3\hat{Z}_1$ is obtained. At the second order, $\mathcal{M}\hat{Z}_2$ was equal to zero. In fact, at the third order, the constant a_2 turns out to be zero for much the same reason. Now, the second order correction to the interface deflection can be written as $\hat{Z}_2 = B\hat{Z}_1$ and the constant B is not known but is not needed either. The unknown constant A or more precisely, A^2 determines the type of pitchfork bifurcation.

Using the equation from the first order, i.e., $\mathcal{M}\hat{Z}_1 = 0$, the solvability condition can be applied as follows

$$\left\langle \hat{Z}_1^\dagger, \mathcal{M}\hat{Z}_3 \right\rangle = \left\langle \hat{Z}_1^\dagger, a_1\hat{Z}_1^3 + a_3\hat{Z}_1 \right\rangle \tag{4–106}$$

$$\left\langle \mathcal{M}^\dagger\hat{Z}_1^\dagger, \hat{Z}_3 \right\rangle = \left\langle 0, \hat{Z}_3 \right\rangle \tag{4–107}$$

where the superscript † denotes the adjoint and $\langle . , . \rangle$ stands for the inner product. All the variables are solved in terms of the surface deflection. The last equation to be used is the normal stress balance. In that equation, all parameters are substituted and therefore $\mathcal{M}$ is a real matrix and its adjoint is therefore its transpose. Then, by using Equation 4–106 and Equation 4–107, one can get

$$\left\langle \hat{Z}_1^\dagger, a_1\hat{Z}_1^3 + a_3\hat{Z}_1 \right\rangle = 0 \tag{4–108}$$

It is known that $\hat{Z}_1 = A\hat{\hat{Z}}_1$ where $\hat{\hat{Z}}_1$ was found at the first order. Equation 4–108 then can be expressed in terms of A as follows

$$\alpha A^4 + \beta A^2 = 0 \tag{4–109}$$

where α and β are constants which are determined at this third order. Let's elaborate on how to obtain Equation 4–109. First, Ca and Bo are fixed. The corresponding critical w/L is found from the first order calculation, which resulted in Figure 4-10. When Bo is smaller than some value, which is approximately 70 for the choice of parameters in Figure 4-10, there is only one critical point and this critical point has an imaginary part i.e., it is a Hopf bifurcation. As noted before, this weakly nonlinear analysis traces only steady solutions and is therefore not applicable to such critical points. However there is another region of Bo number where there is only one critical point: Bo larger than approximately 110. In that region, the critical point does not exhibit any imaginary part and this analysis is applicable to such points, A^2 is always positive and the pitchfork is backward

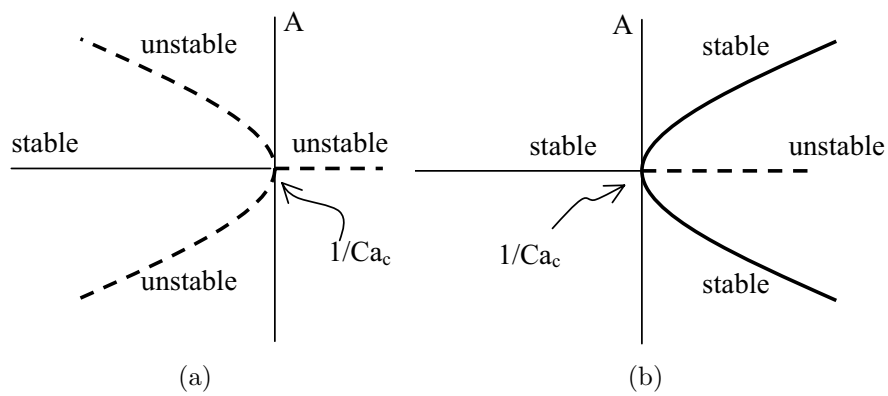

Figure 4-12. Bifurcation diagrams. a) Backward (Subcritical) pitchfork. b) Forward (Supercritical) pitchfork.

as depicted in Figure 4-12(a). When there are three critical points (For example, $Ca = 20$, $Bo = 70$), the A^2 corresponding to the largest w/L is again positive and the bifurcation is backward. If the bifurcation is backward, once the instability sets in, it goes to complete breakup. In contrast with the largest critical w/L, the smallest two critical points give rise to a negative A^2. Then Ca must be decreased from Ca_c in order to get a positive A^2 and, for these cases, the nature of the bifurcation is forward as depicted in Figure 4-12(b). Some more observations can be made from the calculation. The inhomogeneities coming from the no-slip condition, Equation 4–103, and the tangential stress balance, Equation 4–104, have no effect on the constants α and β.

Once A is known, the variation of the actual magnitude of the disturbances with respect to a parameter change can be calculated when Ca is advanced by a small percentage beyond the critical point. For example, one can compare the amplitude of the deflections of the first and second critical points for a fixed Ca and Bo and something interesting but explicable turns up. It is found that A^2 corresponding to the small w/L is one order of magnitude larger than A^2 of the larger w/L. This can be explained by looking at Figure 4-10 at the region where three critical points occur. Focusing on the first two points, we observe that the

first critical point is where instability starts, while the second one is where stability starts. This means that, any advancement into a nonlinear region from the first critical point must produce a larger roughness, i.e., A^2, compared to the second critical point provided the nature of the pitchforks are the same; and indeed they are.

4.5 Summary

The critical point of the RT instability is found using Rayleigh's work principle. The analysis requires determining the change in the total energy of the system, which is composed of the gravitational and surface potential energies.

The theoretical study of the RT instability with elliptical interface turned out to be more stable than its companion RT instability with circular interface. This result is in agreement with our physical intuition based on the increased possibilities of the dissipation of the disturbances switching from a circle to an ellipse.

It is known in the RT problem that there is a decrease in stability when the liquid is sheared with a constant stress. This decrease in the stability limit is attributed to the symmetry breaking effect of the shear. In this study, we show that the fluid mechanics of the light fluid is important and it changes the characteristics of the problem. Under specific circumstances a flat interface is permissible under shear. For the open channel flow, to get a flat interface in the base state, the wall speed has to be adjusted according to the ratio of the liquid heights and the viscosity ratios. If both ratios are unity then any wall speed is allowed. On the other hand, for the closed flow problem, bias in the liquid heights, the wall speeds or the viscosities is not permitted. If there is any difference between the speeds of the upper and the lower walls or between the viscosity and depth of the upper liquid and those of the lower liquid, then the system is less stable than the classical RT problem.

In the open channel flow, the critical point remains unchanged compared to the classical RT instability, but the critical point exhibits oscillations and the frequency of the oscillations depends linearly on the wall speed. The perturbations are carried in the horizontal direction by the moving wall resulting in an oscillatory critical point. On the other hand, in a closed geometry, moving the wall stabilizes the classical RT instability. The results show when, how and why shear can delay the RT instability limit. Physical and mathematical reasons for the enhanced stability are presented. In the closed flow problem, the lateral walls impede the traveling waves and create a returning flow. The stability point increases with increasing wall speed as expected. It is also concluded that the system is more stable for shallow liquid depths. For large liquid depths, the shear has a long distance to travel; consequently, it loses its effect. The classical RT instability is recovered when the liquid depths are very large or the wall speed approaches zero. The most interesting feature of this problem is the presence of the second window of stability. For a given range of Ca and Bo, there exist three critical points, i.e., the system is stable for small widths, it is unstable at some width, but, it becomes stable one more time for a larger width. We present a weakly nonlinear analysis via a dominant balance method to study the nature of the bifurcation from the steady bifurcation points. It is concluded that the problem shows a backward or forward pitchfork bifurcation depending on the critical point.

Clearly, it would not be easy to conduct an experiment with the specifications given in this section. The problem does not accommodate any bias in liquid depths nor in viscosities of the liquids. Any small difference is going to cause a non-flat interface and lead to an instability, which will occur even before the classical RT instability. An ideal experiment might be carried out with porous sidewalls and with two viscous liquids. However, from a mathematical point of view, the problem shows interesting characteristics that have physical interpretations. For stress-free

lateral walls, it is possible to obtain an analytical solution though, it is not possible to uncouple the modes. In fact, the work in this section has shown the effect of mode interaction on delaying the instability.

The main results of this chapter are that an elliptical cross section offers more stability than a companion circular cross section subject to axisymmetric disturbances and that shear driven flow in the RT problem can stabilize the classical instability and lead to a larger critical width. These results motivate us to run some experiments but experiments on the RT problem are not simple to construct and so we consider building liquid bridge experiments with a view of changing the geometry and introducing flow and seeing their effect on the instability.

CHAPTER 5
THE STABILITY OF LIQUID BRIDGES

This chapter deals with the stability of liquid bridges. The organization of this chapter is the same as the previous chapter. We will start with Rayleigh's work principle to investigate the critical point of a cylindrical liquid bridge in zero gravity. Then, we will move on to the effect of geometry on the stability point. This section contains two problems. The first one is the effect of off-centering a liquid bridge with respect to its encapsulant. In the second part, elliptical liquid bridges are studied. In fact, this section proves our intuition based on the dissipation of the disturbances. Finally, the effect of shear is presented, which helps us understand the effect of returning flow in the floating zone crystal growth technique.

5.1 The Breakup Point of a Liquid Bridge by Rayleigh's Work Principle

We know from Rayleigh's calculations that a liquid thread breaks up when the wavelength of the disturbance exceeds its circumference. Let's begin by giving a simple calculation to determine the critical length of a bridge. This calculation is based on Rayleigh's work principle as adapted from Johns and Narayanan [10]. We will follow a procedure similar to the previous chapter.

According to the Rayleigh work principle the stability of a system to a given disturbance is related to the change of energy of the system. In the liquid bridge problem the surface energy is the surface area multiplied by its surface tension. The critical or neutral point is attained when there is no change in the surface area for a given disturbance. Consider a volume of liquid with a given perturbation on it, as seen in Figure 5–1. The volume of the liquid under the crest is more than

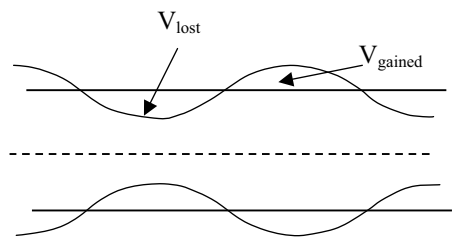

Figure 5-1: Volume of liquid with a given periodic perturbation.

the volume under the through (Appendix C); but the volume of the liquid needs to be constant upon the given perturbation. Therefore, there is an imaginary volume of liquid of smaller diameter whose volume upon perturbation is the same as the actual volume. As a result, the surface area of the liquid is increased with the given perturbation but it is also decreased because of the lower equivalent diameter. At the critical point, there is a balance between the two effects and the surface area remains constant.

To set these thoughts to a calculation consider the liquid having a radius R_0. A one-dimensional disturbance changes the shape of the liquid to

$$r = R + \epsilon \cos(kz) \tag{5–1}$$

where R is the equivalent radius, ϵ represents the amplitude of the disturbance, assumed to be small, and k is the wave number given by $n\pi/L$ with L being the length of the bridge. Using the above shape, the surface area is given by

$$A = \int_0^L 2\pi r \frac{ds}{dz} dz \tag{5–2}$$

where ds is the arc length, given by $ds = \left[1 + \left[\frac{dr}{dz}\right]^2\right]^{1/2} dz \approx \left[1 + \frac{1}{2}\left[\frac{dr}{dz}\right]^2\right] dz$. So, the area per unit length turns out to be

$$\frac{A}{L} = 2\pi R + \frac{1}{2}\pi R \epsilon^2 k^2 \tag{5–3}$$

Here R, the equivalent radius is found from the constant-volume requirement as follows

$$V = \pi R_0^2 \lambda = \int_0^L \pi r^2 dz \tag{5–4}$$

which implies R to be equal to $R_0 - \frac{1}{4}\frac{\epsilon^2}{R_0}$. Substituting this radius into the area expression, the change in area is obtained as

$$\frac{1}{2}\pi \frac{\epsilon^2}{R_0 L^2}\left[(2\pi R_0)^2 - L^2\right] \tag{5–5}$$

The critical point is attained when the length of the bridge is equal to the circumference of the bridge. There are two obvious questions that arise from this calculation: what is the role of the disturbance type on the stability point and what is the role of the liquid properties on the stability point? A particular disturbance type, a cosine function is chosen for this calculation as every disturbance can be broken into its Fourier components and the same calculation can be repeated. In fact, the same calculation is performed by Johns and Narayanan [10] on page 10 for any function $f(z)$ without decomposing into its Fourier components. Equation 5–5 tells us that the critical point does not depend on the properties of the liquid. This can be understood from the pressure argument introduced in Chapter 2. At the critical point, there is no flow. The viscosity and the surface tension play a role in determining the growth or decay rates of the disturbances. Such a curve can be reproduced via a perturbation calculation and this is given next.

5.2 A Simple Derivation To Obtain the Dispersion Curve for a Liquid Bridge via a Perturbation Calculation

A simple perturbation calculation is used to determine the critical length and the dispersion curve of a liquid bridge. To make matters simple, the liquid bridge is assumed to be composed of only one inviscid liquid, and the gravity is neglected. This calculation will show the critical length as a function of its radius; the same calculation methodology will also be applied in more complicated situations, such

as the case when a liquid encapsulates another liquid. The Euler and continuity equations are:

$$\rho\frac{\partial\vec{v}}{\partial t} + \rho\vec{v}\cdot\nabla\vec{v} = -\nabla P \tag{5–6}$$

and

$$\nabla\cdot\vec{v} = 0 \tag{5–7}$$

These domain equations will be solved subject to the force balance and no mass flow at the interface i.e.,

$$P = -\gamma 2H \tag{5–8}$$

and

$$\vec{n}\cdot\vec{v} = \vec{n}\cdot\vec{u} \tag{5–9}$$

Here 2H is the mean curvature, $\vec{n}$ the outward normal to the jet surface and u the surface normal speed (Appendix B). To investigate the stability of the base state, impose a perturbation upon it. Let ϵ indicate the size of the perturbation and expand and P in terms of ϵ, viz.

$$\vec{v} = \vec{v}_0 + \epsilon\left[\vec{v}_1 + r_1\frac{\partial\vec{v}_0}{\partial r}\right] + \cdots \quad \text{and} \quad P = P_0 + \epsilon\left[P_1 + r_1\frac{\partial P_0}{\partial r}\right] + \cdots \tag{5–10}$$

'r1' is the mapping from the current configuration of a perturbed jet to the reference configuration of the cylindrical bridge. We presented the expansion of a domain variable along the mapping Appendix A. More information can be found in Johns and Narayanan [10]. The radius of the bridge R in the current configuration may also be expanded in terms of the reference configuration as

$$R\left(\theta, z, t, \epsilon\right) = R_0 + \epsilon R_1 + \cdots \tag{5–11}$$

Collecting terms to zeroth order in ϵ we get

$$\rho\frac{\partial\vec{v}_0}{\partial t} + \rho\vec{v}_0\cdot\nabla\vec{v}_0 = -\nabla P_0 \tag{5–12}$$

and

$$\nabla \cdot \vec{v}_0 = 0 \tag{5–13}$$

There is a simple solution to the problem. It is $\vec{v} = \vec{0}$ and $P = \gamma/R_0$ where R_0 is the radius of the bridge.

The perturbed equations at first order become

$$\rho \frac{\partial \vec{v}_1}{\partial t} = -\nabla P_1 \tag{5–14}$$

and

$$\nabla \cdot \vec{v}_1 = 0 \tag{5–15}$$

Likewise the interface conditions at first order are

$$P_1 = -\gamma \left[\frac{R_1}{R_0^2} + \frac{1}{R_0^2} \frac{\partial^2 R_1}{\partial \theta^2} + \frac{\partial^2 R_1}{\partial z^2} \right] \tag{5–16}$$

and

$$\vec{i}_{r0} \cdot \vec{v}_1 = v_{r1} = \frac{\partial R_1}{\partial t} \tag{5–17}$$

The stability of the base state will be determined by solving the perturbation equations. To turn the problem into an eigenvalue problem, substitute

$$P_1 = \hat{P}_1 (r) \, e^{\sigma t} e^{im\theta} \cos (kz) \tag{5–18}$$

and

$$R_1 = \hat{R}_1 e^{\sigma t} e^{im\theta} \cos (kz) \tag{5–19}$$

into the first order equations. In the first order equations s, m, and k stand for the inverse time constant, the azimuthal wave number and axial wave number respectively. Eliminate velocity to get

$$\nabla^2 P_1 = \frac{1}{r} \frac{d}{dr} \left(r \frac{d\hat{P}_1}{dr} \right) - \left[\frac{m^2}{r^2} + k^2 \right] \hat{P}_1 = 0 \tag{5–20}$$

The corresponding boundary conditions for the perturbed pressure are

$$\frac{d\hat{P}_1}{dr} = -\sigma^2 \rho \hat{R}_1 \tag{5–21}$$

and

$$\hat{P}_1 = -\gamma \left[\frac{1}{R_0^2} - \frac{m^2}{R_0^2} - k^2 \right] \hat{R}_1 \tag{5–22}$$

The eigenvalues are the values of s at which this problem has a solution other than the trivial solution. Let us first look at the neutral point, i.e., $\sigma^2 = 0$. The solution to Equation 5–20 is of the form

$$\hat{P}_1 = A I_m (kr) \tag{5–23}$$

where A must satisfy

$$\frac{d\hat{P}_1}{dr} (r = R_0) = 0 \tag{5–24}$$

From Equation 5–24, A vanishes. Using this in the only remaining equation, i.e., Equation 5–22 gives

$$0 = -\frac{\gamma}{R_0^2} \left[1 - m^2 - R_0^2 k^2 \right] \hat{R}_1 \tag{5–25}$$

Now, for $\hat{R}_1$ to be other than zero $[1 - m^2 - R_0^2 k^2]$ has to be equal to zero which gives us the critical wave number of the bridge from $k_{critical}^2 R_0^2 = 1$, hence the critical length of the bridge is its circumference.

To obtain the dispersion curve, one needs to substitute Equation 5–22 into Equation 5–21 to get

$$\sigma^2 \rho \hat{P}_1 = \frac{\gamma}{R_0^2} \left[1 - m^2 - R_0^2 k^2 \right] \frac{d\hat{P}_1}{dr} \tag{5–26}$$

Substituting the expression for $\hat{P}_1$ from Equation 5–23 into the above equation

$$\sigma^2 = \frac{\gamma}{\rho R_0^3} \left[1 - m^2 - R_0^2 k^2 \right] \frac{k R_0 I_m' (k R_0)}{I_m (k R_0)} \tag{5–27}$$

is obtained. Here, $I'_m(x) = \frac{d}{dx} I_m(x)$. The most dangerous mode is when m is zero. Then, the equation for the dispersion curve is

$$\sigma^2 = \frac{\gamma}{\rho R_0^3}\left[1 - k^2 R_0^2\right] \frac{kR_0 I'_0(kR_0)}{I_0(kR_0)} \tag{5–28}$$

5.3 The Effect of Geometry on the Stability of Liquid Bridges

In this section we will be concerned with two issues related to geometry. The first has to do with the possible off-centering of a bridge. Recall that to obtain a cylindrical bridge we have to encapsulate it by another liquid of the same density. This leads to the possibility that the bridge might be off centered and in turn this raises questions on the stability of the bridge. The second problem has to do with the end plates of the bridge. We ask whether the stability of the bridge can be enhanced by making the end plates noncircular, specifically elliptic. The motivation for this stems from our observations on the elliptic RT problem where azimuthal pressure variations allowed us to obtain greater stability.

5.3.1 The Stability of an Encapsulated Cylindrical Liquid Bridge Subject to Off-Centering

The liquid bridge is taken to be inviscid simply so as to simplify the calculations without much loss of essential physics. The perturbation theory explained in the earlier chapters is used to study the stability of such a bridge subject to inertial disturbances. At the end of the analysis we will learn that while the off-centered nature does not change the neutral point it does affect the rate of growth and decay of the disturbances causing the unstable regions to become less unstable and stable regions to become less stable. Limiting conditions are considered in order to provide a better understanding of the physics of off-centering.

To begin the analysis of the problem, we draw the attention of the reader to Figure 5-2, which depicts an off-centered bridge in an outer encapsulant. We are particularly interested in what happens to the damping and growth rates of the

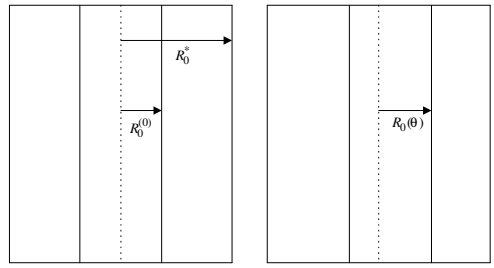

Figure 5-2: Centered and off-centered liquid bridges.

perturbations if the bridge is not centered. The stability is studied by imposing small disturbances upon a quiescent cylindrical base state. Before this, we turn to the governing nonlinear equations, which are given next.

The equation of motion and the continuity equation for an inviscid, constant density fluid are given by

$$\rho\frac{\partial\vec{v}}{\partial t} + \rho\vec{v}\cdot\nabla\vec{v} = -\nabla P \tag{5–29}$$

$$\nabla\cdot\vec{v} = 0 \tag{5–30}$$

Equations 5–29 and 5–30 are valid in a region $0 \leq r \leq R(\theta, z)$, where $R(\theta, z)$ is the position of the disturbed interface of the bridge. Here ρ is the density, and $\vec{v}$ and P are the velocity and pressure fields. Similar equations for the outer fluid, represented by '*', can be written in the region $R(\theta, z) \leq r \leq R_0^{(0)^*}$. The solution to the base state problem is $\vec{v}_0 = \vec{0} = \vec{v}_0^*$ and $P_0 - P_0^* = -\gamma 2H_0 = \dfrac{\gamma}{R_0}$. Note that this base state may be the centered or off-centered state. In the next sub section we will present the higher order equations, which will then give us the dynamic behavior of the disturbances.

5.3.1.1 Perturbed equations: ϵ^1 problem

To first order upon perturbation, the equations of motion and continuity are

$$\rho\frac{\partial\vec{v}_1}{\partial t} = -\nabla P_1 \quad \text{and} \quad \nabla\cdot\vec{v}_1 = 0 \tag{5–31}$$

in the region $0 \leq r \leq R_0(\theta)$. Combining the two equations we get

$$\nabla^2 P_1 = 0 \qquad 0 \leq r \leq R_0(\theta) \tag{5–32}$$

with similar equation for the '*' fluid. The domain equations are second order differential equations in both spatial directions. Consequently, eight constants of integration must be determined along with R_1, which is the surface mapping evaluated at the base state. To find these unknown constants and R_1, we write the boundary conditions in perturbed form. At the interface, there is no-mass flow and the normal component of the stress balance holds. Consequently

$$\vec{n}_0 \cdot (\vec{v}_1 - \vec{u}_1) = 0 = \vec{n}_0 \cdot (\vec{v}_1^* - \vec{u}_1) \tag{5–33}$$

and

$$P_1 - P_1^* = -\gamma 2 H_1 \tag{5–34}$$

The walls are impermeable to flow; as a result the normal component of the velocity is zero, or in terms of pressure we can write

$$\vec{n}_0 \cdot \nabla P_1 = 0 \tag{5–35}$$

A similar equation is valid for the '*' fluid. Free end conditions are chosen for the contact of the bridge with the solid upper and lower walls, i.e.,

$$\frac{dR_1}{dz} = 0 \;\; \text{at } z = 0,\; L_0 \tag{5–36}$$

The perturbed velocities, $\vec{v}_1$ and $\vec{v}_1^*$ can be eliminated from the boundary equations by using Equation 5–31 and its counterpart for the '*' fluid. We separate the time dependence from the spatial dependence by assuming that the pressure, velocity and R_1 can be expressed as $K = \hat{K} e^{\sigma t}$ where K is the variable in question.

Equation 5–33 then becomes

$$\frac{1}{\rho}\vec{n}_0 \cdot \nabla \hat{P}_1 = \frac{-\sigma^2 \hat{R}_1}{\left[1 + \frac{R_\theta^2}{R_0^2}\right]^{1/2}} = \frac{1}{\rho^*}\vec{n}_0 \cdot \nabla \hat{P}_1^* \tag{5–37}$$

Hereafter, the symbol, '^', will be removed from all variables. The problem given by Equations 5–32 - 5–37 is an eigenvalue problem but the geometry is inconvenient because R_0 is a function of the azimuthal angle 'θ'. Therefore we use perturbation theory and write the equations at the reference state i.e., the state when the shift distance 'δ' is equal to zero and where R_0 is equal to $R_0^{(0)}$ and is independent of 'θ'. All variables, at every order are expanded in a perturbation series in δ, including the square of the inverse time constant σ. Therefore σ^2 is

$$\sigma^2 = \sigma^{2^{(0)}} + \delta\sigma^{2^{(1)}} + \frac{1}{2}\delta^2\sigma^{2^{(2)}} + \cdots \tag{5–38}$$

Our goal is to determine the variation of σ^2 at each order to find the effect of the shift, δ, upon the stability of the bridge. The calculation of $\sigma^{2^{(0)}}$ is well-known and can be found in Chandrasekhar's treatise [17]. Its value depends upon the nature of the disturbances given to the reference bridge and can become positive only for axisymmetric disturbances. Hence, the effect of δ on the stability of the bridge subjected to only axisymmetric disturbances in its reference on-centered state is considered. To calculate the first non-vanishing correction to σ^2, we need to determine the mapping from the displaced bridge configuration to the centered configuration, and this is done next.

5.3.1.2 Mapping from the centered to the off-centered liquid bridge

In determining the mapping, we note that we have two different types of perturbations: the physical disturbance represented by ϵ, and the displacement of the liquid bridge represented by δ. Hence, we have an expansion in two variables.

To get this expansion, we observe that the surface of the disturbed liquid bridge is denoted by

$$r = R(\theta,\ z,\ t,\ \epsilon,\ \delta) \tag{5–39}$$

Therefore R can be expanded as

$$R = \overbrace{\left(R_0^{(0)} + \delta R_0^{(1)} + \frac{1}{2}\delta^2 R_0^{(2)} + \ \cdots\right)}^{R_0(\theta,\delta)} + \epsilon \overbrace{\left(R_1^{(0)} + \delta R_1^{(1)} + \frac{1}{2}\delta^2 R_1^{(2)} + \ \cdots\right)}^{R_1(\theta,z,t,\delta)} + \ \cdots \tag{5–40}$$

where $R_0^{(0)}$ is the radius of the centered bridge and $R_0^{(1)} = \dfrac{dR_0}{d\delta}(\delta = 0)$. Figure 5-3 helps us to relate $R_0^{(1)}$ and $R_0^{(2)}$ to $R_0^{(0)}$. By using the basic principles of trigonometry, we can conclude that

$$R_0^2 + \delta^2 - 2\delta R_0 \cos(\theta) = {R_0^{(0)}}^2 \tag{5–41}$$

Substituting the expansion of R_0 from Equation 5–40 into Equation 5–41, we get

$$R_0^{(1)} = \cos(\theta) \ \text{ and } \ R_0^{(2)} = -\frac{\sin^2(\theta)}{R_0^{(0)}}$$

The mapping from centered to off-centered configuration having been found, the effect of the displacement on the stability of the liquid bridge can be determined from the sign of $\sigma^{2^{(1)}}$, which is given in the next section.

5.3.1.3 Determining $\sigma^{2^{(1)}}$

The perturbation expansions involve terms of mixed orders. The subscripts represent the ϵ disturbance while the superscripts in parentheses represent the δ displacement. The domain equation of order $\epsilon^1\delta^0$ is

$$\nabla^2 P_1^{(0)} = 0 \quad 0 \le r \le R_0^{(0)} \tag{5–42}$$

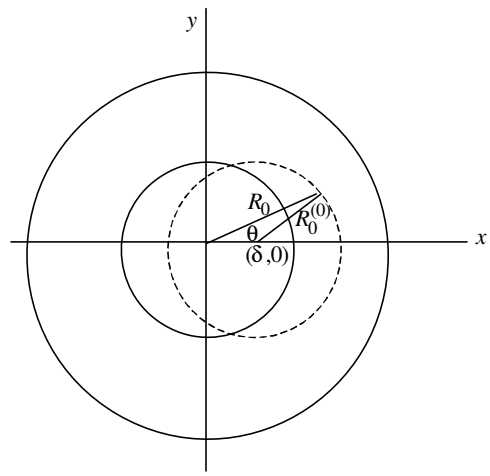

Figure 5-3: The cross-section of an off-centered liquid bridge.

The outer liquid's domain equation can be written similarly. The mass conservation and the normal stress balance at the interface require

$$\frac{-1}{\rho}(\vec{n}_0^{(0)} \cdot \nabla P_1^{(0)}) = \sigma^{2^{(0)}} R_1^{(0)} = \frac{-1}{\rho^*}(\vec{n}_0^{(0)} \cdot \nabla P_1^{(0)^*}) \tag{5–43}$$

and

$$P_1^{(0)} - P_1^{(0)^*} = -\gamma 2 H_1^{(0)} \tag{5–44}$$

In a similar way, the domain equation of order $\epsilon^1\delta^1$ is

$$\nabla^2 P_1^{(1)} = 0 \quad 0 \leq r \leq R_0^{(0)} \tag{5–45}$$

The conservation of mass equation at the interface becomes

$$\frac{-1}{\rho}\left[\vec{n}_0^{(1)} \cdot \nabla P_1^{(0)} + \vec{n}_0^{(0)} \cdot \left[\nabla P_1^{(1)} + R_0^{(1)} \frac{\partial[\nabla P_1^{(0)}]}{\partial r}\right]\right] = \sigma^{2^{(1)}} R_1^{(0)} + \sigma^{2^{(0)}} R_1^{(1)} \tag{5–46}$$

where $R_0^{(1)}$ is the mapping from the current configuration of an off-centered bridge to the reference configuration of the centered bridge and was shown to be $\cos(\theta)$. A similar set of equations can be written for the outer liquid. The normal stress

balance at the interface at this order is

$$\left[P_1^{(1)} + R_0^{(1)}\frac{\partial P_1^{(0)}}{\partial r}\right] - \left[P_1^{(1)^*} + R_0^{(1)}\frac{\partial P_1^{(0)^*}}{\partial r}\right] = -\gamma 2 H_1^{(1)} \tag{5–47}$$

We use an energy method to get the sign of $\sigma^{2^{(1)}}$. By multiplying Equation 5–45 by $P_1^{(0)}/\rho$, Equation 5–42 by $P_1^{(1)}/\rho$, integrating over the volume $\hat{V}$, taking their difference and adding to this a similar term arising from '*' fluid, we obtain

$$\int_{\hat{V}} \left[\frac{P_1^{(0)}}{\rho}\nabla^2 P_1^{(1)} - \frac{P_1^{(1)}}{\rho}\nabla^2 P_1^{(0)}\right] d\hat{V}$$

$$+ \int_{\hat{V}^*} \left[\frac{P_1^{(0)^*}}{\rho^*}\nabla^2 P_1^{(1)^*} - \frac{P_1^{(1)^*}}{\rho^*}\nabla^2 P_1^{(0)^*}\right] d\hat{V}^* = 0 \tag{5–48}$$

The volume integrals can be transformed into surface integrals by using Green's formula. The integral over the 'rz' surface vanishes because of symmetry, i.e. because $P_1^{(0)}$ is the same at 'θ' equal to zero and 2π. The integral over the '$r\theta$' surface vanishes because of the impermeable wall conditions. Equation 5–48 therefore becomes

$$R_0^{(0)}\int_0^{L_0}\int_0^{2\pi}\left[P_1^{(0)}\frac{\partial P_1^{(1)}}{\rho\partial r} - P_1^{(1)}\frac{\partial P_1^{(0)}}{\rho\partial r}\right](r = R_0^{(0)})\, d\theta dz$$

$$-R_0^{(0)}\int_0^{L_0}\int_0^{2\pi}\left[P_1^{(0)^*}\frac{\partial P_1^{(1)^*}}{\rho^*\partial r} - P_1^{(1)^*}\frac{\partial P_1^{(0)^*}}{\rho^*\partial r}\right](r = R_0^{(0)})\, d\theta dz = 0 \tag{5–49}$$

Applying no-mass transfer equations at the interface i.e., Equations 5–43 and 5–46, Equation 5–49 becomes

$$\int_0^{L_0}\int_0^{2\pi}\Bigg[-P_1^{(0)}\left[\sigma^{2^{(0)}}R_1^{(1)} + \sigma^{2^{(1)}}R_1^{(0)} - \frac{R_0^{(1)}}{\rho}\frac{\partial^2 P_1^{(0)}}{\partial r^2}\right]$$

$$+P_1^{(0)^*}\left[\sigma^{2^{(0)}}R_1^{(1)} + \sigma^{2^{(1)}}R_1^{(0)} - \frac{R_0^{(1)}}{\rho^*}\frac{\partial^2 P_1^{(0)^*}}{\partial r^2}\right]$$

$$+ [P_1^{(1)} - P_1^{(1)^*}][\sigma^{2^{(0)}}R_1^{(0)}]\Bigg](r = R_0^{(0)})d\theta dz = 0 \tag{5–50}$$

Equation 5–50 is simplified by noting the fact that $\epsilon^1\delta^0$ terms are 'θ' independent and that $R_0^{(1)}$ is equal to $\cos(\theta)$. Consequently, the integral of $P_1^{(0)}\dfrac{R_0^{(1)}}{\rho}\dfrac{\partial^2 P_1^{(0)}}{\partial r^2}$ and the corresponding term for the outer liquid over 'θ' is zero. Substituting the normal stress balances at each order, i.e. Equations 5–44 and 5–47, Equation 5–50 becomes

$$\int_0^{L_0}\int_0^{2\pi}\left[\gamma 2H_1^{(0)}(\sigma^{2^{(0)}}R_1^{(1)}+\sigma^{2^{(1)}}R_1^{(0)})-\gamma 2H_1^{(1)}(\sigma^{2^{(0)}}R_1^{(0)})\right](r=R_0^{(0)})\ d\theta dz=0 \tag{5–51}$$

To get the sign of $\sigma^{2^{(1)}}$ from Equation 5–51, we need to determine the form of $2H_1^{(1)}$ and therefore $R_1^{(1)}$. But, the form of $R_1^{(1)}$ can be guessed from Equation 5–46, which has two types of inhomogeneities: $R_0^{(1)}\dfrac{\partial^2 P_1^{(0)}}{\partial r^2}$ and $\sigma^{2^{(1)}}R_1^{(0)}$. Therefore, $R_1^{(1)}$ can be written as

$$R_1^{(1)}=A(z)\sigma^{2^{(1)}}+B(z)\cos(\theta)+C$$

where the constant C is zero because of the constant-volume requirement. Substituting the form of $R_1^{(1)}$ into Equation 5–51, we obtain

$$\int_0^{L_0}\left[\gamma 2\pi\sigma^{2^{(0)}}\sigma^{2^{(1)}}\left\{A(z)\left[\frac{R_1^{(0)}}{R_0^{(0)^2}}+\frac{d^2R_1^{(0)}}{dz^2}\right]-R_1^{(0)}\left[\frac{A(z)}{R_0^{(0)^2}}+\frac{d^2A(z)}{dz^2}\right]\right\}\right.$$
$$\left.+\gamma 2\pi\sigma^{2^{(1)}}R_1^{(0)}\left[\frac{R_1^{(0)}}{R_0^{(0)^2}}+\frac{d^2R_1^{(0)}}{dz^2}\right]\right]dz=0 \tag{5–52}$$

where we have used

$$2H_1^{(0)}=\frac{R_1^{(0)}}{R_0^{(0)^2}}+\frac{d^2R_1^{(0)}}{dz^2}\quad\text{and}\quad 2H_1^{(1)}=\frac{R_1^{(1)}}{R_0^{(0)^2}}+\frac{1}{R_0^{(0)^2}}\frac{\partial^2R_1^{(1)}}{\partial\theta^2}+\frac{\partial^2R_1^{(1)}}{\partial z^2}$$

To determine the sign of $\sigma^{2^{(1)}}$ from Equation 5–52, the self-adjointness of the d^2/dz^2 operator and the corresponding boundary conditions on $R_1^{(0)}(z)$ and $A(z)$ are used, rendering the term in Equation 5–52 in '{}' to zero. Also, the Rayleigh

inequality [45], states that

$$\left[\frac{R_1^{(0)}}{R_0^{(0)^2}} + \frac{d^2 R_1^{(0)}}{dz^2}\right] \geq \lambda^2 R_1^{(0)}$$

where λ^2 is the lowest positive eigenvalue of the differential operator d^2/dz^2 and λ^2 is strictly positive. When we substitute this into Equation 5–52, we conclude that $\sigma^{2^{(1)}}$ is zero. Therefore, to find the effect of off-centering we need to move on to the next order in δ and get $\sigma^{2^{(2)}}$.

5.3.1.4 Determining $\sigma^{2^{(2)}}$

The domain equation of the $\epsilon^1\delta^2$ order is

$$\nabla^2 P_1^{(2)} = 0 \tag{5–53}$$

The conservation of mass at the interface requires

$$\frac{-1}{\rho}\left[\vec{n}_0^{(2)} \cdot \nabla P_1^{(0)} + 2\vec{n}_0^{(1)} \cdot \left[\nabla P_1^{(1)} + R_0^{(1)} \frac{\partial(\nabla P_1^{(0)})}{\partial r}\right]\right.$$

$$\left. + \vec{n}_0^{(0)} \cdot \left[\nabla P_1^{(2)} + 2R_0^{(1)} \frac{\partial(\nabla P_1^{(1)})}{\partial r} + R_0^{(1)^2} \frac{\partial^2(\nabla P_1^{(0)})}{\partial r^2} + R_0^{(2)} \frac{\partial(\nabla P_1^{(0)})}{\partial r}\right]\right]$$

$$= \sigma^{2^{(2)}} R_1^{(0)} + 2\sigma^{2^{(1)}} R_1^{(1)} + \sigma^{2^{(0)}} R_1^{(2)} - \frac{\sigma^{2^{(0)}} R_1^{(0)} R_\theta^{(1)^2}}{R_0^{(0)^2}} \tag{5–54}$$

where

$$\vec{n}_0^{(2)} \cdot \nabla P_1^{(0)} = -\frac{\sin^2(\theta)}{R_0^{(0)^2}} \frac{\partial P_1^{(0)}}{\partial r}$$

A similar mass balance equation for the outer fluid can be written. The normal stress balance satisfies

$$\left[P_1^{(2)} + 2R_0^{(1)} \frac{\partial P_1^{(1)}}{\partial r} + R_0^{(1)^2} \frac{\partial^2 P_1^{(0)}}{\partial r^2} + R_0^{(2)} \frac{\partial P_1^{(0)}}{\partial r}\right]$$

$$-\left[P_1^{(2)^*} + 2R_0^{(1)} \frac{\partial P_1^{(1)^*}}{\partial r} + R_0^{(1)^2} \frac{\partial^2 P_1^{(0)^*}}{\partial r^2} + R_0^{(2)} \frac{\partial P_1^{(0)^*}}{\partial r}\right] = -\gamma 2 H_1^{(2)} \tag{5–55}$$

where the mean curvature is given by

$$2H_1^{(2)} = \frac{R_1^{(2)}}{R_0^{(0)^2}} + \frac{1}{R_0^{(0)^2}}\frac{\partial^2 R_1^{(2)}}{\partial\theta^2} + \frac{\partial^2 R_1^{(2)}}{\partial z^2} + R.T. \tag{5–56}$$

while R.T is given by

$$R.T. = R_1^{(0)}[1-3\cos^2(\theta)] - \sin^2(\theta)R_0^{(0)^2}\frac{\partial^2 R_1^{(1)}}{\partial z^2} + 2\sin(\theta)R_0^{(0)}\frac{\partial R_1^{(1)}}{\partial\theta} - 4\cos(\theta)R_0^{(0)}\frac{\partial^2 R_1^{(1)}}{\partial\theta^2}$$

We proceed with an approach analogous to the previous section to predict the sign of $\sigma^{2^{(2)}}$ and we obtain the counterpart of Equation 5–48. We then use Green's formula and introduce the no-mass transfer at the interface for the $\epsilon^1\delta^2$ and the $\epsilon^1\delta^0$ problems, viz. Equations 5–54 and 5–43 to obtain the analog of Equation 5–50, which is

$$\begin{aligned}\int_0^{L_0}\int_0^{2\pi}\Bigg[&- P_1^{(0)}\Bigg[\sigma^{2^{(0)}}R_1^{(2)} + \sigma^{2^{(2)}}R_1^{(0)} - \frac{\sigma^{2^{(0)}}R_1^{(0)}\sin^2(\theta)}{R_0^{(0)^2}} \\ &+ \frac{2\cos(\theta)}{\rho}\frac{\partial^2 P_1^{(1)}}{\partial r^2} + \frac{\cos^2(\theta)}{\rho}\frac{\partial^3 P_1^{(0)}}{\partial r^3} - \frac{\sin^2(\theta)}{\rho R_0^{(0)}}\frac{\partial^2 P_1^{(0)}}{\partial r^2} \\ &+ \frac{2\sin(\theta)}{\rho R_0^{(0)}}\frac{\partial P_1^{(1)}}{\partial\theta} - \frac{\sin^2(\theta)}{\rho R_0^{(0)^2}}\frac{\partial P_1^{(0)}}{\partial r}\Bigg] + P_1^{(0)^*}(\text{similar expression for } * \text{ liquid}) \\ &+ (P_1^{(2)} - P_1^{(2)^*})(\sigma^{2^{(0)}}R_1^{(0)})\Bigg]\, d\theta dz = 0\end{aligned} \tag{5–57}$$

In order to simplify Equation 5–57 in a manner similar to the previous section, we use the normal stress balance equations, i.e. Equations 5–44 and 5–55, the form of $R_1^{(2)}$, which is guessed from the no-mass transfer equation, i.e. Equation 5–54 and the self-adjointness of the d^2/dz^2 operator. We also use Equation 5–43, which gives

$$-\frac{\sin^2(\theta)}{\rho R_0^{(0)^2}}\frac{\partial P_1^{(0)}}{\partial r} = \frac{\sigma^{2^{(0)}}R_1^{(0)}\sin^2(\theta)}{R_0^{(0)^2}}$$

Then, Equation 5–57 becomes

$$\int_0^{L_0}\int_0^{2\pi}\Bigg[-P_1^{(0)}\Bigg[\sigma^{2^{(2)}}R_1^{(0)}+\frac{2\cos(\theta)}{\rho}\frac{\partial^2 P_1^{(1)}}{\partial r^2}+\frac{\cos^2(\theta)}{\rho}\frac{\partial^3 P_1^{(0)}}{\partial r^3}$$

$$-\frac{\sin^2(\theta)}{\rho R_0^{(0)}}\frac{\partial^2 P_1^{(0)}}{\partial r^2}+\frac{2\sin(\theta)}{\rho R_0^{(0)}}\frac{\partial P_1^{(1)}}{\partial\theta}\Bigg]+P_1^{(0)^*}\Bigg[\text{similar expression for } * \text{ liquid}\Bigg]$$

$$+\Bigg[2\cos(\theta)\Bigg[\frac{\partial P_1^{(1)^*}}{\partial r}-\frac{\partial P_1^{(1)}}{\partial r}\Bigg]+\cos^2(\theta)\Bigg[\frac{\partial^2 P_1^{(0)^*}}{\partial r^2}-\frac{\partial^2 P_1^{(0)}}{\partial r^2}\Bigg]$$

$$-\frac{\sin^2(\theta)}{R_0^{(0)}}\Bigg[\frac{\partial P_1^{(0)^*}}{\partial r}-\frac{\partial P_1^{(0)}}{\partial r}\Bigg]\Bigg][\sigma^{2^{(0)}}R_1^{(0)}]-\sigma^{2^{(0)}}R_1^{(0)}\gamma(R.T)\Bigg]\,d\theta dz=0 \qquad (5\text{–}58)$$

In principle, $\sigma^{2^{(2)}}$ can be found from the above equation. However, some more work is needed as terms such as $R_1^{(0)}$, $P_1^{(0)}$ and $P_1^{(1)}$ appear. $R_1^{(0)}$ can be expressed as $B\cos(kz)$ for free end conditions, but the solution for the pressure $P_1^{(i)}$ is obtained from the domain equation $\nabla^2\ P_1^i\ =\ 0$ and upon letting $P_1^i=\hat{P}_1^i(r)\cos(kz)\cos(m\theta)$ the domain equation becomes

$$\frac{1}{r}\frac{d}{dr}\left(r\frac{d\hat{P}_1^i}{dr}\right)-\left(\frac{m^2}{r^2}+k^2\right)\hat{P}_1^i=0 \qquad (5\text{–}59)$$

where i and m are each zero for the $\epsilon^1\delta^0$ order and equal to one for the $\epsilon^1\delta^1$ order.

Using Equation 5–59, we evaluate the integrals in Equation 5–58 and obtain

$$0=-\hat{P}_1^{(0)}\frac{\pi^2}{\rho k}\Bigg[\sigma^{2^{(2)}}\rho\hat{R}_1^{(0)}+\frac{\partial^2\hat{P}_1^{(1)}}{\partial r^2}+\frac{\partial^3\hat{P}_1^{(0)}}{2\partial r^3}-\frac{1}{2R_0^{(0)}}\frac{\partial^2\hat{P}_1^{(0)}}{\partial r^2}-\frac{1}{R_0^{(0)}}\hat{P}_1^{(1)}\Bigg]$$

$$+\hat{P}_1^{(0)^*}\frac{\pi^2}{\rho^* k}\Bigg[\text{similar expression for } * \text{ liquid}\Bigg]$$

$$+\sigma^{2^{(0)}}R_0^{(0)}\frac{\pi^2}{2k}\Bigg[2\Bigg[\frac{\partial\hat{P}_1^{(1)^*}}{\partial r}-\frac{\partial\hat{P}_1^{(1)}}{\partial r}\Bigg]+\Bigg[\frac{\partial^2\hat{P}_1^{(0)^*}}{\partial r^2}-\frac{\partial^2\hat{P}_1^{(0)}}{\partial r^2}\Bigg]-\frac{1}{R_0^{(0)}}\Bigg[\frac{\partial\hat{P}_1^{(0)^*}}{\partial r}-\frac{\partial\hat{P}_1^{(0)}}{\partial r}\Bigg]\Bigg]$$

$$-\frac{\sigma^{2^{(0)}}\hat{R}_1^{(0)}\gamma}{R_0^{(0)^4}}\frac{\pi^2}{2k}\Bigg[-\hat{R}_1^{(0)}+k^2R_0^{(0)^2}\hat{R}_1^{(0)}+2R_0^{(0)}\hat{R}_1^{(1)}\Bigg] \qquad (5\text{–}60)$$

Note that $\hat{P}_1^{(0)}$ and $\hat{P}_1^{(1)}$ in Equation 5–60 are functions of only r and all of the terms are evaluated at the reference interface, i.e. at $r=R_0^{(0)}$.

To find the sign of $\sigma^{2^{(2)}}$ from Equation 5–60, we need to solve for the perturbed pressures. Their forms are found from Equation 5–59 as

$$P_1^{(i)} = \left[A_{km}^{(i)} I_m(kr) + C_{km}^{(i)} K_m(kr) \right] \cos(kz) \cos(m\theta)$$

and

$$P_1^{(i)^*} = \left[A_{km}^{(i)^*} I_m(kr) + C_{km}^{(i)^*} K_m(kr) \right] \cos(kz) \cos(m\theta)$$

where $C_{km}^{(i)}$ is zero because the pressure is bounded everywhere.

To obtain the constants $A,\ B,\ A^*$ and C^*, we substitute the form of the pressures into the boundary equations at each order. To order $\epsilon^1\delta^0$, from the no-mass transfer, viz. Equation 5–43, the normal stress balance, viz. Equation 5–44 and the impermeable walls, we get

$$A_{k0} I_0'(kR_0^{(0)}) = -\rho\sigma^{2^{(0)}} B_k \tag{5–61}$$

$$A_{k0}^* I_0'(kR_0^{(0)}) + C_{k0}^* K_0'(kR_0^{(0)}) = -\rho^*\sigma^{2^{(0)}} B_k \tag{5–62}$$

$$A_{k0} I_0(kR_0^{(0)}) - A_{k0}^* I_0(kR_0^{(0)}) - C_{k0}^* K_0(kR_0^{(0)}) = \frac{-\gamma B_k}{R_0^{(0)^2}} \left[1 - k^2 R_0^{(0)^2} \right] \tag{5–63}$$

and

$$A_{k0}^* I_0'(kR_0^{(0)^*}) + C_{k0}^* K_0'(kR_0^{(0)^*}) = 0 \tag{5–64}$$

When $\sigma^{2^{(0)}}$ is zero, we see from Equations 5–61, 5–62 and 5–64 that A_{k0}, A_{k0}^* and C_{k0}^* are all zero. From Equation 5–63, we recover the critical point, which is $k^2 R_0^{(0)^2} = 1$. When $\sigma^{2^{(0)}}$ is not zero, four equations must be solved simultaneously such that all of the constants not vanish at the same time.

Likewise, $\hat{P}_1^{(1)}$ and $\hat{P}_1^{(1)^*}$ are solved by introducing the boundary conditions at the $\epsilon^1\delta^1$ order. The solution of the perturbed pressures, $\hat{P}_1^{(i)}$ and $\hat{P}_1^{(i)^*}$ are substituted into Equation 5–60 to evaluate $\sigma^{2^{(2)}}$. The reader can see that an analytical expression for $\sigma^{2^{(2)}}$ is obtained. This expression, however, is extremely

lengthy so we move on to a graphical depiction of $\sigma^{2^{(2)}}$ and a discussion of the physics of the off-centering.

5.3.1.5 Results from the analysis and discussion

An immediate conclusion of the above derivations is that $\sigma^{2^{(1)}}$ is zero. This comes as no surprise because the deviation of the cylindrical bridge from the center is symmetric. In other words, it does not matter whether the deviation is of an amount equal to $+\delta$ or $-\delta$. In fact all odd order corrections to eigenvalues will therefore be equal to zero. Several figures are presented where the effect of off centering is shown and the physics of off centering is discussed. The ordinates and abscissas are given in terms of scaled quantities where the scale factors are obvious from the labels. Figure 5-4 shows the effect of off-centering on the growth rate constant σ. The neutral point did not change, which is not surprising because at the neutral point the pressure perturbations are indeed zero and since the system is neutrally at rest, it cannot differentiate between centered and off-centered configurations.

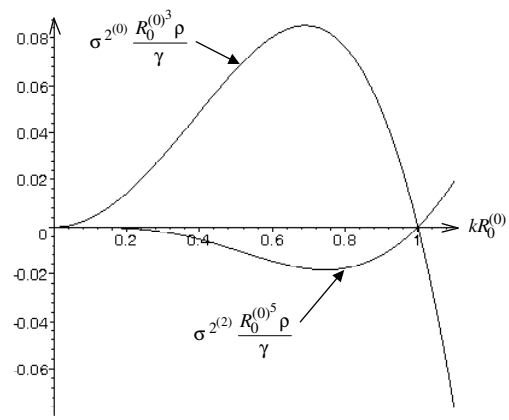

Figure 5-4. $\sigma^{2^{(0)}}$ and $\sigma^{2^{(2)}}$ (multiplied by their scale factors) versus the wavenumber for $\rho^*/\rho = 1$ and $R_0^{(0)^*}/R_0^{(0)} = 2$.

If 'k' is smaller than the critical wavenumber, k_c, the bridge is unstable to infinitesimal disturbances. As can be seen from Figure 5-4, once the bridge is

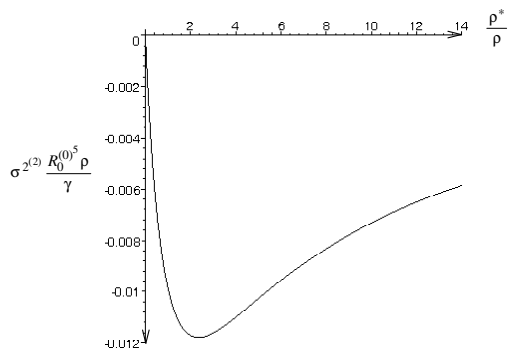

Figure 5-5. Change in $\sigma^{2^{(2)}}$ (multiplied by its scale factor) for small to intermediate density ratios for scaled wavenumber ($kR_0^{(0)}$) of 0.5 and $R_0^{(0)^*}/R_0^{(0)} = 2$.

unstable, the off-centering has a stabilizing effect. Although the neutral point is unaffected, the rate of growth is reduced. The off-centering provides non-axisymmetric disturbances, which in turn stabilize the bridge. However, lazy waves amplify the effect of transverse curvature against the longitudinal curvature; consequently, the bridge is always unstable in this region. The longitudinal curvature becomes more important for short wavelengths and in the stable region, each value of σ^2 produces two values of σ, which are purely imaginary and conjugate to each other. The disturbances corresponding to the wavelengths in this region neither settle nor grow. The bridge oscillates with small amplitude around its equilibrium arrangement. The bridge cannot return to its equilibrium configuration without viscosity, which is a damping factor. Once the bridge is stable, the off-centering offers a destabilizing effect because the wall is close to one region of the bridge and this delays the settling effect of longitudinal curvature.

Limiting conditions, usually provide a better understanding of the physics. In Figure 5-5, ρ^*/ρ is allowed to vary and it approaches zero and its effect on scaled $\sigma^{2^{(2)}}$ is given. The figure shows that the outer fluid loses its role when ρ^*/ρ approaches zero because the fluids are inviscid. Therefore, the bridge is expected to behave as if there were no encapsulant at all, thereby causing $\sigma^{2^{(2)}}$ to vanish. To

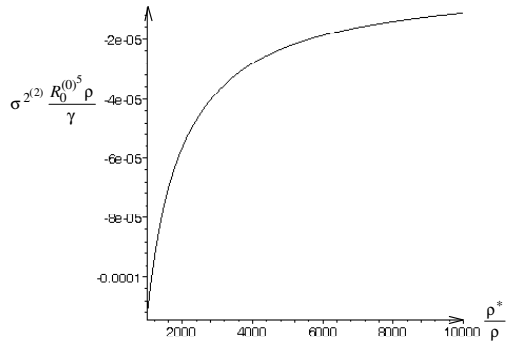

Figure 5-6. Change in $\sigma^{2^{(2)}}$ (multiplied by its scale factor) large density ratios for scaled wavenumber of 0.5 and $R_0^{(0)^*}/R_0^{(0)} = 2$.

see the behavior of the curve, the range of the plot is extended to $\rho^*/\rho = 14$. When ρ^*/ρ is very large, as shown in Figure 5-6, the outer liquid serves as a rigid wall and therefore $\sigma^{2^{(2)}}$ approaches zero. In other words, $\sigma^{2^{(2)}}$ approaches zero as ρ^*/ρ goes to either zero or infinity.

The ratio of the radii $R_0^{(0)^*}/R_0^{(0)}$ is another parameter that is examined and its effect is shown in Figure 5-7. As the ratio approaches unity, the azimuthal effect becomes more obvious. On the other hand, as the outer fluid occupies a very large volume, the off-centering effect settles down. As a result, $\sigma^{2^{(2)}}$ approaches zero and the bridge acts as if there was no outside fluid.

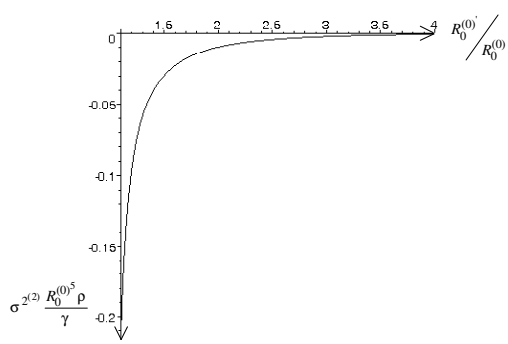

Figure 5-7. Change of $\sigma^{2^{(2)}}$ (multiplied by its scale factor) versus outer to inner radius ratio $R_0^{(0)^*}/R_0^{(0)}$ for scaled wavenumber of 0.5 and $\rho^*/\rho = 1$.

In summary, the physics of the problem indicate that the effect of off-centering is such that it does not change the break-up point of the bridge but it does affect the growth rate constant. The stable regions become less stable, meaning that the perturbation settles over a longer period of time, whereas the unstable regions become less unstable, therefore the disturbance grows slower. In addition, the physics of the off-centered problem indicates that the effect of off-centering is seen to even orders of δ and this required an algebraically involved proof.

It is important to understand the effect of off-centering the bridge because it can be technically difficult to center the bridge and this might have a technological impact when a float zone is encapsulated by another liquid in the crystal growth technique. Our next focus is to understand the complex interactions of geometry on the stability of liquid bridges. We will present our physical explanation of why a non-circular bridge can be more stable than its circular counterpart. We will prove our reasoning with elliptical liquid bridge experiments.

5.3.2 An Experimental Study on the Instability of Elliptical Liquid Bridges

In an earlier chapter we showed how an elliptic interface could help extend the stability in the Rayleigh-Taylor problem In this chapter we will consider the experimental extension of this idea to liquid bridges.

Liquid bridges have been studied experimentally as far back as Mason [46] who used two density-matched liquids, namely water and isobutyl benzoate and obtained a result for the ratio of the critical length to radius to within 0.05% of the theoretical value [12]. While most of the theoretical and experimental papers on liquid bridges pertain to bridges with circular cylindrical interfaces, there are some, such as those by Meseguer et al. [47] and Laverón-Simavilla et al. [48] who have studied the stability of liquid bridges between almost circular disks. Using perturbation theory for a problem where the upper disk is elliptical and the bottom

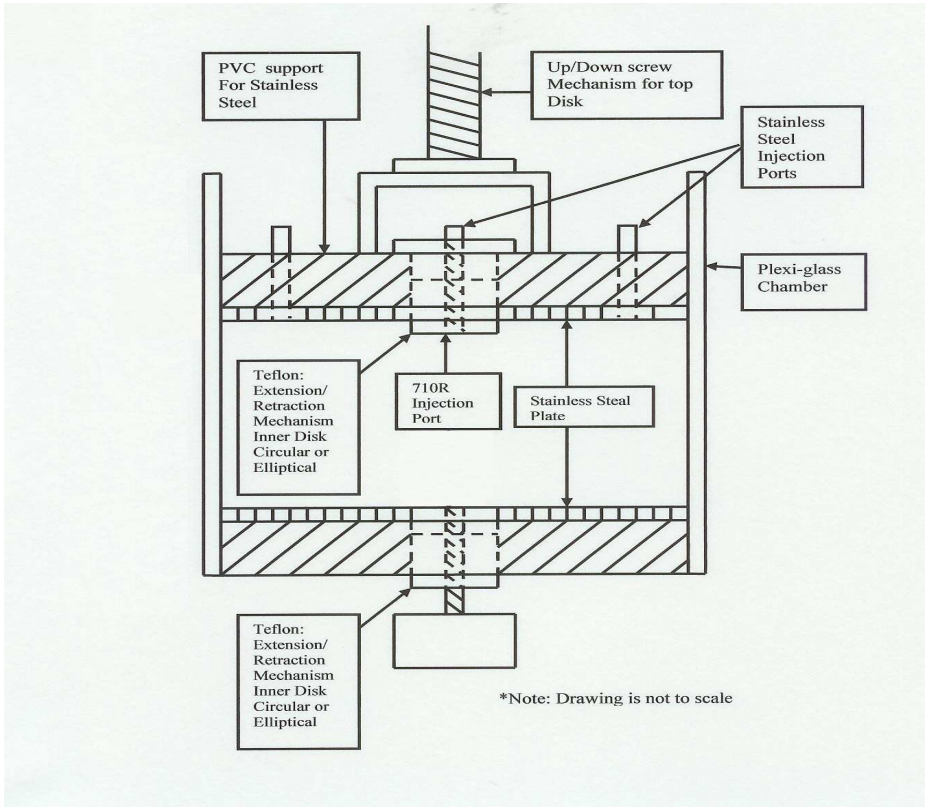

Figure 5-8: Sketch of the experimental set-up for elliptical bridge.

disk is circular, they deduced that it is possible to stabilize an otherwise unstable bridge for small but non-zero Bond number. Recall that the Bond number is given by the ratio of gravitational forces to surface tension forces. The earlier work of others and the earlier chapter on elliptical interfaces in the Rayleigh-Taylor problem, therefore, has motivated us to conduct experiments on the stability of liquid bridges between elliptical end plates and we now turn to the description of these experiments. Figure 5-8 shows a diagram of the experimental set-up. It depicts a transparent Plexiglas cylinder of diameter 18.50 cm, which can contain the liquid bridge and the outer liquid. The bridge, in the experiments that were performed, consisted of Dow Corning 710R, a phenylmethyl siloxane fluid that has a density of 1.102 ± 0.001 g/cm^3 at 25 °C. The density was measured with a pycnometer that was calibrated with ultra pure water at the same temperature. The surrounding liquid was a mixture of ethylene glycol/water as suggested by

Table 5-1: Physical properties of chemicals.

	$710R$	Mixture
Density (g/cm^3)	1.102 ± 0.001	1.102 ± 0.001
Viscosity (cSt) [49]	500	7.94
Interfacial tension (N/m) [49]	0.012 ± 0.002	

Gallagher et al. [49]. The outer fluid is virtually insoluble in 710R. Table 5-1 gives the physical properties of the chemicals used.

The bridge was formed between parallel, coaxial, equal diameter Teflon end plates. The outer liquid was in contact with stainless steel disks. Furthermore, a leveling device was used to make sure that the disks were parallel to each other. To ensure the alignment of the top disk, the leveling device was kept on top of the upper disk during the experiment. For the elliptical liquid bridge experiments, the end plates were superimposed on each other. This was guaranteed by marking the sides of the top and bottom disk, which were, in turn, tracked by a marked line down the side of the Plexiglas outer chamber.

The key to creating a liquid bridge of known diameter, and making sure that the disks are occupied completely by the proper fluids, is to control the wetting of the inner and outer disks by the two fluids. If the 710R fluid contacts the stainless steel surface, it will displace the outer fluid. Therefore, it was critical to keep the steel disks free of 710R and this was assured by a retracting and protruding Teflon disk mechanism. Prior to the experiment, the bottom Teflon disk was retracted and the top Teflon disk protruded from the steel disks. This helped in starting and creating the liquid bridge. Then, 710R fluid was injected from a syringe of 0.1 ml graduations through a hole of 20 thousandths of an inch (0.02 inches). A liquid bridge of around 1 mm length was thus formed in the absence of the outer liquid. Capillary forces kept this small-length bridge from collapsing. The outer liquid was injected through two holes of 0.02 inches, 180° from each other, so as

not to displace the 710R. The next step was to simultaneously increase the length by raising the upper disk and adding the 710R and outer liquid.

A video camera was used to examine the bridge for small differences in density. We were able to capture the image thanks to the difference in the refractive index between the bridge and the outer liquid. The loss of symmetry in the liquid bridge was an indication of the density mismatch. The elliptical liquid bridge is symmetric around the mid plane of the bridge axis, while the circular bridge has a vertical cylindrical interface; the shape of the bridge could then be checked via a digitized image.

The density of the mixture was adjusted before the experiment to 0.001 g/cm^3 by means of a pycnometer. However, during the experiment, finer density matching was required, and either water or ethylene glycol was mixed accordingly to adjust the density mismatch. The shape of the bridge was the best indicator to match the densities. In addition, the accuracy of density matching was increased substantially as the height of the bridge approached the stability limit. Extreme care was taken to match the densities when the height was close to the break-up point due to the fact that gravity decreases the stability point well below the Plateau limit for circular liquid bridges [50]. For example, we were able to correct a slight density mismatch, $\frac{\Delta\rho}{\rho}$ of 10^{-5} by adding 0.2 ml of water to 1 liter of surrounding liquid. This density difference is observable by looking at the loss of symmetry in the bridge. A similar argument also holds for elliptical liquid bridges. Depending on the amount of liquid added, either water or ethylene glycol, mixing times ranged from 10 to 30 minutes. In all experiments, sufficient time was allowed to elapse after the mixing was achieved so that quiescence was reached.

The top disk was connected to a threaded rod, which was rotated to raise it and increase the length of the bridge. The height of the bridge when critical conditions were reached was ascertained at the end of the experiment by counter

rotating the rod downward until the end plates just touched. One full rotation corresponded to 1.27 mm. The maximum possible error in height measurement was determined to be 0.003 inches over a threaded length of 12 inches. Therefore, the error in the total height measurement of the bridge was determined to be less than 0.24%. In addition to this, there was a backlash error that was no more than 0.035 mm. It turns out that this error amounts to a maximum of 0.11% of the critical height. The total error in the height measurement technique was therefore never more than 0.35%. The volumes of fluid injected into the bridge for the large and small bridges were 19.80 and 2.45 ml respectively. It may be noted from Slobozhanin and Perales [51] as well as from Lowry [25] that a 1% decrease or increase in the injected volume from the volume required for a cylindrical bridge results in a decrease or increase by approximately 0.5% in the critical height, respectively. Experiments with circular end plates were performed to ensure that the maximum error was very small.

5.3.2.1 Results on experiments with circular end plates

The experiments with circular end plates were performed for two reasons. First, the accuracy of the procedure and experimental set-up were verified by recovering the Plateau limit. Second, the typical break-up time for the circular bridge was measured to help estimate the waiting time for each increment when the elliptical end plates were subsequently used. The diameters of the circular Teflon end plates that were machined were measured by a Starrett Micrometer (T230XFL) to an accuracy of ±0.0025 mm as 20.02 mm and 10.01 mm respectively.

The lengths were increased in increments of 0.16 mm once the bridge height was about 3% lower than the critical height. Thereafter, for each increment the waiting time was at least 45 minutes before advancing the height through the next increment. When the critical height, as reported in Table 5-2, was reached the necking was seen in about 30 minutes and total breakup occurred in around 15

Table 5-2. Mean experimental break-up lengths for cylindrical liquid bridges. Upper and lower deviations in experiments are given in brackets.

	Break-up length (mm)	% change in length of the mean from theoretical critical
Large cylindrical bridge	62.84 (+0.02, -0.04)	-0.08
Small cylindrical bridge	31.48 (+0.09, -0.05)	+0.10

minutes after the initial necking could be discerned. Each experiment was repeated at least 3 times and the results were quite reproducible. A typical stable bridge at a height of 29.57 mm is depicted in Figure 5-9(a). The same bridge at breakup is shown in Figure 5-9(b) at a height of 31.57 mm. The reported values in the table do not account for the backlash and it should be noted that the increments in height were done in steps of 0.16 mm. Taking this into account, it is evident that the error in the experiment was very small, showing that the procedure and the apparatus gave reliable results. This procedure was useful in the follow-up experiments using elliptical end faces.

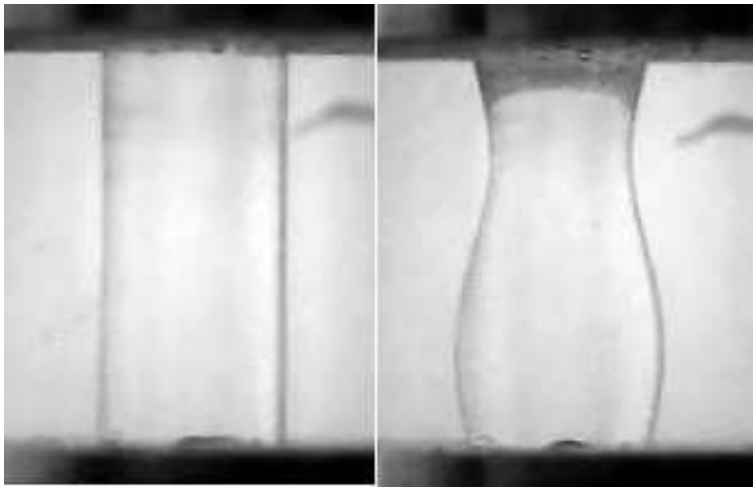

Figure 5-9. Cylindrical liquid bridge. Note that in this and all pictures the depicted aspect ratio is not the true one due to distortions created by the refractive indices of the fluids residing in a circular container with obvious curvature effects. (a) Stable bridge (b) Unstable bridge.

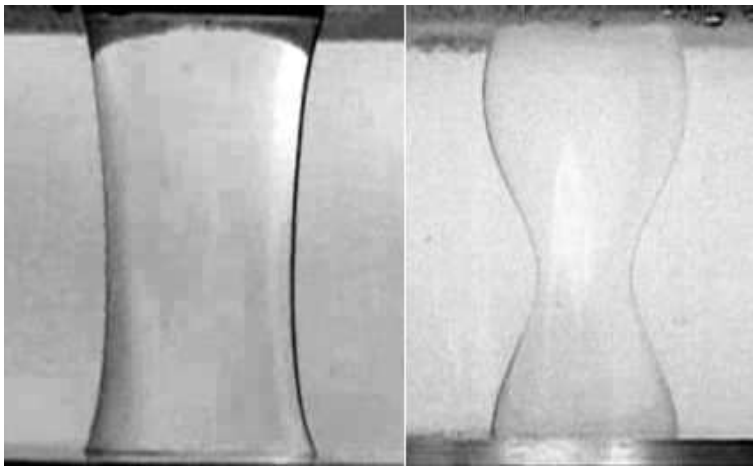

Figure 5-10. Large elliptical liquid bridge (a) Stable large elliptical liquid bridge. (b) Unstable large elliptical liquid bridge, before break-up.

5.3.2.2 Results on experiments with elliptical end plates

The major axes of the two elliptical Teflon end plates were measured to be 24.01 and 12.00 mm (± 0.0025). The minor axes were measured to be 16.80 and 8.34 mm respectively. For the large disc, the radius of a hypothetical companion circular end plate of the same area is 10.04 mm and for the small disc the companion radius is 5.00 mm; the deviation of the elliptical end plates from the companion hypothetical circular plates of the same areas was therefore close to 20%.

Table 5-3. Mean experimental break-up lengths for elliptical liquid bridges. Upper and lower deviations in experiments are given in brackets.

	Break-up length (mm)	% change in length from the critical height of the hypothetical companion circular bridge
Large elliptical bridge	64.90 (+0.10, -0.05)	2.86
Small elliptical bridge	32.29 (+0.09, -0.09)	2.74

The procedure that was used for the bridge generated by elliptical end plates was virtually identical to that used in the calibration experiments using circular end plates, described earlier. Figures 5-10(a) and 5-10(b) show the large elliptical liquid bridge at two different stages before and near break-up. Figures 5-11(a)

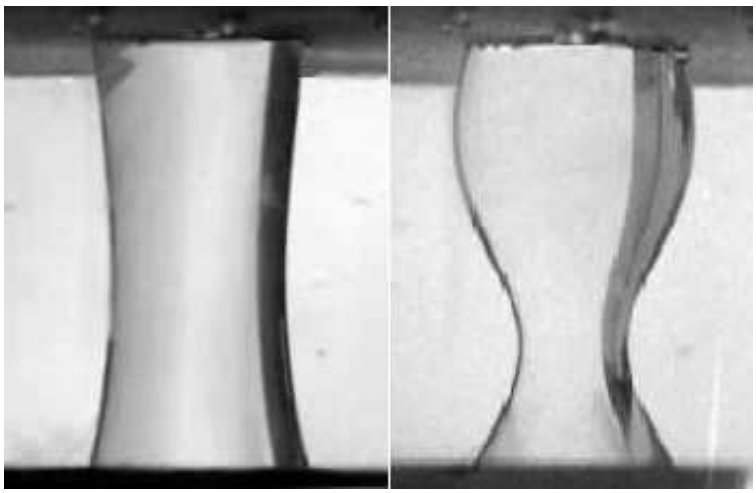

Figure 5-11. Small elliptical liquid bridge (a) Stable bridge. (b) Unstable bridge, before break-up.

and 5-11(b) are the analogous pictures for the smaller area elliptical bridge. We found that the increase in the break-up point was about 2.86% longer for the large end plate elliptical bridge, and nearly 2.74% longer for the small elliptical bridge showing that an elliptical bridge is in fact more stable than the companion circular bridge. The breakup heights for the elliptical liquid bridge experiments are given in Table 5-3.

Several comments may be made. First, a scaling analysis reveals that the ratio of the critical length of the deviated elliptical bridge to the critical length of its companion circular bridge can only depend on the percentage deviation of the ellipse from the circle, provided that the Bond number is negligible. This is why the enhancements in stability for the two sets of experiments with different ellipses are close to each other. Second, from a geometric argument, one can see that the stability limit can not change to first order when the elliptical disks are deviated from the circular disks by a small amount. This result was also obtained, albeit by calculation, by Meseguer et al. [47]. It would appear that the change in stability can be seen only at second order. Now, the deviation in the end plates used are about 20% and the observed increase in stability could be attributed

to the magnitude of this deviation or simply because the second order effect is strong enough to show the change. The third observation is that even slight density mismatches lead to asymmetry which becomes most pronounced near or at break-up. This is not surprising as imperfections become dominant near bifurcation points as seen in the theory of imperfections [52]. The imperfection due to density mismatch can only advance the breakup and so the experimental results must give a lower bound to the instability limit that one would predict from theory [52]. In summary, non-circular liquid bridges with geometrically similar end plates can be expected to offer greater stability than their circular counterparts. We have shown this to be true in the case of elliptical liquid bridges by way of experiments.

5.4 Shear-induced stabilization of liquid bridges

As already mentioned, a liquid bridge in a non-zero Bond number has a lower stability limit than the Plateau limit. Like gravity or density difference, flow also changes the morphology of an otherwise vertical liquid bridge interface. This change occurs on account of uneven pressure differences across the interface through its axial length. In other words, non-zero Bond number bridges in the absence of flow and flow with zero Bond numbers offer the liquid bridge or melt zone less stability. These facts led Lowry and Steen [53–55], Chen et al. [56] and Atreya and Steen [57] to investigate how both destabilizing effects could be judiciously combined to cancel one another and actually enhance the stability of a liquid zone, even enhancing the stability beyond the classical Plateau limit. It should be noted however, that to surpass the Plateau limit is very difficult and was never successfully completed experimentally with a constant flow rate.

They performed a series of impressive experiments with bridges of non-zero Bond numbers. These bridges were encapsulated by an outer fluid that was allowed to flow through vertically. The liquid bridge was anchored to two end plates that were connected by a centering rod. Such a centering rod has no effect on the

stability when flow is absent but its presence does modify the flow dynamics when a shearing outer fluid is taken into account. The experiments showed stabilization of the interface and the reasons advanced indicated that a shearing flow could "straighten out" a bulging bridge, depending, of course, on the direction of flow. In other words, the flow can suppress the deviations from a vertical cylindrical interface, balance gravity, and consequently, stabilize an otherwise unstable static bridge by as much as 5%. The stabilization that they achieved even reached the Plateau limit. The experiments, which showed stabilization due to shear, did not produce any stabilization beyond the Plateau limit due to the narrow range of such a possibility and attendant experimental difficulties.

The work in this study continues the idea of stabilization of non-zero Bond number bridges due to shear. However, the question posed is how would flow induced in a closed geometry which is closer to the technological application, i.e., floating zone method, affect the stability of liquid bridges. The major difference between this work and earlier efforts is that the fluid flow in the outer compartment is in a confined geometry, not a flow through configuration, no inner rod will be used, and larger density differences are examined. Again, the reason for considering this configuration is motivated by the fact that the liquid encapsulated melt zone process, which is a specific FZ technique, yields flow profiles in closed compartments.

In short, the overall goal is therefore to study shear-induced recirculating flow, as shown in Figure 5-12, and its effect on the stability of a liquid bridge. There are many factors that come into play when considering how one must design an apparatus to achieve our goals. For example choosing the right fluids with desirable viscosities and choosing a sensible bridge radius to outer wall radius ratio. We begin with a scoping numerical calculation that will assist establishing the dimensions of the experimental setup and the chemicals that constitute the

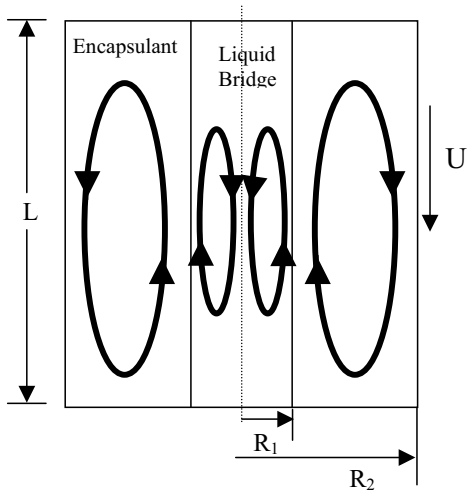

Figure 5-12. The schematic of the returning flow created in the presence of an encapsulant in the floating zone technique.

bridge and the encapsulant. Once the dimensions and the chemicals are decided, a method by which to characterize the stability of a liquid bridge is described. Then, the experimental setup, the chemicals, and identifies the accuracies in the measurements are presented. Lastly, the results of the experiments are presented. The effect of each parameter such as the speed of the moving wall and the effect of the Bo is studied along with the physical explanation and comparison with the numerical results whenever possible. As a final point, a summary of the results and the collection of the messages are given.

5.4.1 A Model for Scoping Calculations

To guide our experiments, a model was developed for steady flow of two Navier Stokes fluids in a configuration depicted by Figure 5-12. Both inertial and viscous terms are taken into account in the model. The input parameters to the model are the bridge radius, the outer compartment radius, the length of the bridge, the viscosities and densities of the fluids, and the wall speed. The calculated information of interest is then the flow profiles in both regions, bridge and encapsulant, which also defines the conditions when the flows are nonaxisymmetric. A nonaxisymmetric flow would create unwanted disturbances

Table 5-4. The effect of the viscosities on the maximum vertical velocity along the liquid bridge interface, $v_{z,max}$. The densities of the liquids are 1g/cc each, the height of the bridge is 3 cm, the outer radius is 2.5 cm, and the radius of the bridge is 0.5 cm. The flows were determined to be axisymmetric.

$\mu_1(cP)$	$\mu_2(cP)$	$v_{z,max}/U$
150	1	0.0015
50	50	0.0154
1	5	0.3455
1	1	0.1667

because the effect of these flows on bridge stability are not easily predictable. The numerical model is approximate in that a vertical shape of the interface is assumed. It is noteworthy that a model worked in the Stokes limit with stress free horizontal walls, yet assuming a deformable interface was proposed by Johnson [58]. Our numerical solution was obtained with no slip conditions and by including inertial terms. From Johnson's calculations, we gather that the flow intensity in the bridge increases with an increase in viscosity ratio between the outer and inner fluids, which was also verified by our computations.

The following calculations use a finite element method and were done with an accuracy of $\epsilon = 10^{-6}$ (L^2 norm of the computed residual). The model is made up of $150x165$ quadrilateral finite elements (piecewise Q2 approximation for the velocity field and piecewise Q1 for the pressure), built up on $301x331$ nodes in the radial and axial directions, respectively. This spatial discretization leads to an algebraic system of $199,262$ unknowns to solve for the velocity field. The numerical model was extremely helpful in determining appropriate viscosities and radius ratios. Table 5-4 shows some of the results for the interface velocity scaled by the wall speed for various viscosities. Three bridge radii of 0.5, 1, and 1.5 cm were chosen for the computations while the outer compartment radius was fixed as 2.5 cm. Two of the radius values represent the actual dimensions that were used in the experiments and the experimental choices reflected logistics as well as machining

ease. For computational purposes, the height of the bridge was chosen to be 3 cm for a bridge of 0.5 and 1 cm radius while it was varied between 4 and 6 cm for a bridge of 1.5 cm radius. The height is a convenient adjustable variable in an experiment. The values of height chosen for the smaller radius computations were based on being in the vicinity of the Rayleigh Plateau limit i.e., height /radius being 2π. The heights chosen for the larger radius, on the other hand, reflect the fact that flow could only increase by increasing the height from the lower radius bridge, but not so large that difficulties due to Bo would arise.

Some of the features of the detailed numerical model that was used to determine the flow profiles in the bridge can be guessed from a simple scaling analysis. A rough scaling argument from a one-dimensional model for a two fluid system reveals the dependence of the velocity along the interface of the bridge on the parameters in the problem at constant outer wall speed. In the one-dimensional model, a moving wall in contact with an outer fluid that encapsulates an inner core fluid anchored by a very thin stationary rod is assumed. Subscripts one and two refer to the inner and outer fluids respectively, and thus the fluid velocity at the interface scales with the moving wall speed as

$$\frac{\mu_2 \left[U - v_z \left(r = R_1\right)\right]}{\left[R_2 - R_1\right]} = \frac{\mu_1 v_z \left(r = R_1\right)}{R_1} \tag{5–65}$$

which yields to

$$v_z \left(r = R_1\right) = \frac{U}{1 + \dfrac{\mu_1}{\mu_2} \dfrac{\left[R_2 - R_1\right]}{R_1}} \tag{5–66}$$

This simple expression suggests increasing the outside liquid's dynamic viscosity, decreasing the bridge's viscosity, or increasing the bridge's radius, for fixed wall radius, R_2. This conclusion is also justified by the results of the detailed computations displayed in Table 5-4.

Table 5-5. The effect of viscosity on the maximum vertical velocity along the liquid bridge interface. The densities of the liquids are 1g/cc each, the height of the bridge is 3 cm, the outer radius is 2.5 cm, the viscosities are 1 cP for each liquid. The flows were determined to be axisymmetric.

R_1 (cm)	$v_{z,max}/U$
0.5	0.1667
1.0	0.2500
1.5	0.3559

The results in the table portray more than the scaling argument. For example observe that while the scaling argument relates the velocities to viscosity ratios, the computations show the importance of individual viscosities. In fact the calculations shown in the table tell us that if the viscosities are the same, it is better to have less viscous liquids. As an instance the $v_{z,max}/U$ ratio can be increased by an order of magnitude, if the viscosities are 1 instead of 50 cP.

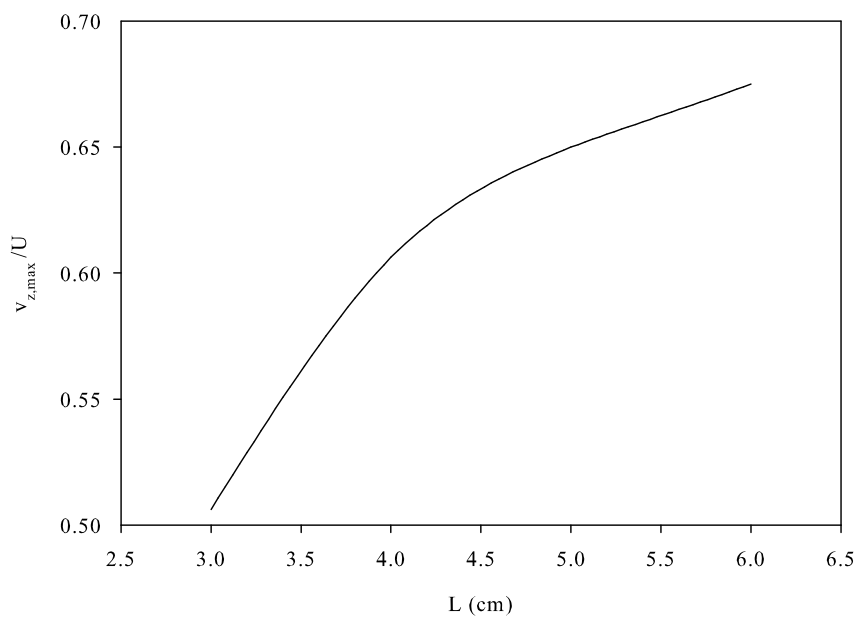

Figure 5-13. The effect of the height of the bridge on the maximum axial velocity along the liquid/liquid interface. The densities of the liquids are 1g/cc each, the outer radius is 2.5 cm, the radius of the bridge is 1.5 cm, and the viscosities are 1.4 and 270 cP for the bridge and encapsulant, respectively.

It is noteworthy that unlike the conclusion obtained from the one-dimensional model the viscosity ratio cannot alone determine the flow regimes in a closed compartment model. Pressure gradients are important and thus viscosity can never be scaled as a pure ratio in closed compartment models.

To see the effect of radius ratio, more calculations were done assuming that the viscosities of both fluids are 1 cP. The results are presented in Table 5-5. As expected, it is found that as the radius increases, the ratio $v_{z,max}/U$ increases and thus more momentum is transferred to the liquid/liquid interface. Doubling the radius gave an increase of 1.5 times the velocity.

To see the effect of height a bridge of radius 1.5 cm was chosen in the computations. The speed at the interface for a given U is expected to increase by

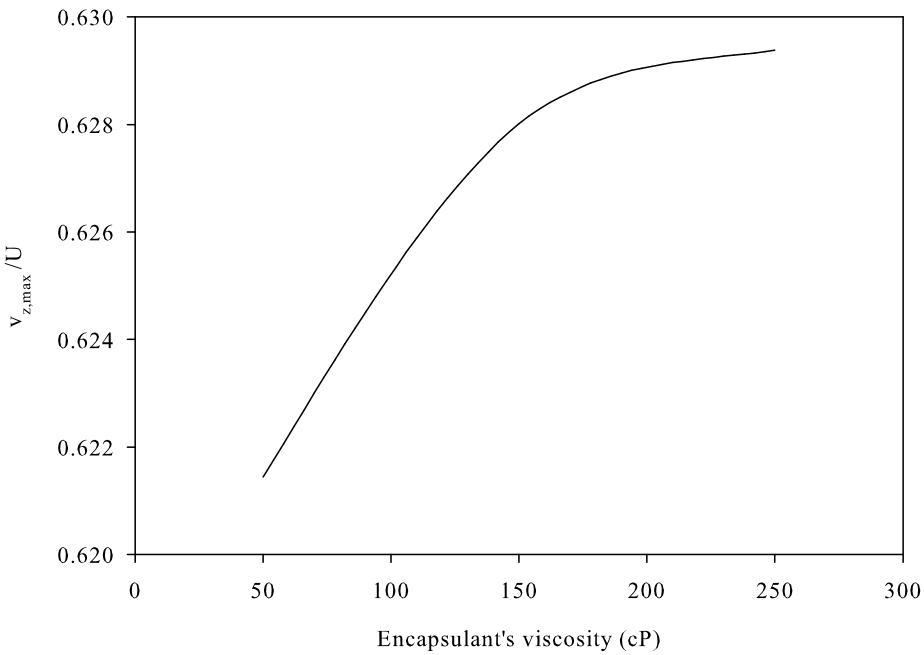

Figure 5-14. The effect of the encapsulant's viscosity on the ratio of maximum speed observed at the interface to the wall speed. The densities are 1.616 g/cc, the outer radius is 2.5 cm, the radius of the bridge is 1.5 cm, and the viscosity of the bridge is 1.2 cP. The height of the bridge is 5.9 cm.

increasing the height of the bridge because the gap ratio, $\frac{L}{[R_2 - R_1]}$, gets larger. This increasing trend is shown in Figure 5-13. For these computations, the viscosities of the bridge and the surrounding liquid are 1.4 and 270 cP, respectively.

These calculations led us to choose the chemicals and the radius ratios. In our experiments, we settled upon a 3M liquid, HFE 7500, which has a viscosity of approximately 1.2 cP for the inner fluid while the outside liquid was a mixture of sodium polytungstate and glycerine of viscosity around 250 cP. The radius of the bridge was chosen to be either 0.5 cm or 1.5 cm.

One last important parameter to study is the effect of the viscosity on the speed at the interface. This is important because the viscosity depends on temperature, which can change at each experiment. As seen from Figure 5-14, even if the viscosity changes from one experiment to another, the maximum speed at the interface does not change considerably.

5.4.2 Determining the Bond Number

The shape of a liquid bridge is characterized by its Bond number, the contact angle, length to radius ratio and the ratio of the volume injected to the volume that corresponds to a vertical cylindrical bridge of the same dimensions. Determining the Bo, however, is not an elementary matter because the interfacial tension, which is needed to determine the Bond number, is not easily measured. Moreover, in an experimental environment a degree change in temperature can cause the Bo to change by as much as 10^{-1} because of the change in the densities. Aside from using direct measurements of physical properties to determine Bo, two other methods were investigated. One is by image analysis where the shape of a bridge is compared with calculations. This method requires high resolution imaging which in turn requires complicated equipment and was therefore discarded. The other method arises by noting that the critical breakup length depends upon the Bo. This means that one can experimentally determine the critical breakup length

and use theoretical calculations to obtain the Bo that must correspond to such a breakup length. Here, we adopted the latter method to determine the Bond number. In particular we used Brakke's Surface Evolver (SE) program for the stability calculation [59, 60].

The input parameters for such a calculation are the volume of the liquid in the bridge, the contact angle at the end plates, the critical height at breakup, the bridge radius and a guess Bond number. The output of the calculation is the time constant for the decay or growth of infinitesimal disturbances. For a given set of parameters the guess Bond number is changed until neutral stability is obtained i.e., until the time constant is just zero. The guess Bo that gives neutral stability is the Bo number for the experimental system. The SE software whose accuracy depends upon adjustable numerical tuning parameters such as grid refinement was tested in the zero Bond number case by recovering the Plateau limit and also by verifying the results available in graphical form by Lowry [25]. Of course this method of determining the Bond number of an experiment assumes that the critical height can be accurately measured. As explained later this was ensured by recovering the classical Plateau limit for a zero Bond number configuration and in fact was how we 'calibrated' the correctness of our experimental procedure. We now move to a discussion of the experimental setup, the chemicals used and the procedure employed.

5.4.3 The Experiment

5.4.3.1 The experimental setup

The experiments were performed in a Plateau chamber made of a transparent Plexiglas cylinder of diameter 5 cm in which fluid shear could be induced by wall motion. The setup is depicted in Figure 5-15. The end plates were composed of two materials. The inner part was made of circular Teflon disks with which the bridge was in contact. The encapsulating liquid was in contact with the outer part

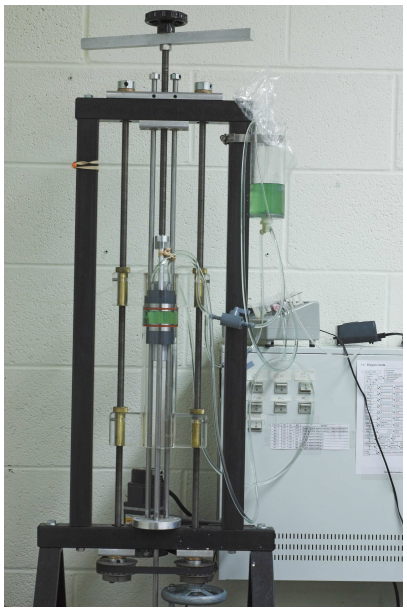

Figure 5-15: Photograph of the experimental set-up.

of the disks, which was made of stainless steel. Two sets of liquid bridge radii were used in these experiments. The diameters of these end plates were measured by a Starrett Micrometer (T230XFL) as 10 and 30 mm with an accuracy of ± 0.0025 mm. The top disk was connected to a threaded rod, which was rotated to raise or lower it and thereby change the length of the bridge while the bottom disk was kept fixed. The Plexiglas wall containing the liquids was threaded through two large rods, which in turn were connected to gears attached to a servo motor BXM230-GFH2 with a gear reduction head GFH2-G200. The motor's speed was adjusted by its own controller. A wide range of speeds was accessible by selecting different gear ratios. Moreover the direction of the motion could be changed. Teflon o-rings were used in grooves at both top and bottom disks to provide a slippery surface between the wall and the disks and to ensure that the encapsulant fluid did not leak out. Figure 5-15 shows a photograph that gives a perspective of the operating span with respect to the test section.

The chemicals chosen were a solution of sodium polytungstate and glycerine as the encapsulant and a 3 M HFE-7500 as the liquid bridge. The density of HFE-7500 is 1.61 g/cc and its viscosity is 1.2 cP. The density of sodium polytungstate solution can be easily adjusted from 1.00 g/cc to 3.10 g/cc. In these experiments, we started with a solution of density 2.85 g/cc and mixed it with glycerine to obtain nearly the same density as that of the bridge. Before the experiment, the density of the outside solution was measured with a hydrometer to an accuracy of 0.0001 g/cc. Glycerine served the dual purpose of lowering the density of the salt solution and increasing its viscosity. The scoping computations that assisted in the design of the experiment tell us clearly that the viscosity ratios of the outer to inner fluids must be large to effect reasonable shear. Our choice of fluids and the need to adjust the viscosity of the outer fluid reflected the messages conveyed by these calculations. The viscosity of the outside solution therefore was varied between 200 to 250 cP depending on the salt/glycerine ratio for each experiment. In this regard, the reader might observe from Figure 4 that the maximum possible momentum transfer is reached even with the lowest viscosity of 200 cP for the outside fluid. This range therefore assured that viscosity would not play a factor between different experiments. It is important to note that although the viscosities were high, experiments were conducted to ensure that no viscous heating took place. A rotating disc viscometer in the non-isothermal mode was repeatedly run for several minutes with the encapsulant fluid to see if viscosity and temperature changed over time. Since viscosity, which depends on temperature did not change over time, there was very little concern that viscous heating would in turn affect the Bo number.

5.4.3.2 The experimental procedure

The key techniques needed to initiate and establish a liquid bridge are discussed in an earlier study [61]. As observed, the shape of a bridge depends

on the volume of the liquid injected, its Bond number and the spacing between the end plates. The accuracy of spacing and radius measurements and the method for determining the Bond number were discussed earlier. This leaves us to specify the accuracy of the volume of fluid injected, as this is also important. The volumes were controlled with syringes, which had 0.1 and 0.2 cc graduations for the 10 and 30 mm diameter bridges respectively.

The setup and the procedure to determine the breakup point were calibrated by recovering the Plateau limit. The breakup point was found to be 3.143 cm ± 0.010 cm for the small diameter bridge. The calibration experiments were done with the small diameter end plates to ensure that the effect of slight temperature changes was minimal on the Bond number. It is important to observe that the change of density arising from temperature fluctuations is amplified by nine times when the large disks are used, as Bo is proportional to the square of the radius. The details of the procedure and the attendant errors in recovering the Plateau limit are discussed by Uguz et al. [61].

Guided by the numerical results, keeping the volume of the liquid in mind, the density and viscosity of the outside liquid was adjusted so that shear could have an effect on the stability of the bridge. The aim of the experiments was therefore to create flow in the outside liquid to minimize the destabilizing effect of the density imbalance and help stabilize the bridge. Shearing the wall creates a returning flow in the outside liquid, which in turn creates a returning flow in the liquid bridge. Note that the flow in the bridge is in opposite direction to the direction of the wall (See Figure 5-16). Consequently, if the bridge bulges from the bottom, the wall is moved downward to create a flow such that the interface becomes more symmetric. It is worth reminding the reader that there was no centering rod used in these experiments. Although such a rod would not have any effect on the stability of

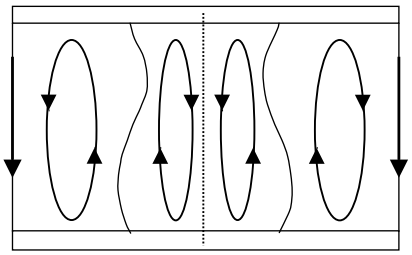

Figure 5-16. A cartoon of a bridge bulging at the bottom. The wall is moved downward with the objective of obtaining a symmetric interface with respect to the mid plane.

a non-shearing bridge, it would have changed the flow profiles and therefore the stability point when the wall is moved.

The expectation of the experiments was to obtain measurably more stable bridges with flow than without flow. The height of the bridge was measured with a Starrett caliper with a resolution of 0.01 mm and accuracy of ± 0.03 mm. This is the only error that matters in our reported results as only percentage changes in critical height are of interest.

The procedure of the experiment was as follows. The bridge was first created in the absence of shear. Once the desired volume of the bridge was injected, the valve connected to the inner liquid injection port was closed. This is extremely important as the pressure gradient created in the chamber by moving the wall or the upper disk can alter the bridge volume. The breakup point of the static bridge was found at this volume by slowly increasing the height of the upper disk in small increments and giving ample time for disturbances to settle down or grow before each increment. When increasing the height of the bridge, the encapsulant was drained into the outside compartment from an exterior liquid chamber. Once the breakup point was found, the volume and the breakup height of the bridge sufficed to compute the Bond number using the SE solver. The wall was moved at a constant velocity in the stabilization direction once the bridge started to break. Moving the wall changed the shape of the bridge immediately. While the

wall was moving, the spacing, i.e., the height of the bridge, was increased in small increments of 0.008 cm. The breakup point of the bridge was then found in the presence of shear at the established wall speed. The breakup height in the presence of shear and the injected volume were used to compute a Bo as if there was no flow. This Bo is referred to as the "Apparent Bo". Thus each experimental set for a given injected volume comprised of finding the breakup point for the static bridge and the break up points for the shearing for different wall speeds ranging between 42 and 168 cm/hr with a manufacturer's error of ± 0.08 cm/hr. The next step was to increase the volume of the bridge and repeat the set of experiments. Since temperature could change slightly from one experimental set to another, the breakup lengths and the Bo were calculated for each new volume and wall speed data. In the next section the results of the experiments are presented.

5.4.4 The Results of the Experiments

In running the experiments, two different radii for the bridge's end plates were used viz., 0.5 and 1.5 cm. However, no significant increase in stability was achieved with the small radius bridge. This result is in accordance with the scoping calculations presented in Table 5-5. Therefore, in this section we only present the data corresponding to the bridge of 1.5 cm radius. We will discuss two major effects on the percentage increase of the breakup height: first, the effect of the wall speed and second, the effect of the injected volume. This classification allows us to view the data with different perspectives, as it is helpful in identifying the role of each parameter in the experiment explicitly. A summary will serve to tie the results together.

We start our discussion with Figure 5-17, which presents the percentage increase in the breakup height in the presence of flow for a given Bo and for various bridge volumes.

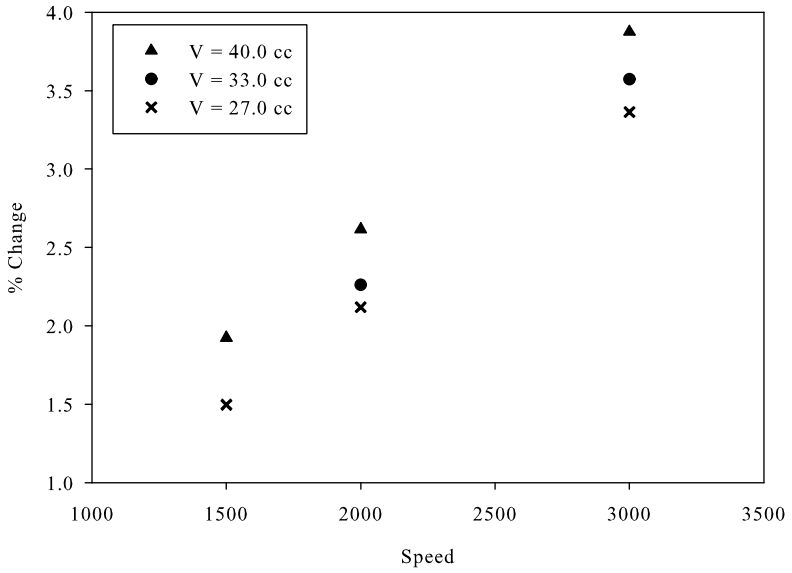

Figure 5-17. The effect of wall speed on the percentage increase in the breakup height of the bridge for various volumes. The radius of the bridge is 1.5 cm, the Bo is 0.218 $\pm$ 0.006, and to obtain the linear wall speed in cm/hr multiply the abscissa by 0.056.

Three observations can be made from Figure 5-17. First, introducing shear certainly stabilizes the liquid bridge. Therefore it can be concluded that the flow acts to reduce the effect of gravity. Second, for the experiments reported in the figure the breakup height of the bridge increases as the applied speed increases. Visual observations of the bridge showed that it did not achieve near symmetry even for the largest wall speed employed. This means that even the largest speed was not enough to overcome the destabilizing effect of gravity or in other words, correct the density difference. Third, the greater the injected volume the more stabilizing the flow becomes. This is seen explicitly in Figure 5-18 which displays the percentage change versus the injected volume. To understand why this occurs observe that as the volume injected increases, the breakup height of the static bridge increases. As the height to radius ratio increases, the effect of the flow

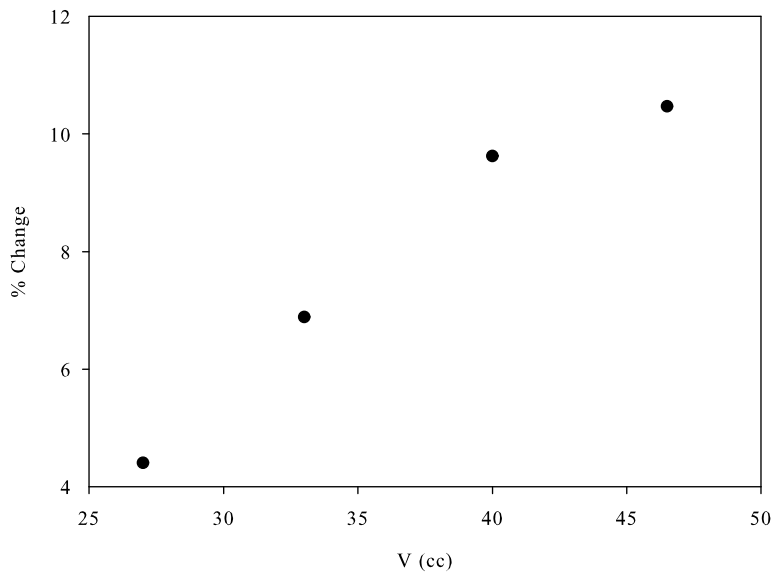

Figure 5-18. The effect of the volume on the percentage increase in the breakup height of the bridge. The radius of the bridge is 1.5 cm, the Bo is 0.118 ± 0.017, and the speed is 3000 (168cm/hr).

becomes more pronounced. This also expresses the numerical trend seen earlier in Figure 5-13.

It is noteworthy that at some height, the percentage increase in the breakup height in the presence of flow begins to plateau or become constant. This is believed to occur because the height to radius ratio is very large and does not provide any more increase in the momentum transfer of flow to the bridge. In fact in some experiments for a given Bo, we observed a decrease in the percentage change for large volumes. This is logical, if it is remembered that the breakup height of the bridge changes very slowly with a large increase in the volume [25]. In addition, the larger the volume the greater the "weight" of the bridge and the more difficult for the flow to have an impact.

Figure 5-19 which displays data for a fixed bridge volume shows that for a given Bo, increasing the flow rate enhances the percentage change in the breakup height of the bridge. If the flow is strong enough, the interface becomes symmetric

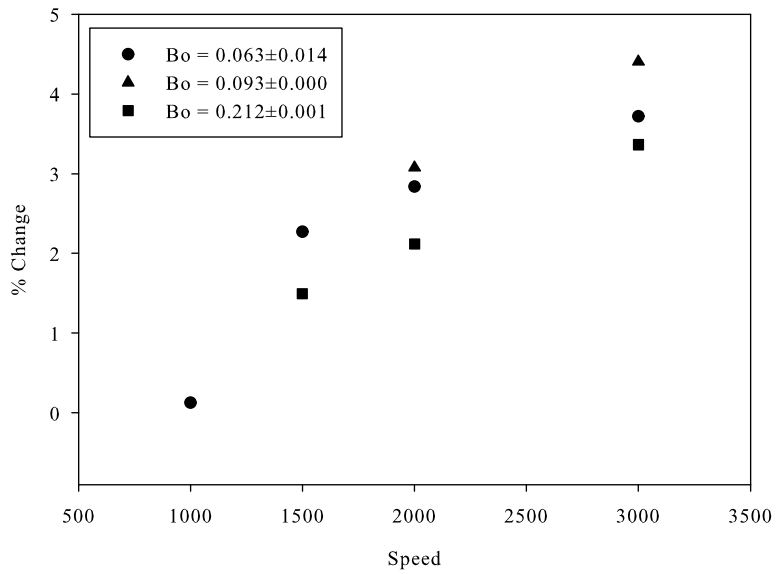

Figure 5-19. The effect of the wall speed on the percentage increase in the breakup height of the bridge for various Bond numbers. The radius of the bridge is 1.5 cm, the volume is 27.0 cc. To obtain the linear wall speed in cm/hr, the abscissa is multiplied by 0.056.

at the breakup of the shear-induced bridge. The aim is to get a zero "Apparent Bo" with flow. This statement implies that the greatest percentage increase would occur for the largest Bo bridge. However, when Bo is very large, e.g. $Bo = 0.212$ it is seen from the figure that the available shear was insufficient to effect a considerable change in the stability point. This also implies that the apparent Bond number for all three cases was not the same for a given wall speed. By contrast when the Bond number is small, even if a zero Apparent Bo is reached by introducing flow, the percentage change in the height is little because the bridge is almost symmetric when flow is introduced and little correction of the interface shape is permissible. Consequently, for this experimental apparatus, the maximum percentage stabilization is obtained for intermediate Bo bridges and this is the point of Figure 5-19.

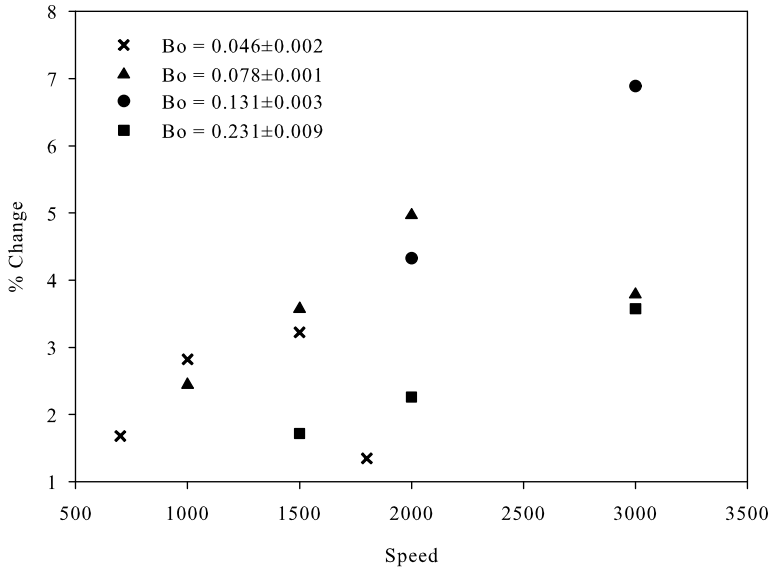

Figure 5-20. The effect of the wall speed on the percentage increase in the breakup height of the bridge for various Bond numbers and larger volume. The radius of the bridge is 1.5 cm, the volume is 33.0 cc. The speed is dimensionless. To obtain the speed in cm/hr, the current speed needs to be multiplied by 0.056.

As we saw one way to enhance the momentum transfer is to increase the volume of the bridge. Figure 5-20, which is similar to Figure 5-19, is obtained for a higher volume i.e., for 33.0 cc of injected volume. Aside of the fact that the results are more dramatic there are other features that are interesting. For example the increasing wall speed initially causes an increase in the stability until a maximum is reached and thereafter a decrease in the stability enhancement. This calls for an explanation. When the wall speed is small, the bridge which in its static configuration bulges from the bottom (say) becomes more symmetric and the stability is enhanced. As also observed by Lowry [25] as the wall speed is increased and the flow gets stronger, it actually "over corrects" the shape of the bridge and flips the direction of the bulge i.e., causing the bulge to appear at the top. This is particularly true for the small Bo bridges, e.g., $Bo = 0.04$ and 0.08. Thus, there are two points on the curve where the breakup height is the same but the breakup

occurs from the bottom for the first point, and from the top for the second one. This is also believed to be true for the larger Bond number bridges but the wall speed needs to become large enough to see the maximum, something that was not possible with the available apparatus. For example in the case of $Bo = 0.13$ and $Bo = 0.23$, even the largest speed permitted by the current apparatus was not enough to flip the direction of the bulge. Consequently, no maximum of percentage increase was observed for these large Bo bridges.

As we conclude our discussion of the experimental results we note that the "Apparent Bond number" which is another way of expressing the critical height to radius ratio when shear is employed could become as low as 0.001. This was obtained at a speed of 2000 (112 cm/hr) for a bridge whose Bond number was 0.124.

The main features of the experimental results are summarized by three statements. First, for every wall speed there exists an optimum Bond number bridge where the maximum stability is obtained. The value of this optimum must of course depend on the shearing apparatus employed and the fluids chosen. Low Bond number bridges have a narrow window of stability while high Bond number bridges cannot easily be stabilized on account of shearing limitations. Second, for every Bond number there is an optimum wall speed at which maximum stability is obtained for at low wall speed the shearing is insufficient while at very high speeds the shape of the bridge over corrects and bulges from the opposite end. Third, an increase in bridge volume leads to an increase in momentum transfer. The stabilization change in the bridge therefore increases until plateau is reached.

CHAPTER 6
CONCLUSIONS AND RECOMMENDATIONS

In this chapter, the main results of this dissertation are re-evaluated and future work is proposed. This dissertation has involved advancing the understanding of the Rayleigh-Taylor (RT) and liquid bridge problems by comparing the two problems and finding ways to delay the instabilities. It was shown that the stability point has been affected both by the geometry of the system and the flow.

In an attempt to understand the effect of geometry and flow on the stability of both problems a theory was advanced for the RT problem while experiments were performed for liquid bridges. The RT problem was studied theoretically because of the relative simplicity in using the two-dimensional rectangular Cartesian coordinate system to learn about the physics while experiments, are complicated because of the inability to adhere to this two-dimensional assumption. A theory for liquid bridges on the other hand is more complicated because of the cylindrical coordinate system while, the experimental complications seen in RT problem are avoided in experiments on the bridge.

One major conclusion of the theory in the RT problem is that inducing diffusion paths for perturbations enhances the stability. Another major conclusion of the theory is that shear-driven flow enhances the stability if the flow field is closed and the interface is allowed to be flat in the base state. In addition, another major conclusion from the theory is that two windows of stabilities are obtained for some parameters. This means that there are multiple width ranges where flow can offer stability. However, if the flow were open regardless of whether it is in the inertial or Stokes limit the instability would either be advanced or remain unaffected.

The conclusions from our theoretical study raise questions that ought to be addressed in the future. The first question is whether there are theorems on stability that may be obtained for geometries of arbitrary shape that could give either upper or lower bounds on the stability or both. This would possibly involve the use of variational principles. Another question that could be studied in the future is why there is a sudden change from a delay in the instability when flow is present at an erstwhile flat surface to the sudden advancement in instability when the interface is not flat in the base state. In other words, we might wonder why the instability does not change slowly and continuously as the interface goes from being flat in the base state to non-flat in the base state when flow is present. This would involve theory of asymptotics on imperfections and such a theory would also have to address the situation where multiple stability windows are present.

The major conclusions of the experiments on liquid bridges are that elliptical end plates in the liquid bridge enhance stability and flow enhances stability provided the Bond number is non-zero. These conclusions entertain several possibilities for the future. The first problem for future research is connected to the manner in which an elliptical bridge breaks off. It does so in a symmetric manner from the mid point i.e. the half way point between the end plates presumably because the mid point is of circular cross section. If the end plates were twisted with respect to each other the base state topology would change and this would raise the question on where cross sections would be circular and how the stability would be affected. Elliptical bridges are open to more questions. It would be interesting to see what would happen to the stability point if the deviation of the elliptical end plate from the circle were not small. A theory supporting these experimental results is also of interest. The theory may be developed either by using a perturbation theory or by using elliptical coordinates. In the first case, the ellipse is deviated from a circle by a small amount. The latter offers a theory,

which is also valid for highly elliptical plates that would serve for two purposes: obtain the stability of highly elliptical bridges and determine the validity of the perturbation calculation.

Another problem for future study is connected to flow stabilization of liquid bridges. It was observed that flow stabilizes a non-zero Bond number bridge depending on its direction. A bridge with elliptical end plates cannot be vertical. It would be interesting to build a setup to investigate the stability of elliptical bridges subject to flow. Would they offer greater stability compared to circular bridges?

APPENDIX A
THE PERTURBATION EQUATIONS AND THE MAPPING

In this appendix, the perturbation equations and the mappings used in the theoretical work are explained. The reader is referred to Johns and Narayanan [10] for the details.

Let 'u' denote the solution of a problem in an inconvenient domain D where D may be not specified and then it must be determined as part of the solution. The meaning of the term inconvenient may be understood when a calculation similar to that of the off-centered bridge presented in Chapter 5 is studied.

It would be possible to obtain the solution u and the domain D if the same problem is solved on a regular domain D_0 , which is called the reference domain. The perturbation calculation and the mapping require the inconvenient domain D needs to be expressed around D_0 in powers of a small parameter ϵ. Therefore the solution u and the domain D are solved simultaneously in a series of companion problems. The points of D_0 will be denoted by the coordinate y_0 and those of D by the coordinate y. The x-coordinate is assumed to remain unchanged. Therefore, 'u' must be a function of ϵ directly because it lies on D and also because it is a function of 'y'. The point y of the domain D_ϵ is then determined in terms of the point y_0 of the reference domain D_0 by the mapping

$$\mathrm{y} = f\left(\mathrm{y}_0, \epsilon\right) \tag{A–1}$$

The function f, can be expanded in powers of ϵ as

$$f\left(y, \epsilon\right) = y_0 + \epsilon y_1 + \frac{1}{2}\epsilon^2 y_2 + \cdots \tag{A–2}$$

where

$$y_0 = f\left(y_0, \epsilon = 0\right) y_1\left(y_0, \epsilon\right) = \frac{\partial f\left(y_0, \epsilon = 0\right)}{\partial \epsilon} y_2\left(y_0, \epsilon\right) = \frac{\partial^2 f\left(y_0, \epsilon = 0\right)}{\partial \epsilon^2} \tag{A–3}$$

At the boundary of the new domain, the function y is replaced by Y to point out the difference. Its expansion in powers of ϵ can be written similarly as

$$Y = Y_0 + \epsilon Y_1\left(Y_0, \epsilon = 0\right) + \frac{1}{2}\epsilon^2 Y_2\left(Y_0, \epsilon = 0\right) + \cdots \tag{A–4}$$

Lastly, the variable $u\left(y, \epsilon\right)$ can be expanded in powers of ϵ along the mapping as

$$\mathrm{u}\left(\mathrm{y},\epsilon\right) = \mathrm{u}\left(\mathrm{y} = \mathrm{y}_0,\epsilon = 0\right) + \epsilon \frac{\mathrm{du}\left(\mathrm{y} = \mathrm{y}_0,\epsilon = 0\right)}{\mathrm{d}\epsilon} + \frac{1}{2}\epsilon^2 \frac{\mathrm{d}^2\mathrm{u}\left(\mathrm{y} = \mathrm{y}_0,\epsilon = 0\right)}{\mathrm{d}\epsilon^2} + \cdots \tag{A–5}$$

To obtain a formula for $\frac{\mathrm{du}\left(\mathrm{y} = y_0,\epsilon = 0\right)}{\mathrm{d}\epsilon}$, differentiate u along the mapping taking y to depend on ϵ, holding y_0 fixed. Using the chain rule, this gives

$$\frac{\mathrm{du}\left(\mathrm{y},\epsilon\right)}{\mathrm{d}\epsilon} = \frac{\partial \mathrm{u}\left(\mathrm{y},\epsilon\right)}{\partial \epsilon} + \frac{\partial \mathrm{u}\left(\mathrm{y},\epsilon\right)}{\partial \mathrm{y}} \frac{\partial y\left(\mathrm{y}_0,\epsilon\right)}{\partial \epsilon} \tag{A–6}$$

When the above equation is evaluated at $\epsilon = 0$, we obtain

$$\frac{\mathrm{du}\left(\mathrm{y} = \mathrm{y}_0,\epsilon = 0\right)}{\mathrm{d}\epsilon} = \mathrm{u}_1\left(\mathrm{y}_0\right) + \frac{\partial \mathrm{u}_0}{\partial y_0}\left(y_0\right) \mathrm{y}_1\left(\mathrm{y}_0, \epsilon\right) \tag{A–7}$$

where $u_1\left(y_0\right) = \frac{\partial u\left(y_0,\epsilon = 0\right)}{\partial \epsilon}$ and $\frac{\partial u_0}{\partial y_0}\left(y_0\right) = \frac{\partial u\left(y_0,\epsilon = 0\right)}{\partial y}$

All higher order derivatives of u can be determined the same way. If a domain variable needs to be specified at the boundary it is written similarly as

$$\frac{\mathrm{du}\left(\mathrm{y} = \mathrm{Y}_0,\epsilon = 0\right)}{\mathrm{d}\epsilon} = \mathrm{u}_1\left(\mathrm{Y}_0\right) + \frac{\partial \mathrm{u}_0\left(\mathrm{Y}_0\right)}{\partial \mathrm{y}_0} \mathrm{Y}_1\left(\mathrm{Y}_0, \epsilon\right) \tag{A–8}$$

When additional derivatives are obtained and substituted into the expansion of u, it becomes

$$\mathrm{u}\left(\mathrm{y},\epsilon\right) = \mathrm{u}_0 + \epsilon\left[\mathrm{u}_1 + \mathrm{y}_1 \frac{\partial \mathrm{u}_0}{\partial \mathrm{y}_0}\right] + \frac{1}{2}\epsilon^2\left[\mathrm{u}_2 + 2\mathrm{y}_1 \frac{\partial \mathrm{u}_1}{\partial \mathrm{y}_0} + \mathrm{y}_1^2 \frac{\partial^2 \mathrm{u}_0}{\partial \mathrm{y}_0^2} + \mathrm{y}_2 \frac{\partial \mathrm{u}_0}{\partial \mathrm{y}_0}\right] + \cdots \tag{A–9}$$

The above equation indicates that even for the domain equations mapping needs to be included in the governing equations. However, the mapping in the domain cannot be determined, in fact it is not needed neither. We will show this by means of an example and then use it as a rule of thumb. Let

$$\frac{\partial \mathrm{u}}{\partial \mathrm{y}} = 0 \tag{A–10}$$

defined in our inconvenient domain. Using chain rule

$$\frac{\partial \mathrm{u}}{\partial \mathrm{y}} = \frac{\partial \mathrm{u}}{\partial \mathrm{y}_0}\frac{\partial \mathrm{y}_0}{\partial \mathrm{y}} \tag{A–11}$$

where $\frac{\partial \mathrm{y}_0}{\partial \mathrm{y}}$ is determined using Equation A–2. Holding ϵ fixed

$$\frac{\partial \mathrm{y}_0}{\partial \mathrm{y}} = 1 - \epsilon\frac{\partial \mathrm{y}_1}{\partial \mathrm{y}} - \frac{1}{2}\epsilon^2\frac{\partial \mathrm{y}_2}{\partial \mathrm{y}} - \cdots \tag{A–12}$$

Thus, up to the first order in ϵ, the domain equation becomes

$$\frac{\partial \mathrm{u}}{\partial \mathrm{y}} = \frac{\partial \mathrm{u}_0}{\partial \mathrm{y}_0} + \epsilon\left[\frac{\partial \mathrm{u}_1}{\partial \mathrm{y}_0} + \mathrm{y}_1\frac{\partial^2 \mathrm{u}_0}{\partial \mathrm{y}_0^2}\right] + \cdots = 0 \tag{A–13}$$

The domain equation at the zeroth order in ϵ is

$$\frac{\partial \mathrm{u}_0}{\partial \mathrm{y}_0} = 0 \tag{A–14}$$

The domain equation at the first order in ϵ becomes

$$\frac{\partial \mathrm{u}_1}{\partial \mathrm{y}_0} + \mathrm{y}_1\frac{\partial^2 \mathrm{u}_0}{\partial \mathrm{y}_0^2} = 0 \tag{A–15}$$

However, $\dfrac{\partial^2 u_0}{\partial y_0^2}$ is zero. Therefore, Equation A–15 becomes

$$\frac{\partial \mathrm{u}_1}{\partial y_0} = 0 \tag{A–16}$$

The mapping does not appear in the domain equations. However, the mapping is saved for the surface variables as can be seen in all problems studied in this dissertation.

APPENDIX B
SURFACE VARIABLES

In this Appendix, we introduce the surface variables, namely the unit normal vector, the unit tangent vector, the surface speed and the mean curvature.

B.1 The Unit Normal Vector

We define a free surface by $z = Z(x,t)$ in Cartesian coordinates or $r = R(\theta, z)$ in cylindrical coordinates. Also, we define a functional that vanishes on the surface as

$$f = z - Z\left(x,t\right) = 0 \tag{B–1}$$

in Cartesian coordinates, and

$$f = r - R\left(\theta, z, t\right) \tag{B–2}$$

in cylindrical coordinates. The normal points into the region where f is positive is given by

$$\tilde{\mathrm{n}} = \frac{\nabla f}{|\nabla f|} \tag{B–3}$$

Here,

$$\nabla f = \frac{\partial f}{\partial x} i_x + \frac{\partial f}{\partial z} i_z$$

in Cartesian coordinates and

$$\nabla f = \frac{\partial f}{\partial r} i_r + \frac{1}{r}\frac{\partial f}{\partial \theta} i_\theta + \frac{\partial f}{\partial z} i_z$$

in cylindrical coordinates. Then, the equation for the normal is given by

$$\vec{n} = \frac{-\dfrac{\partial Z}{\partial x} i_x + i_z}{\left[\left[\dfrac{\partial Z}{\partial x}\right]^2 + 1\right]^{1/2}} \tag{B–4}$$

in Cartesian coordinates and

$$\vec{n} = \frac{i_r - \frac{1}{R}\frac{\partial R}{\partial \theta} i_\theta - \frac{\partial R}{\partial z} i_z}{\left[1 + \left[\frac{1}{R}\frac{\partial R}{\partial \theta}\right]^2 + \left[\frac{\partial R}{\partial z}\right]^2\right]^{1/2}} \tag{B–5}$$

in cylindrical coordinates.

B.2 The Unit Tangent Vector

The derivation of the unit tangent vector is straightforward using the definition $\tilde{\mathrm{n}} \cdot \tilde{\mathrm{t}} = 0$ from which we get

$$\tilde{\mathrm{t}} = \frac{i_x + \frac{\partial Z}{\partial x} i_z}{\left[\left[\frac{\partial Z}{\partial x}\right]^2 + 1\right]^{1/2}} \tag{B–6}$$

in Cartesian coordinates and

$$\vec{t} = \frac{\frac{\partial R}{\partial z} i_r + i_z}{\left[\left[\frac{\partial R}{\partial z}\right]^2 + 1\right]^{1/2}} \tag{B–7}$$

or

$$\vec{t} = \frac{\frac{1}{R}\frac{\partial R}{\partial \theta}\vec{i}_r + \left[1 + \left[\frac{\partial R}{\partial z}\right]^2\right]\vec{i}_\theta - \left[\frac{1}{R}\frac{\partial R}{\partial \theta}\frac{\partial R}{\partial z}\right]\vec{i}_z}{\left[\left[\frac{1}{R}\frac{\partial R}{\partial \theta}\right]^2 + \left[1 + \left[\frac{\partial R}{\partial z}\right]^2\right]^2 + \left[\frac{1}{R}\frac{\partial R}{\partial \theta}\frac{\partial R}{\partial z}\right]^2\right]^{1/2}} \tag{B–8}$$

in cylindrical coordinates.

B.3 The Surface Speed

Let a surface be denoted by

$$f(\vec{r}, t) = 0 \tag{B–9}$$

Let the surface move a small distance Δs along its normal in time Δt. Then, $f(\vec{r} \pm \Delta s\tilde{\mathrm{n}}, t + \Delta t)$ is given by

$$f(\vec{r} \pm \Delta s\tilde{\mathrm{n}}, t + \Delta t) = f(\vec{r}, t) \pm \Delta s\tilde{\mathrm{n}} \cdot \nabla f(\vec{r}, t) + \Delta t \frac{\partial f(\vec{r}, t)}{\partial \mathrm{t}} + \cdots \tag{B–10}$$

whence $f(\vec{r} \pm \Delta s\tilde{\mathrm{n}}, t + \Delta t) = 0 = f(\vec{r}, t)$ requires

$$\pm \Delta s\tilde{\mathrm{n}} \cdot \nabla f(\vec{r}, t) = -\Delta t \frac{\partial f(\vec{r}, t)}{\partial \mathrm{t}}$$

The normal speed of the surface, u, is then given by

$$\mathrm{u} = \pm \frac{\Delta s}{\Delta t} = -\frac{\dfrac{\partial f(\vec{r}, t)}{\partial t}}{\tilde{\mathrm{n}} \cdot \nabla f(\vec{r}, t)}$$

Now, using the definition of the unit normal given earlier we get

$$\mathrm{u} = -\frac{\dfrac{\partial f}{\partial t}}{|\nabla f|} \tag{B–11}$$

In our problems, the definition of u becomes

$$\mathrm{u} = \frac{\dfrac{\partial Z}{\partial t}}{\left[\left[\dfrac{\partial Z}{\partial x}\right]^2 + 1\right]^{1/2}} \tag{B–12}$$

in Cartesian coordinates and

$$u = \frac{\dfrac{\partial R}{\partial t}}{\left[1 + \left[\dfrac{1}{R}\dfrac{\partial R}{\partial \theta}\right]^2 + \left[\dfrac{\partial R}{\partial z}\right]^2\right]^{1/2}} \tag{B–13}$$

in cylindrical coordinates.

B.4 The Mean Curvature

The derivation of the curvature for a general surface is given in [10]. Here we provide the formulas for the surfaces studied in this dissertation. For the Cartesian

surface defined by Equation B–1, the mean curvature is given by

$$2H = \frac{Z_{xx}}{\left[Z_x^2 + 1\right]^{3/2}} \tag{B–14}$$

The subscript denotes the derivative of Z with respect to that variable. For the cylindrical surface defined by Equation B–2, the curvature is

$$2H = \frac{\left[1 + R_z^2\right]\left[-R^2 - 2R_\theta^2 + RR_{\theta\theta}\right] - 2R_\theta R_z\left[RR_{z\theta} - R_\theta R_z\right] + \left[R^2 + R_\theta^2\right]RR_{zz}}{\left[R^2\left[1 + R_z^2\right] + R_\theta^2\right]^{3/2}} \tag{B–15}$$

Again, the subscripts denote the derivatives.

APPENDIX C
THE VOLUME LOST AND GAINED FOR A LIQUID JET WITH A GIVEN PERIODIC PERTURBATION

Consider a volume of liquid with a given periodic perturbation as seen in Figure 5–1. Rotated about the axis of the jet, the volume lost is less than the volume gained. Although this statement seems counter-intuitive, yet it is not difficult to see the difference in the areas/volumes when two slices of same thickness of a cylinder are considered. As can be seen in Figure C-1, the outer area -similarly volume- is bigger than the inside area. The rotated volume in Figure 5–1 is similar in nature.

In this Appendix we want to prove mathematically that the gained volume is more than the lost volume. If we take Figure 5–1 as basis, we can represent the curve as follows

$$r = R + \epsilon \sin\left(\frac{2\pi}{\lambda} z\right) \tag{C–1}$$

Observe that r is equal to R when z is 0, $\lambda/2$ and λ. The volume gained and lost can be written as

$$V_g = \pi \int_0^{\lambda/2} \left[R^2 + \epsilon^2 \sin^2\left(\frac{2\pi}{\lambda} z\right) + 2R\epsilon \sin\left(\frac{2\pi}{\lambda} z\right) \right] dz$$

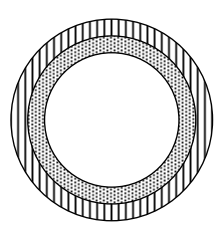

Figure C-1: The volume argument for a volume of liquid with a given perturbation.

$$V_l = \pi \int_{\lambda/2}^{\lambda} \left[R^2 + \epsilon^2 \sin^2\left(\frac{2\pi}{\lambda} z\right) + 2R\epsilon \sin\left(\frac{2\pi}{\lambda} z\right) \right] dz \tag{C–2}$$

When the integrals are evaluated, the first two terms are equal to each other for the volumes gained and lost. They are $\frac{1}{2}\pi R^2 \lambda$ and $\frac{1}{4}\pi \epsilon^2 \lambda$. On the other hand the last term for the gained volume is $2\epsilon R\lambda$ and $-2\epsilon R\lambda$ for the lost volume. Hence, the volume gained is more than the volume lost under the curve rotated about the axis of the jet.

APPENDIX D
THE EFFECT OF INERTIA IN THE RAYLEIGH-TAYLOR AND LIQUID JET PROBLEMS

The aim of this calculation is to show the effect of flow for an inviscid liquid in the Rayleigh-Taylor and liquid jet problems. The problem is sketched in Figure D-1. The free surface is located at $z = 1$. The liquid of density ρ lies above a passive gas.

The governing nonlinear equations are

$$\rho\left[v_x\frac{\partial v_x}{\partial x} + v_z\frac{\partial v_x}{\partial z}\right] = -\frac{\partial P}{\partial x}$$
$$\rho\left[v_x\frac{\partial v_z}{\partial x} + v_z\frac{\partial v_z}{\partial z}\right] = -\frac{\partial P}{\partial z} + \rho g \tag{D–1}$$

and

$$\frac{\partial v_x}{\partial x} + \frac{\partial v_z}{\partial z} = 0 \tag{D–2}$$

The stability of the problem is determined via a perturbation analysis described in Chapter 3. The base state velocity profile is chosen to be $v_{x,0} = f(z)$ which satisfies the continuity equation. The base state is given by

$$v_{x,0} = f(z), \quad v_{z,0} = 0, \quad \text{and} \quad P_0 = \rho g z \tag{D–3}$$

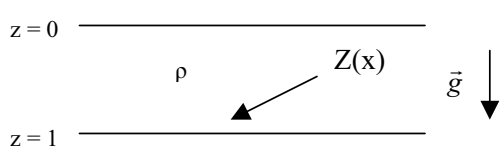

Figure D-1: Sketch of the problem depicting a liquid on top of air.

The perturbed equations are given as follows

$$\rho\left[v_{x,0}\frac{\partial v_{x,1}}{\partial x}+v_{z,1}\frac{\partial v_{x,0}}{\partial z}\right]=-\frac{\partial P_1}{\partial x}$$

$$\rho\left[v_{x,0}\frac{\partial v_{z,1}}{\partial x}\right]=-\frac{\partial P_1}{\partial z} \tag{D–4}$$

and

$$\frac{\partial v_{x,1}}{\partial x}+\frac{\partial v_{z,1}}{\partial z}=0 \tag{D–5}$$

Taking the curl of the equation of motion, one obtains

$$v_{x,0}\frac{\partial^2 v_{x,1}}{\partial x\partial z}+v_{z,1}\frac{\partial^2 v_{x,0}}{\partial z^2}-v_{x,0}\frac{\partial^2 v_{z,1}}{\partial z^2}=0 \tag{D–6}$$

Letting $v_{x,0}=Cz$ where C is a constant, eliminating $v_{x,1}$ using the continuity and finally expanding $v_{z,1}=\hat{v}_{z,1}e^{ikx}$, dropping the hat, one gets

$$\frac{d^2 v_{z,1}}{\partial z^2}-k^2 v_{z,1}=0 \tag{D–7}$$

The solution to the above equation is

$$v_{z,1}=A\cosh(kz)+B\sinh(kz) \tag{D–8}$$

At $z=0$, the no-flow condition, $v_{z,1}=0$, results in $A=0$. At the interface, $z=1$, the no-mass transfer condition is given by

$$v_{z,1}-ikZ_1v_{x,0}=0 \tag{D–9}$$

The constant B is found by substituting the expression for $v_{z,1}$ and $v_{x,0}$ as

$$B=\frac{ikC}{\sinh(k)}Z_1$$

The last equation is the normal stress balance given by

$$P_1+Z_1\frac{dP_0}{dz}=\gamma k^2 Z_1 \tag{D–10}$$

The pressure term in the normal stress balance is eliminated by first taking the derivative of it with respect to x, and using the equations of motion. After these substitutions, Equation D–10 becomes

$$\left[\rho C^2 \left[1 - k \coth\left(k\right)\right] - \rho g + \gamma k^2\right] Z_1 = 0 \tag{D–11}$$

is obtained. Observe that $k \coth\left(k\right)$ is larger than unity. As can be seen from Equation D–11, the effect of the gravity is increased, which implies that the critical wavelength is decreased. Therefore, the flow makes Rayleigh-Taylor problem less stable.

The second problem of interest is flow in a jet where inertia is dominant. The governing nonlinear equations are very similar but written in cylindrical coordinates. The governing equation, counterpart of Equation D–7 is

$$r^2 \frac{d^2 v_{r,1}}{\partial r^2} + r \frac{d v_{r,1}}{\partial r} - k^2 r^2 v_{r,1} = 0 \tag{D–12}$$

After solving for the differential equation, and applying boundary conditions, the expression for the velocity is substituted into the normal stress balance. The resulting equation is

$$\left[\frac{-\gamma}{R_0^2} + \gamma k^2 - \rho C^2 R_0^2 \frac{I_1\left(kR_0\right)}{I_0\left(kR_0\right)} k\right] R_1 = 0 \tag{D–13}$$

The term coming with the flow is always destabilizing. Therefore, the flow makes liquid jet less stable.

REFERENCES

[1] D. Langbein, "Crystal growth from liquid columns," *Journal of Crystal Growth*, vol. 104, pp. 47–59, 1990.

[2] R. A. Brown, "Theory of transport processes in single crystal growth from the melt," *AIChE Journal*, vol. 34, pp. 881–911, 1988.

[3] C. Hickox, "Instability due to viscosity and density stratification in axisymmetric pipe flow," *Physics of Fluids*, vol. 14, pp. 251–262, 1971.

[4] J. B. Grotberg, "Preface: Biofluid mechanics," *Physics of Fluids*, vol. 17, Art. No. 031401, 2005.

[5] A. M. Jacob and D. P. Gaver, "An investigation of the influence of cell topography on epithelial mechanical stresses during pulmonary airway reopening," *Physics of Fluids*, vol. 17, Art. No. 031502, 2005.

[6] J. P. White and M. Heil, "Three-dimensional instabilities of liquid-lined elastic tubes: A thin-film fluid-structure interaction model," *Physics of Fluids*, vol. 17, Art. No. 031506, 2005.

[7] L. Smarr, J. R. Wilson, R. T. Barton, and R. L. Bowers, "Rayleigh-Taylor overturn in super-nova core collapse," *Astrophysics Journal*, vol. 246, pp. 515–525, 1981.

[8] N. K. Gupta and S. . V. Lawande, "Effects of density gradients on Rayleigh-Taylor instability in an ablatively accelerated inertial confinement fusion target," *Plasma Physics and Controlled Fusion*, vol. 28, pp. 267–278, 1986.

[9] F. D. Rumscheidt and S. G. Mason, "Break-up of stationary liquid threads," *Journal of Colloid Science*, vol. 17, pp. 260–269, 1962.

[10] L. E. Johns and R. Narayanan, *Interfacial Instability*, Springer-Verlag, New York, 2002.

[11] F. Savart, "Memoire sur la constitution des veines liquides lancées par des orifices circulaires en mince paroi," *Annales de chimie et de physique*, vol. 53, pp. 337–386, 1833.

[12] J. Plateau, *Experimental and Theoretical Researches on the Figures of Equilibrium of a Liquid Msass*, Annual Reports of the Smithsonian Institution (translated), 1863.

[13] J. W. S. Rayleigh, "On the instability of jets," *Proceedings of the London Mathematical Society*, vol. 10, pp. 4–13, 1878.

[14] J. W. S. Rayleigh, "On the capillary phenomena of jets," *Proceedings of the Royal Society*, vol. 19, pp. 71–97, 1879.

[15] J. W. S. Rayleigh, *Theory of Sound*, Macmillan, London, 1896. (Reprinted by Dover, New York, 1945.)

[16] J. W. S. Rayleigh, "On the instability of a cylinder of viscous liquid under capillary force," *Philosophical Magazine*, vol. 34, pp. 145, 1892.

[17] S. Chandrasekhar, *Hydrodynamic and Hydromagnetic Stability*, Oxford University Press, London, 1961.

[18] R. J. Donnelly and W. Glaberson, "Experiments on capillary instability of a liquid jet," *Proceedings of the Royal Society of London Series A - Mathematical and Physical Sciences*, vol. 290, pp. 547–556, 1966.

[19] P. Lafrance, "Nonlinear breakup of a laminar liquid jet," *The Physics of Fluids*, vol. 18, pp. 428–432, 1975.

[20] N. N. Mansour and T. S. Lundgren, "Satellite formation in capillary jet breakup," *Physics of Fluids A*, vol. 2, pp. 1141–1144, 1990.

[21] S. Tomotika, "On the instability of a cylindrical thread of a viscous liquid surrounded by another viscous liquid," *Proceedings of The Royal Society of London, Series A*, vol. 150, pp. 322–337, 1935.

[22] B. J. Meister and G. F. Scheele, "Generalized solution of the Tomotika stability analysis for a cylindrical jet," *AIChE Journal*, vol. 13, pp. 682–688, 1967.

[23] S. P. Lin, *Breakup of Liquid Sheets and Jets*, Cambridge University, United Kingdom, 2003.

[24] J. Eggers, "Dynamics of liquid nanojets," *Physical Review Letters*, vol. 89, pp. 1–4, 2002.

[25] B. J. Lowry, Shape Stability of Liquid Bridges in Flow, Ph.D. Dissertation, Cornell University, Ithaca, NY, 1994.

[26] D. Langbein, *Capillary Surfaces: Shape-Stability-Dynamics, in Particular Under Weightlessness*, Springer-Verlag, Berlin Heidelberg, 2002.

[27] L. M. Witkowski and J. S. Walker, "Flow driven by Marangoni convection and rotating magnetic field in a floating-zone configuration," *Magnetohydrodynamics*, vol. 37, pp. 112–118, 2001.

[28] A. Cröll, T. Kaiser, M. Schweiser, A. N. Danilewski, S. Lauer, A. Tegetmeier, and K. W. Benz, "Floating-zone and floating-solution-zone growth of GaSb under microgravity," *Journal of Crystal Growth*, vol. 191, pp. 365–376, 1998.

[29] G. Müller and F. M. Herrmann, "Growth of 20 mm diameter GaAs crystals by the floating zone technique during the D-2 Spacelab mission," in *Materials and Fluids Under Low Gravity*, Eds: L. Ratke, H. Walter, and B. Feuerbacher, Springer-Verlag, Berlin Heidelberg, 1996.

[30] J. W. S. Rayleigh, "Investigation of the character of equilibrium of an incompressible heavy fluid of variable density," *Proceedings of the London Mathematical Society*, vol. 14, pp. 170–177, 1883.

[31] G. I. Taylor, "Effect of variation in density on the stability of superposed streams of fluid," *Proceedings of The Royal Society of London Series A*, vol. 132, pp. 499–523, 1931.

[32] C. Völtz, W. Pesch, and I. Rehberg, "Rayleigh-Taylor instability in a sedimenting suspension," *Physical Review E*, vol. 65, pp. 0114041–0114047, 2001.

[33] J. Yang, A. D'Onofrio, S. Kalliadasis, and A. D. Wit, "Rayleigh-Taylor instability of reaction-diffusion acidity fronts," *Journal of Chemical Physics*, vol. 117, pp. 9395–9408, 2002.

[34] Y. N. Young, H. Tufo, A. Dubey, and R. Rosner, "Rayleigh-Taylor instability of reaction-diffusion acidity fronts," *Journal of Fluid Mechanics*, vol. 447, pp. 377–408, 2001.

[35] P. d. Gennes, F. Brochard-Wyart, and D. Quéré, *Capillarity and wetting phenomena ; drops, bubbles, pearls, waves*, Springer-Verlag, New York, 2004.

[36] Y. J. Chen and P. H. Steen, "Suppression of the capillary instability in the Rayleigh-Taylor slot problem," *Physics of Fluids*, vol. 8, pp. 97–102, 1996.

[37] D. Y. Hsieh, "Effects of heat and mass transfer on Rayleigh-Taylor instability," *Transactions of the ASME*, vol. 94, pp. 156–162, 1972.

[38] S. P. Ho, "Linear Rayleigh-Taylor stability of viscous fluids with mass and heat transfer," *Journal of Fluid Mechanics*, vol. 101, pp. 111–128, 1980.

[39] O. Ozen and R. Narayanan, "The physics of evaporative and convective instabilities in bilayer systems: linear theory," *Physics of Fluids*, vol. 16, pp. 4644–4652, 2004.

[40] H. A. Dijkstra and P. Steen, "Thermocapillary stabilization of the capillary breakup of an annular film of liquid," *Journal of Fluid Mechanics*, vol. 229, pp. 205–228, 1991.

[41] J. L. Duda and J. S. Vrentas, "Steady flow in the region of closed streamlines in a cylindrical cavity," *Journal of Fluid Mechanics*, vol. 45, pp. 247–260, 1971.

[42] L. E. Scriven and C. V. Sternling, "On cellular convection driven by surface-tension gradients: effects of mean surface tension and surface viscosity," *Journal of Fluid Mechanics*, vol. 45, pp. 247–260, 1964.

[43] S. Agarwal, L. E. Johns, and R. Narayanan, "Growth curves in precipitation and solidification," *Journal of Crystal Growth* (submitted), 2006.

[44] P. Grindrod, *The Theory and Applications of Reaction-Diffusion Equations Patterns and Waves*, Oxford University Press, Oxford, 1996.

[45] H. F. Weinberger, *A First Course in Partial Differential Equations with Complex Variables and Transform Methods*, Wiley, New York, 1965.

[46] G. Mason, "An experimental determination of the stable length of cylindrical liquid bubbles," *Journal of Colloid and Interface Science*, vol. 32, pp. 172–176, 1970.

[47] J. Meseguer, J. M. Perales, and J. I. D. Alexander, "A perturbation analysis of the stability of long liquid bridges between almost circular supporting disks," *Physics of Fluids*, vol. 13, pp. 2724–2727, 2001.

[48] A. Lavern-Simavilla, J. Meseguer, and J. L. Espino, "Stability of liquid bridges between an elliptical and a circular supporting disk," *Physics of Fluids*, vol. 15, pp. 2830–2836, 2003.

[49] C. T. Gallagher, D. T. Leighton, and M. J. McCready, "Experimental investigation of a two-layer shearing instability in a cylindrical couette cell," *Physics of Fluids*, vol. 8, pp. 2385–2390, 1996.

[50] S. R. Coriell, S. C. Hardy, and M. R. Cordes, "Stability of liquid zones," *Journal of Colloid and Interface Science*, vol. 60, pp. 126–136, 1977.

[51] L. A. Slobozhanin and J. M. Perales, "Stability of liquid bridges between equal disks in an axial gravity field," *Physics of Fluids A*, vol. 5, pp. 1305–1314, 1993.

[52] B. J. Matkowsky and E. Reiss, "Singular perturbations of bifurcations," *SIAM Journal of Applied Mathematics*, vol. 33, pp. 230–255, 1977.

[53] B. J. Lowry and P. H. Steen, "Stabilization of an axisymmetric liquid bridge by viscous flow," *International Journal of Multiphase Flow*, vol. 20, pp. 439–443, 1994.

[54] B. J. Lowry and P. H. Steen, "Flow influenced stabilization of liquid columns," *Journal of Colloid and Interface Science*, vol. 170, pp. 38–43, 1994.

[55] B. J. Lowry and P. H. Steen, "Stability of slender liquid bridges subjected to axial flows," *Journal of Fluid Mechanics*, vol. 330, pp. 189–213, 1997.

[56] Y. J. Chen, N. D. Robinson, J. M. Herndon, and P. H. Steen, "Liquid bridge stabilization: theory guides a codimension-two experiment," *Computational Methods in Applied Mechanics and Engineering*, vol. 170, pp. 209–221, 1999.

[57] S. Atreya and P. H. Steen, "Stability analysis of long liquid bridges in the presence of gravity and flow," *Proceedings of the Royal Society of London Series A Mathematical and Physical Sciences*, vol. 458, pp. 2645–2669, 2002.

[58] D. T. Johnson, "Viscous effects in liquid encapsulated liquid bridges," *International Journal of Heat and Fluid Flow*, vol. 23, pp. 844–854, 2002.

[59] K. A. Brakke, "The surface evolver," *Experimental Mathematics*, vol. 1, pp. 141–165, 1992.

[60] K. A. Brakke, "The surface evolver and the stability of liquid surfaces," *Philosophical Transactions of the Royal Society of London*, vol. 354, pp. 2143–2157, 1996.

[61] A. K. Uguz, N. J. Alvarez, and R. Narayanan, "An experimental study on the instability of elliptical liquid bridges," *Physics of Fluids*, vol. 17, pp. 0781061–0781064, 2005.

BIOGRAPHICAL SKETCH

Kerem Uğuz was born in Turkey. He graduated from Boğazici University in Istanbul, Turkey, receiving a B.S degree in 1999 and a M.S degree in 2001 in chemical engineering. His master's thesis title is "Selective Low Temperature CO Oxidation in H_2-rich Gas Streams". He then attended the University of Florida for graduate studies under the supervision of Prof. Ranga Narayanan. In 2006, he graduated from the University of Florida with a Ph.D in chemical engineering.